SEARCH FOR COSMIC-RAY ANTIDEUTERONS WITH THE AMS-02 EXPERIMENT ON THE INTERNATIONAL SPACE STATION

A DISSERTATION SUBMITTED TO THE GRADUATE DIVISION OF THE UNIVERSITY OF HAWAI'I AT MĀNOA IN PARTIAL FULFILLMENT OF THE REQUIREMENTS FOR THE DEGREE OF

DOCTOR OF PHILOSOPHY

IN

PHYSICS

MAY 2019

By

Travis Gordon Nelson

Dissertation Committee:

Philip von Doetinchem, Chairperson
Veronica Bindi
Jason Kumar
Sven Vahsen
Nodari Sitchinava

"It won't take that long to graduate!"

-Me, circa 2011

Abstract

The AMS-02 experiment has been measuring the comic-ray spectrum since its installation on the International Space Station in May 2011. This dissertation presents the results of a low-energy antiparticle analysis. The first part of this dissertation investigates the low-energy Galactic antiproton flux. Details of the analysis variables are explained. Further described are the techniques used to determine the true energy spectrum of the measured antiprotons. The analysis result is presented. Compared to the previously published results from AMS-02, the low-energy antiproton flux has been extended down to 0.85 GeV/c. The second part of this dissertation focused on the low-energy Galactic antideuteron analysis. A method was developed to suppress the antiproton background using energy depositions. The anaysis variables were also improved from the antiproton analysis. A Galactic antideuteron exclusion limit was set at 1.23×10^{-5} [(GeV/n) m^2 sr s]$^{-1}$. Predictions were then made on the AMS-02 antideuteron discovery sensitivity through 2024 and 2030.

Acknowledgements

I would like to thank my advisor, Philip, for allowing me to pursue the antideuteron study for my dissertation. If you had not taken the chance in bringing me on I would not be where I am today.

I would like to thank the AMS-02 collaboration as a whole for designing, building, and operating such a great experiment. I would like to give a special thanks to Nikolas Zimmermann and Bastian Beischer for helping me to use ACsoft to extract the AMS-02 data. I would like to thank Weiwei Xu for guidance with respect to the antiproton flux analysis.

Many thanks to the cosmic ray antiparicle group at here in Hawai‘i for the in-depth analysis discussions. Good luck on the continuing effort!

Most importantly I would like to thank my wife Rosalie for the years of support while I completed this dissertation. Your patience, understanding, and love got me through this crazy wild time.

Thanks everyone!

This work was partially funded by the National Science Foundation.

Primary data extraction for this analysis used ACsoft developed at RWTH Aachen University. All the analysis in this dissertation used the ROOT framework developed at CERN.

Contents

List of Figures

List of Tables

Abbreviations

ACC	Anti Coincidence Counter
AMS-02	Alpha Magnetic Spectrometer
BESS	Balloon-borne Experiment with Superconducting Spectrometer
CDM	Cold Dark Matter
DM	Dark Matter
DOF	Degrees of Freedom
ECAL	Electromagnetic Calorimeter
FOV	Field of view
HDM	Hot Dark Matter
ISS	International Space Station
LTOF	Lower TOF
MC	Monte Carlo
NDF	Number of Degrees of Freedom
PAMELA	Payload for Antimatter Matter Exploration and Light-nuclei Astrophysics
PMT	Photomultiplier tube
RICH	Ring Imaging Cherenkov Counter
SAA	South Atlantic Anomaly
TOF	Time of Flight
TRD	Transition Radiation Detector
UTOF	Upper TOF
WIMP	Weakly Interacting Massive Particle

For my Grandmother, Gloria J. Nelson (1922-2017) and my Dad, Karl G. Nelson (1955-2016). I miss you both...

Chapter 1

Introduction

In the year 2019 the composition of the vast majority of gravitating matter in the Universe is unknown. 86 years have passed since it was postulated in the literature that there existed this non-luminous matter. What is Dark Matter?

To date antinuclei have not been observed in cosmic rays. The lightest antinuclei, antideuterons, are hypothesized to be reaction products of potential Dark Matter theories. Antideuterons may also be produced by primary cosmic rays interacting with the interstellar medium. These two potential sources have different production peaks and are thus distinguishable.

The Alpha Magnetic Spectrometer (AMS-02) experiment aims to make the first detection of antinuclei in cosmic rays. Mounted on the International Space Station, AMS-02 is a large mass spectrometer capable of measuring the cosmic ray spectrum with great precision from momenta of 500 MeV/c per nucleon to above 1 TeV/c per nucleon.

Chapter two provides a brief overview of particle astrophysics. It begins with a short history of astrophysics and particle physics from the discovery of cosmic rays to present. Following this synopsis, the current motivations for Dark Matter are described. Finally, the AMS-02 detector and descriptions of its sub-detectors are presented in detail.

Chapter three details the low-energy antiproton flux analysis carried out using the AMS-02 Time-of-Flight system. The procedure is described in detail. This was done in preparation for the study of antideuterons with the AMS-02 experiment.

Chapter four details the low-energy antideuteron analysis on AMS-02 data from 2011 through 2017. A means of suppressing the antiproton background is described. Also described in detail is the final estimation of the remaining antiproton background. An antideuteron exclusion limit is set based on the data analyzed. A prediction is then made on the AMS-02 antideuteron

discovery sensitivity through 2024 and 2030 which correspond to potential International Space Station retirement dates.

Chapter five summarizes the results from work carried out in this dissertation. Implications of the results and a future outlook are also presented.

Chapter 2

Astroparticle Physics and the AMS-02 Experiment

2.1 Cosmic Rays

A man by the name of Victor Hess packed his electroscope into his balloon's gondola on 17 April 1912. There was a near total solar eclipse viewed from the launch region in lower Austria. Hess made a flight to 2750 meters. His electroscope registered an increased ionization rate compared to sea level, and no change in observed rate during the eclipse. Thus, concluded Hess, the source of ionizing radiation which his electroscope measured was not from the Earth nor the Sun, it must originate deeper in space [1].

Over a century later the origin of the highest energy cosmic rays is still a mystery. Much has been learned about their properties. We now know that cosmic rays are composed of high energy particles, mostly protons, electrons, and heavier atomic nuclei. The energy spectrum of cosmic rays have been measured to nearly 10^{21} eV. The all particle energy spectrum for cosmic rays is presented in Fig. 2.1.

The fluxes of individual particle species have been measured with great precision up to $\mathcal{O}$(TeV) by various experiments at balloon altitudes as well as in Low Earth Orbit [3–6]. Although the source of the highest energy cosmic rays is unknown, some high energy sources have been identified [7]. For instance, during coronal mass ejections, solar energetic particles have been measured at energies above 5 GeV. Trapped radiation belts have been identified with particle energies also on the order of a GeV. There is strong evidence that some super nova remnants are emitting particle radiation at energies above a GeV [8].

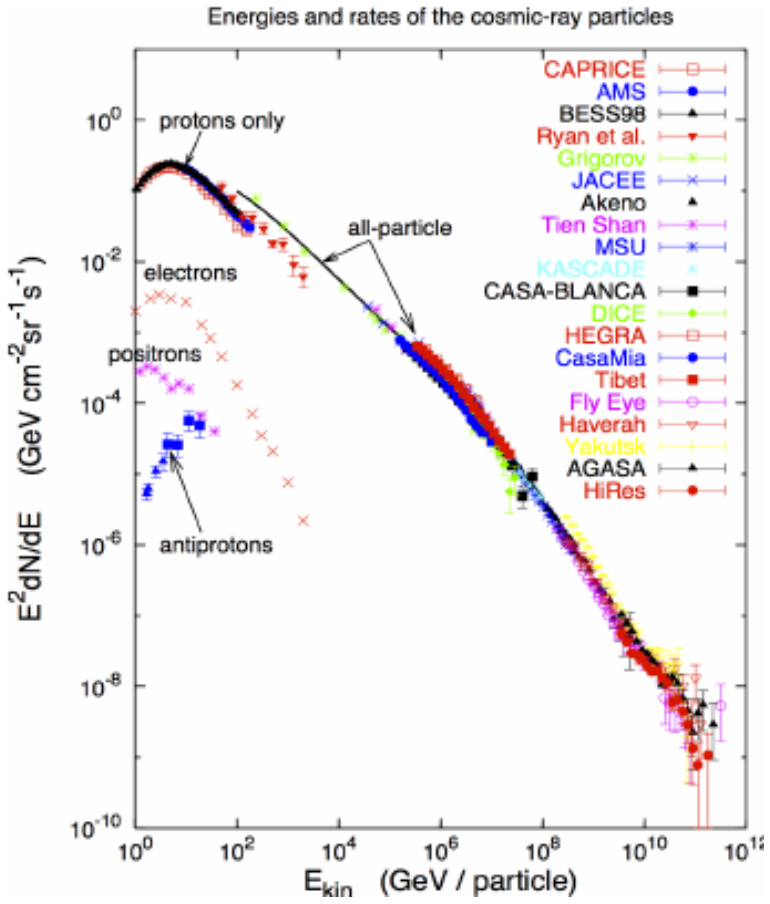

FIGURE 2.1: The all particle cosmic ray spectrum as well as a few constituent fluxes. [2]

2.2 Antimatter

The observable universe is matter dominated. In 1928 Paul Dirac combined the quantum theory of the electron and special relativity in the so called Dirac Equation [9]. This unification led to an unexpected prediction. A negative energy solution existed, which could be satisfied by an electron of positive charge. This so called anti-electron would be discovered by Carl Anderson in 1932 while studying cosmic ray tracks in a cloud chamber [10]. This constituted the first observational evidence of an antiparticle. Anderson called it the positron. In time the antiproton and antineutron would be discovered and in 1965 the first antinucleus, the antideuteron, was observed at Brookhaven National Laboratory [11].

The largest abundance of antimatter exists as space radiation, primarily of secondary origin. As high energy cosmic rays impinge upon the interstellar medium interactions occur which may produce stable antiparticles. Let us consider the secondary production of antiprotons. The majority of cosmic rays are protons. Likewise, the majority of the interstellar medium is hydrogen. Therefore, the most probable interaction to occur is that a cosmic ray proton will

strike a proton at rest. The rest mass of a proton is 938 MeV/c^2, as is the rest mass of an antiproton. The threshold reaction to produce a single antiproton will be:

$$pp \longrightarrow pp\bar{p}p. \tag{2.1}$$

It is useful to consider the Lorentz invariant center-of-momentum energy, $\sqrt{s}$, to calculate the threshold energy for the reaction to occur. Since the final state will be 4 particles of equal mass, M_p, $\sqrt{s_{threshold}} = 4M_p$. The incoming cosmic ray proton must have incoming kinetic energy, E_p, determined by $s = 16M_p = 2M_p + 2M_pE_p$. Thus, the threshold production energy of antiprotons by cosmic rays impinging on the interstellar medium is $7M_p$ or 6.6 GeV.

$$\sqrt{s} = \sqrt{2M_p + 2EM_p} \tag{2.2}$$

From Fig. 2.1 one can see that the particle flux begins to fall steeply before this threshold energy. In addition, the antiproton production cross section is very small. It is therefore deduced that the antiproton production rate will be quite small. In fact, the observed antiproton to proton flux ratio is on the 10^{-5} level for energies on the order of 1 GeV [12].

The method of antinucleus production is not well understood. The simplest antinucleus is the antideuteron, an antiproton bound with an antineutron. It is theorized that if an antiproton and antineutron are formed close enough in phase space they will merge to form an antideuteron. This production mechanism has been dubbed coalescence [13–16]. Eq.2.3 gives the simplified representation for antideuteron coalescence. The full momentum derivatives represent the particle spectra and p_0 is the coalescence momentum.

$$\gamma_{\bar{d}}\frac{\mathrm{d}^3N_{\bar{d}}}{\mathrm{d}p^3_{\bar{d}}} = \frac{\pi}{6}p_0^3\left(\gamma_{\bar{p}}\frac{\mathrm{d}^3N_{\bar{p}}}{\mathrm{d}p^3_{\bar{p}}}\right)\left(\gamma_{\bar{n}}\frac{\mathrm{d}^3N_{\bar{n}}}{\mathrm{d}p^3_{\bar{n}}}\right) \tag{2.3}$$

The antineutrons are produced by the same process as antiprotons, cosmic rays interacting with the interstellar medium. The coalescence mechanism requires the antiproton and antineutron to be close in phase space thus antideuterons produced from this mechanism will be highly boosted. Secondary production of antideuterons from cosmic ray interactions with the interstellar medium peaks at about 4 GeV/n [17]. The favored production reaction is:

$$pp \longrightarrow pp\bar{p}p\bar{n}n \longrightarrow pp\bar{n}\bar{d}. \tag{2.4}$$

The expected flux level of secondary antideuterons is greatly influenced by the value of the coalescence momentum. In general a higher value of the coalescence momentum will result in a secondary antideuteron flux of greater intensity. A study done by Korsmeier, Donato, and Fornengo [17] predicts the peak secondary antideuteron flux to be between 10^{-7} and 10^{-6} $[(\mathrm{GeV}/n)\ \mathrm{m}^2\ \mathrm{sr}\ \mathrm{s}]^{-1}$ for a typical value or a very large value of the coalescence momentum respectively (see Figs. 2.7 and 2.8).

These antiparticles may continue their journey through space or later annihilate with the interstellar medium. Because the relative abundance of antimatter to matter is very small, minute features in the cosmic ray spectrum may be probed.

2.3 The Standard Model

The standard model is the current theoretical framework of particle physics. The standard model is based on gauge symmetries with matter fields for quarks and leptons, fields for gauge bosons, and a scalar field boson. All particles of the standard model have been observed experimentally. The last particle to be identified was the scalar Higgs boson, whose discovery was announced on 4 July 2012 by the CERN LHC collaboration [18, 19].

The symmetries of the elementary particles are described by unitary groups (Eq. 2.5).

$$SU(3)_C \otimes SU(2)_L \otimes U(1)_Y \tag{2.5}$$

$\mathrm{SU}(3)_C$ is the group for the strong force which is carried by the color charge of quarks. $\mathrm{SU}(2)_L$ $\otimes$ $\mathrm{U}(1)_Y$ is the group of the electroweak interaction which is the unification of electromagnetism and weak force interaction. Gravitation has not yet been unified with the standard model.

2.4 Experimental Motivation for Dark Matter

The universe cannot be described using the physical principles currently understood to be true and purely luminous baryonic matter. In fact, observations suggest that the mass energy of the universe is composed of less than 5% luminous matter. The rest is postulated to be a combination of dark matter (27%) and dark energy (68%). Dark energy can be thought of as the engine driving inflation. The term dark matter was coined by Fritz Zwicky in the 1930's [20]. Zwicky realized that the motion of galaxies in the Coma cluster could not be explained by the luminous matter of the cluster alone. He applied the virial theorem to the cluster and concluded that much more mass was needed to explain the velocity dispersion, i.e. "Dark Matter."

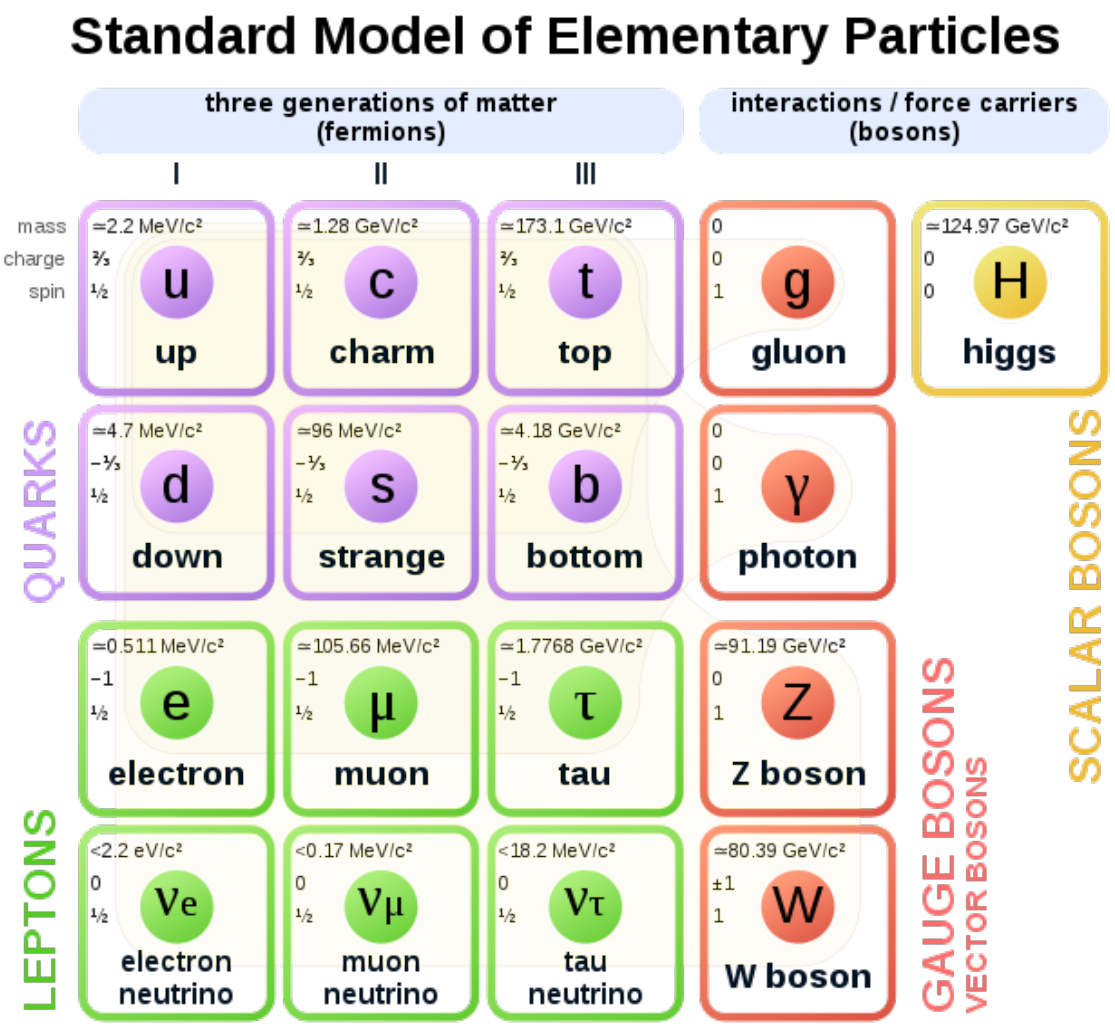

FIGURE 2.2: The standard model. Credit:Wikipedia User MissMJ

Galactic rotation curves provide some of the most compelling evidence for dark matter. The rotation curve of our nearest galactic neighbor, Andromeda, was first measured by Babcock et. al. in 1938 [21]. As rotational velocities were measured further out on the disk from the center, an unexpected trend was observed. With respect to increasing radial position, rotation velocities increase linearly and then plateau. This systematic trend was clearly diagnosed by Freeman in 1970 [22]. The increasing and then constant rotation velocity with respect to increasing distance from the galactic center is unexpected because the surface luminosity of a galactic disk falls off exponentially with radius as given by:

$$I(r) = I_0 e^{-\frac{r}{r_D}} \tag{2.6}$$

FIGURE 2.3: Hubble Space Telescope color image of the spiral galaxy NGC 6503. Rotation velocity measurements have been made to 12.8 disk scale lengths by measuring radio emissions from the 21 cm neutral hydrogen line. Credit:NASA, ESA, D. Calzetti (University of Massachusetts), H. Ford (Johns Hopkins University), and the Hubble Heritage (STScI/AURA)-ESA/Hubble Collaboration

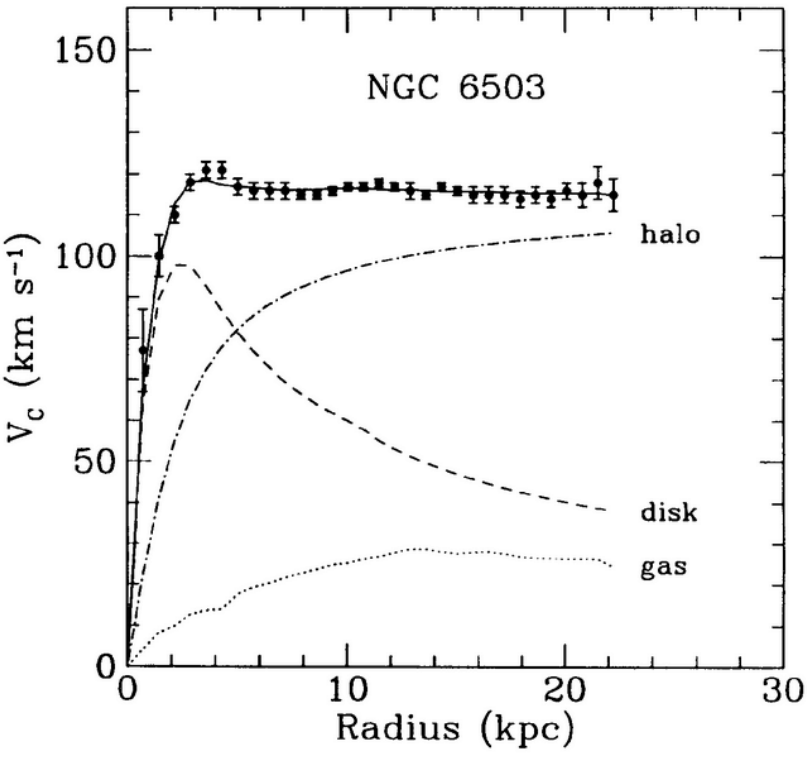

FIGURE 2.4: Galactic rotation curve measured for NGC 6503. [23]

where r_D is the "disk scale length." Since luminous mass is proportional to luminosity one would expect that most of the galactic mass would be concentrated within a few scale lengths. This scenario would produce Keplerian rotational velocities, proportional to $r^{-1/2}$, which is in conflict with measurement. Many systematic studies of galactic rotation curves have been performed in the optical band and support the non-Keplerian view.

The most convincing evidence for this flattened nature comes from radio observations [24]. Observations of the neutral hydrogen 21 cm line can be made at large radii. A case in point is the galaxy NGC6503, Fig. 2.3, where $r_D = 1.73$ kpc and the last 21 cm measurement is at $12.8r_D$. As a comparison, optical measurements typically extend to $r_D = 1.5$ to 3.5.

The flat rotation curve is confirmed in radio even at these large distances from the galactic center as shown in Fig. 2.4. The difference between the expected rotation curve from the luminous mass distribution compared to what is observed is attributed to dark matter. The observed rotation curves indicate that there exists a halo of dark matter in which galaxies lie. Although the exact profile of the dark matter halo is unknown, a good fit to observations was proposed by Navarro, Frenk, and White [25]. Eq. 2.7 gives the proposed NFW dark matter halo density profile.

$$\rho(r) = \frac{\rho_h}{(r/r_h)(1 + r/r_h)^2} \tag{2.7}$$

Observations have been made of galactic clusters which have passed through one another. What has been observed of these interactions provides compelling evidence for dark matter. For example see the well known "Bullet Cluster" (Fig. 2.5). This composite image presents X-ray emission in red and gravitating matter inferred from lensing in blue, overlaid on the optical field. The majority of the matter appears to have been unaffected by the passage, yet it can be seen that intergalactic gas has been excited at the collision region. Furthermore this ionized material is no longer comoving with the majority of matter in the clusters. This is a telltale indicator that the majority of the matter has a very small interaction cross section which is consistent with dark matter. This phenomenon is not restricted to the Bullet Cluster alone, but has been observed in a number of other clusters. For example see Fig. 2.6 of the cluster MACS J0025.4-1222, which was studied in 2008.

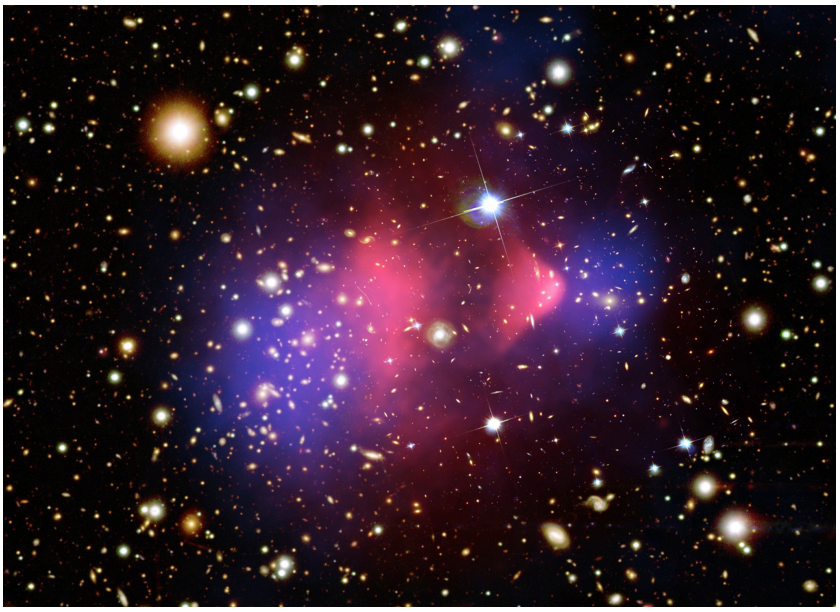

FIGURE 2.5: The Matter of the Bullet Cluster Composite Credit: X-ray: NASA/CXC/CfA/ M.Markevitch et al.; Lensing Map: NASA/STScI; ESO WFI; Magellan/U.Arizona/ D.Clowe et al. Optical: NASA/STScI; Magellan/U.Arizona/D.Clowe et al.

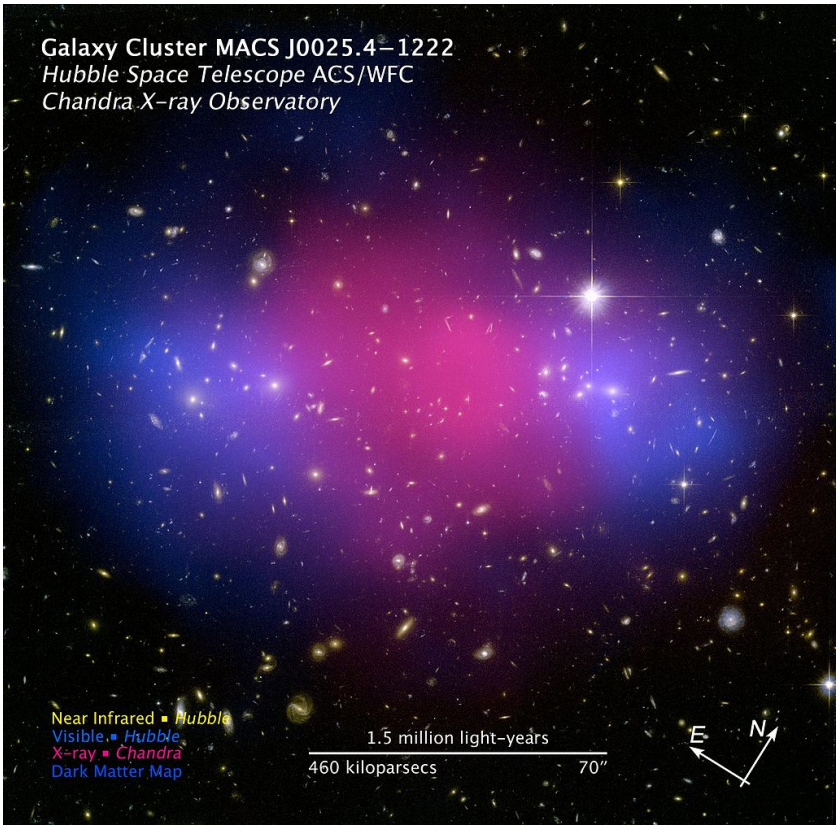

FIGURE 2.6: MACS J0025.4-1222 Composite Credit: X-ray(NASA/CXC/Stanford/S.Allen); Optical/Lensing(NASA/STScI/UC Santa Barbara/M.Bradac)

2.4.1 Theories for Dark Matter

One can pose the question of whether dark matter is relativistic or not. Relativistic dark matter, which is presumed to be low mass particles, is dubbed "Hot dark matter" (HDM) while non-relativistic dark matter, which is presumed to be high mass, is dubbed "Cold dark matter" (CDM). CDM is the favored theory [24] because of structure formation arguments. The standard theory [26] on structure formation assumes that the early universe was mostly, but not perfectly, homogeneous. The action of gravity amplifies the density contrast over time, leading to the formation of galaxies and clusters when the self gravity of a dense region allows it to decouple from the overall Hubble expansion of the universe. HDM scenarios would wipe out structures larger than galaxies in the standard theory because it would decouple too soon in the early universe to allow for such large scale formation. Therefore, the HDM picture of structure formation is "top down", large structures form first and fragment into smaller ones. Conversely, in the CDM picture, only small scale structures (sub-galactic) are wiped out. The CDM picture is a "bottom up" one where small scale structures form first.

The nature of dark matter is still unknown. A promising theory is that dark matter is composed of weakly interacting massive particles (WIMPs). Many beyond the standard model models exist which are well motivated and provide a WIMP candidate. One such theory is Supersymmetry (SUSY). For a detailed look at SUSY see [27]. The SUSY WIMP candidate commonly studied is the neutralino, which is the lightest supersymmetric partner (LSP).

2.4.2 Identifying the Nature of Dark Matter

There are currently thought to be three detection categories for Dark Matter. They are: direct production at particle colliders, direct detection by scattering, and indirect detection. There are many different ways to carry out such experiments and all three categories are heavily populated. An indirect detection mechanism for detecting neutralinos is to observe pair annihilation products [28]. Neutralino pairs may annihilate to standard model particles. Due to charge conservation both matter and antimatter must result. The antimatter channel, consisting of positrons and light antinuclei, has the possibility of being observed due to the relatively low abundance of antimatter sources from known physical processes. The positron fraction is of interest and has recently been refined by the AMS-02 collaboration [29]. The antiproton flux was recently measured by the PAMELA and AMS-02 collaborations and is consistent with secondary production, such as high energy protons interacting with the interstellar medium (ISM), alone [12] [30].

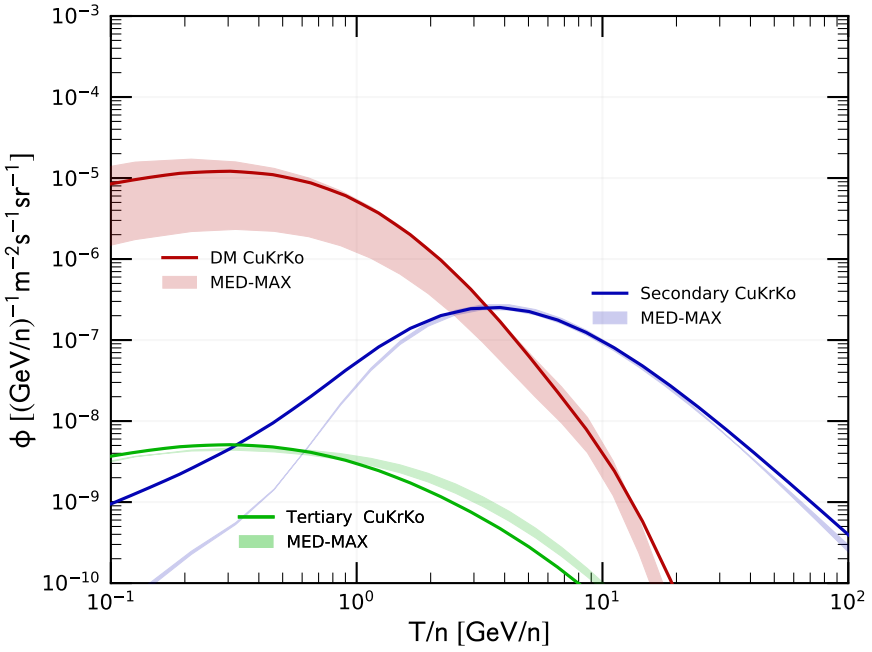

FIGURE 2.7: The blue curve shows the predicted secondary antideuteron flux from an analysis perform by Korsmeier, Donato, and Fornengo [17]. A typical value of the coalescence momentum (160 MeV/c) was used.

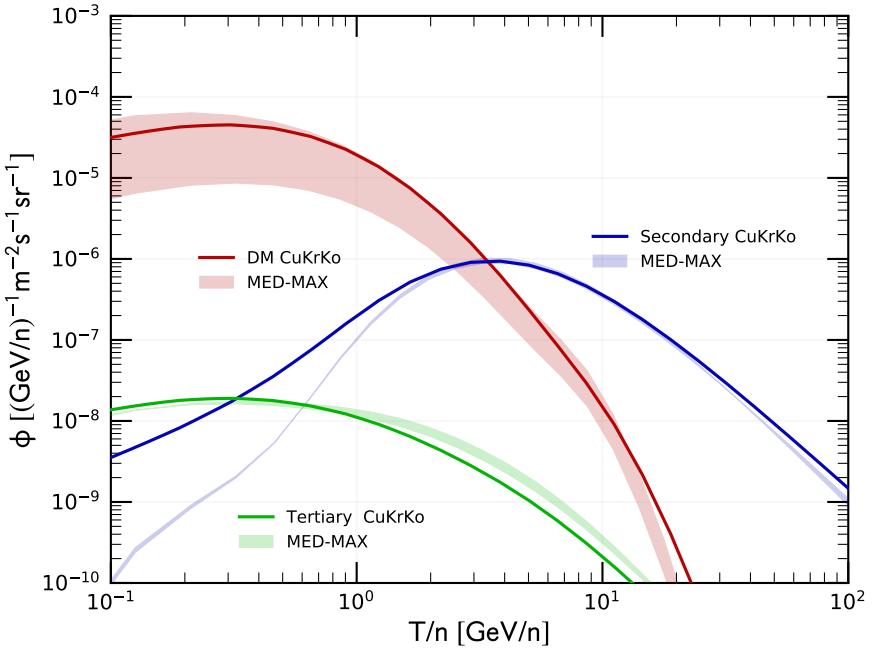

FIGURE 2.8: The blue curve shows the predicted secondary antideuteron flux from an analysis perform by Korsmeier, Donato, and Fornengo [17]. A large value of the coalescence momentum (248 MeV/c) was used.

Antideuterons originating from neutralino annihilation peaks in the couple of GeV energy range [31]. SUSY neutralinos are but one of many potential WIMP candidates that can produce antideuterons. A more general approach begins with the assumption that some dark matter candidate produces $b\bar{b}$ quark-antiquark pairs which eventually result in antideuterons [17] [32]. Using this approach the DM antideuteron signal is predicted to be 4-5 orders of magnitude greater than the astrophysical background at very low energies (Figs 2.7 and 2.8). There is a significant depletion in the expected secondary production rate for antideuterons in this energy range. This depletion is due to kinematical effects from the secondary production mechanism. For antideuterons at energies of about 1 GeV/n, the annihilation signal reaches nearly two orders of magnitude above the background from secondary production. MED-MAX refers to the uncertainty of the flux due to the uncertainty of galactic propagation parameters, particularly the DM halo size. The detection of antideuterons will be a huge step forward. The antideuteron search is "...very promising for dark matter searches." [33]

2.5 The AMS-02 Experiment

The Alpha Magnetic Spectrometer (AMS-02) is a space-based particle detector installed on the International Space Station (ISS). Its mission is to measure the cosmic ray spectrum including isotopic abundances from 500 MeV/c up to about 1 TeV/c particle momentum per nucleon.

AMS-01, the successful precursor, flew aboard the Space Shuttle Orbiter Discovery for ten days in June 1998. The detector collected over one hundred million cosmic ray events during a collection period of about 180 hours, producing significant results [34–36].

Fig. 2.9 shows a schematic view of the final AMS-02 detector layout. The detector is comprised of:

- A twenty layer Transition Radiation Detector (TRD).
- A four layer Time of Flight (TOF) system.
- A permanent magnet.
- A nine layer silicon tracker.
- An Anti Coincidence Counter (ACC).
- A Ring Imaging Cherenkov Counter (RICH).
- A 3D sampling electromagnetic calorimeter (ECAL).

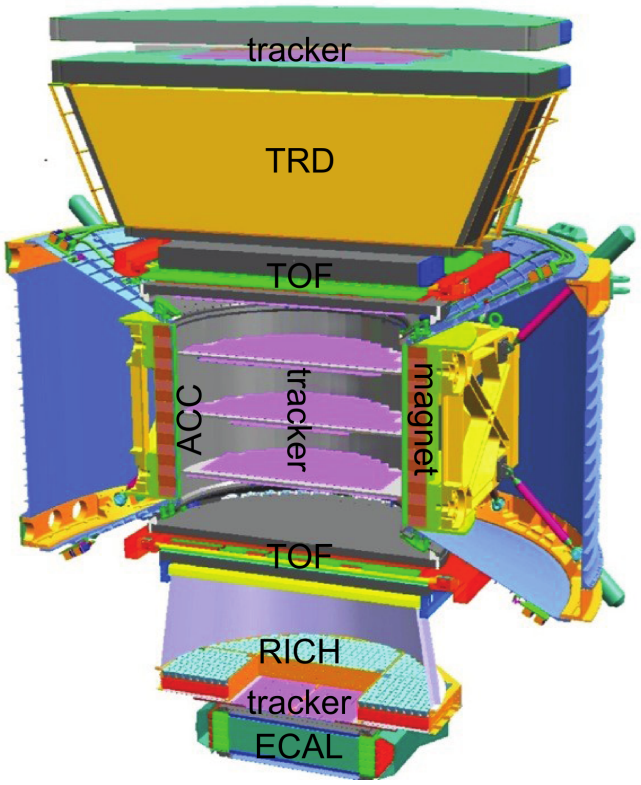

FIGURE 2.9: Schematic view of the AMS-02 experiment highlighting the various sub-detectors.

It is useful to define the coordinate system of AMS-02 for reference. Cartesian coordinates are used, with the origin located at the center of the AMS-02 magnet. The Z axis runs along the vertical axis of AMS-02, with positive Z oriented towards the TRD and negative Z oriented towards the ECAL. The X axis is oriented parallel to the AMS-02 magnetic field while the Y axis is oriented perpendicular. The YZ plane is sometimes referred to as the "bending plane" because charged particles are deflected by the magnetic field in this plane only.

2.5.1 TRD

Transition radiation is produced by highly relativistic charged particles (Lorentz factor $\gamma \geq 500$) passing through the 20 mm thick fleece radiator material (density of 0.06 g/cm^3, 10 μm polypropylene/polyethylene fibers.) The transition radiation photons are detected in proportional mode straw tube modules filled with a Xe/CO_2(80%|20%) gas mixture at a pressure of 900 mBar. The TRD consists of 20 straw layers separated by 20 mm fleece radiators (Fig. 2.10). Modules consist of 16 straw tubes with an inner diameter of 6 mm made out of a double layer kapton-aluminum foil of 72 μm wall thickness. A gold plated 30 μm thick tungsten wire is fixed to polycarbonate endpieces and is used as the sense wire. The modules are mechanically stabilized by longitudinal and vertical carbon fiber stiffeners. The 20 layers total 328 straw

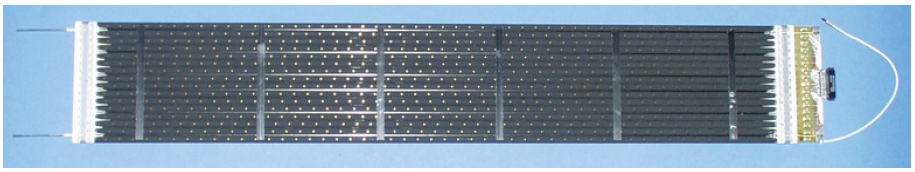

FIGURE 2.10: A completed TRD module.

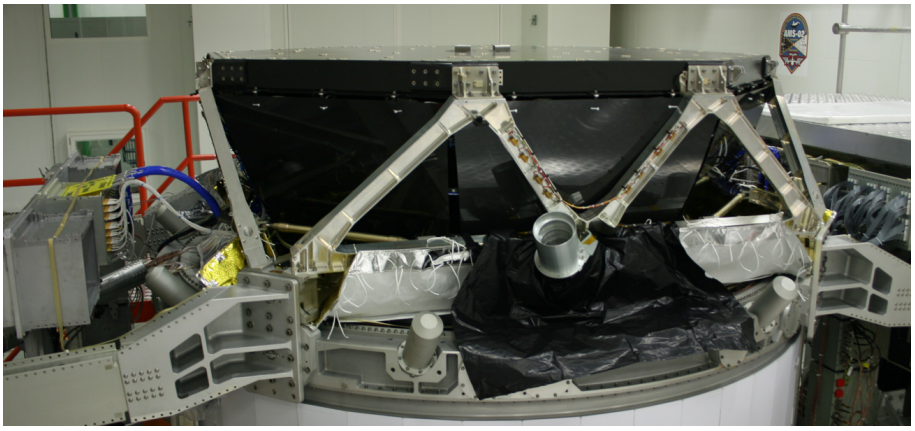

FIGURE 2.11: The Transition Radiation Detector is seen integrated on the top of the AMS-02 detector.

tube modules of lengths up to 2 m. They are arranged in a conical shaped octagon structure (Fig 2.11). The top and bottom four layers are oriented parallel to the AMS-02 magnetic field while the inner 12 layers run perpendicular to provide 3D tracking. An analog pulse height readout is used to distinguish efficiently wire signals due to pure ionization losses (hadrons) from signals containing both $\mathrm{d}E/\mathrm{d}X$ and absorbed transition radiation photons (electrons, positrons). Using this technique, the TRD selects electrons and positrons with 90% efficiency and rejection power from hadrons > 1000 in energy range 3 - 100 GeV [37].

2.5.2 TOF

The TOF [28, 38] (Fig. 2.12) system provides the fast trigger to the experiment, measures the velocity β and absolute charge Z of charged particles, and distinguishes up-going (in the detector frame) from down-going particles at the 10^{-9} level.

The four planes contain in total 34 scintillators read out by fine-mesh Hamamatsu R5946 PhotoMultiplier Tubes (PMTs) and are separated into two units with a Z separation of 127.3 cm. The Upper TOF (UTOF), containing layers 1 and 2, is placed on top of the magnet just below the TRD. The central Z position of the UTOF is 63.65 cm above the detector center. Layer 1 contains 8 scintillator paddles (Fig. 2.13) oriented parallel to the magnetic field direction. Layer 2 is also comprised of 8 scintillator paddles. The layer 2 paddles are oriented perpendicular to the magnetic field. The Lower TOF (LTOF), containing layers 3 and 4, is placed just below

FIGURE 2.12: The upper and lower Time of Flight assemblies prior to integration.

the magnet above the RICH. The central Z position of the LTOF is -63.65 cm. Layer 3 contains 10 scintillator paddles oriented perpendicular to the magnetic field while layer 4 contains 8 paddles oriented parallel to the magnetic field. Each paddle is made of 1 cm thick EJ-200 polyvinyltoluene plastic scintillator manufactured by Eljen-Technology.

Central paddles are rectangular in geometry 12 cm wide and varying in length between 117 cm and 134 cm. Each of the central paddles have 2 PMTs mounted on each end, totaling 4 PMTs per rectangular paddle. The edge paddles are trapezoidal in shape to completely cover the acceptance of the tracker magnet while also minimizing weight. The edge paddles of Layers 2 and 3 are mounted with 8 PMTs each. The edge paddles of layers 1 and 4 are mounted with 6 PMTs each. The total PMT count for the TOF is 134. The paddles are slightly overlapped in order to avoid geometrical inefficiency.

The timing resolution of each counter has been measured to be less than 180 ps and is well parameterized by eq. 2.8 where $P_1 = (159 \pm 2)$ps and $P_2 = (79 \pm 1)$ps.

$$\sigma_t = \sqrt{\frac{P_1^2}{Z} + P_2^2} \tag{2.8}$$

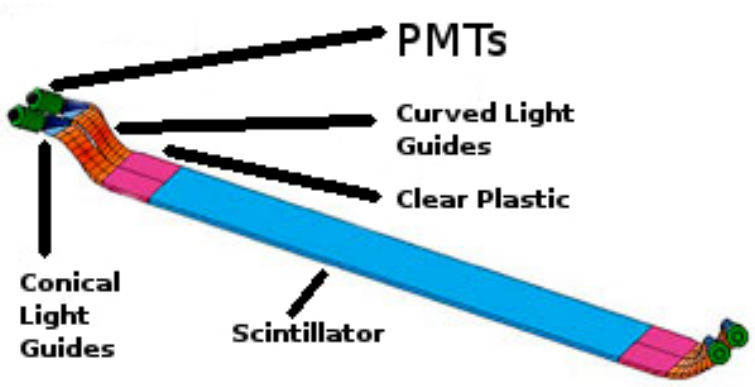

FIGURE 2.13: A schematic view of a rectangular Time of Flight paddle.

It is useful to estimate how the timing resolution translates to the velocity resolution for the TOF. For high velocity hadron tracks ($\beta \simeq 1$) particles traverse the detector in approximately straight lines. The path length between the upper and lower TOF will then be l_p. The vertical spacing between the upper and lower TOF is L and is 127.3 cm. The zenith angle is θ. The time that the particle takes to traverse the TOF is t. The particle velocity is v.

$$v = \beta c \tag{2.9}$$

Equation 2.9 defines particle velocity in terms of the speed of light, c.

$$t = \frac{l_p}{v} \tag{2.10}$$

Equation 2.10 relates the time which the TOF measures to the particle velocity and path length.

$$l_p = \frac{L}{\cos\theta} \tag{2.11}$$

The path length is found in terms of the separation distance of the upper and lower TOF and the track zenith angle in equation 2.11.

$$t = \frac{L}{c\beta\cos\theta} \tag{2.12}$$

The timing measurement is thus given by equation 2.12 and assuming Gaussian uncertainty yields the following.

$$\frac{\sigma_t^2}{t^2} = L^2\left[\frac{\sigma_v^2}{v} + \frac{\sigma_{\cos\theta}^2}{\cos^2\theta}\right] \tag{2.13}$$

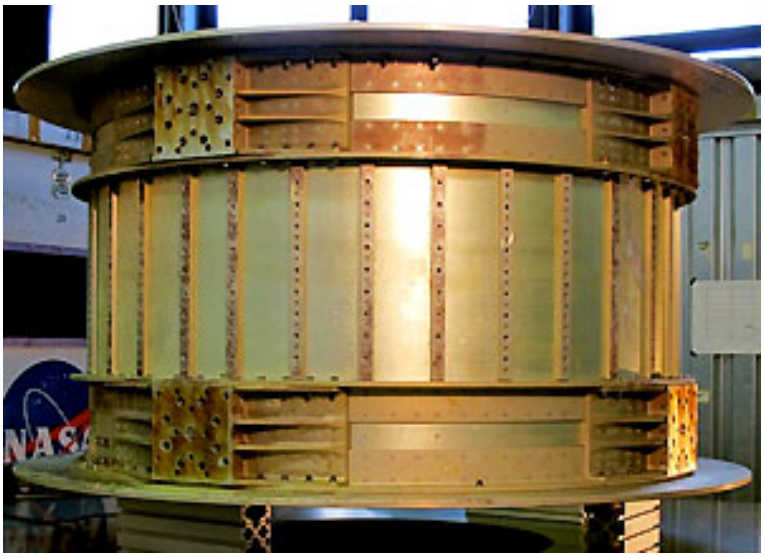

FIGURE 2.14: The permanent magnet.

The uncertainty of the zenith angle measurement is very small owing to the excellent resolution of the tracker. Therefore, this term may be dropped. Thus the velocity resolution simplifies for high velocity particles to:

$$\frac{\sigma_v}{c} = \frac{c \cdot \cos\theta}{L^2}\sigma_t \tag{2.14}$$

This rough approximation agrees well with data. The overall β resolution has been measured as about 4% for $\beta \approx 1$ protons.

2.5.3 Permanent Magnet

AMS-02 uses a permanent magnet [39] (Fig. 2.14) with a magnetic field of $B = 0.149$ T to bend charged particles in order to determine their rigidity. The magnet was flown on the AMS-01 detector in June of 1998 on the STS-91 mission.

Upon re-inspection of the magnet before it was integrated into AMS-02, the field was found to be unchanged from its 1998 state. The magnet consists of of 6400 Nd-Fe-B blocks of dimension 5 cm x 5 cm x 2.5 cm. The external field must be kept to a minimum to not affect torques on the station. The external field has been measured to be less than 3 G at a distance 2 m from the magnet center.

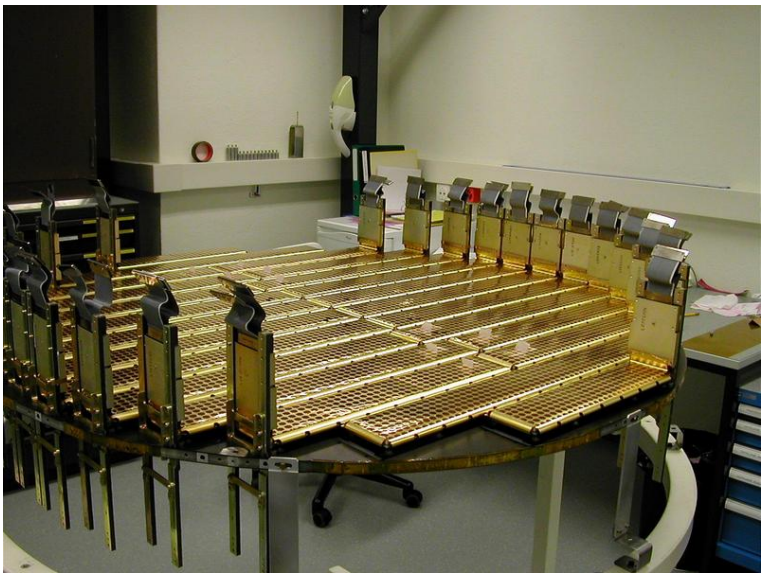

FIGURE 2.15: A view of one of the silicon tracker planes.

FIGURE 2.16: The inner tracker assembly being integrated into the permanent magnet.

2.5.4 Silicon Tracker

The silicon tracker [39] is composed of nine layers of silicon microstrip detector planes (Fig 2.15). Each silicon wafer has a thickness of 0.3 mm. The inner tracker (Fig 2.16) consists of three double planes within the magnet bore and a single plane at the top of the magnet bore. Two further planes were included to increase the lever arm of the tracker. Plane 1 is located above the TRD at 158.920 cm above the center of AMS-02. Plane 9 is located between the RICH and the ECAL at 135.882 cm below the center of AMS-02, completing the tracker. The silicon

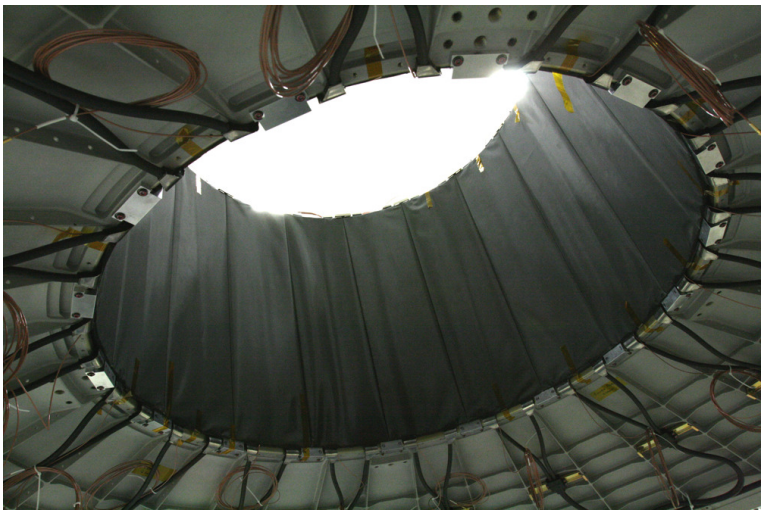

FIGURE 2.17: The assembled ACC as seen during integration.

strip detector consists of 192 ladders, containing the silicon sensors, readout electronics and mechanical support. In the bending plane the tracker has a single point resolution of 10 μm, and 30 μm in the non-bending plane. The mechanical stability of the inner tracker is monitored by a laser system. The laser system is comprised of 20 infrared beams which penetrate all inner tracker layers yielding a position accuracy of better than 5 μm. The tracker reaches a maximal detectable rigidity of 2.2 TV for protons. The measured rigidity resolution is 25% at 500 GV [40]. The signal amplitude from energy deposition in each tracker plane provides an independent measure of the particle absolute charge. The observed tracker charge resolution is close to 5% in the TOF regime of $\beta \leq 0.8$ for charge 1.

2.5.5 ACC

The inner tracker is surrounded by the ACC [41] (Fig. 2.17) system to ensure clean track reconstruction. The ACC has a modular design consisting of 16 curved scintillator panels (BC-414) each with a thickness of 8 mm and instrumented with wavelength shifting fibers. Each panel is 830 mm long and 220 mm wide. Scintillation light is guided to a connector where clear fiber cables guide it to fine-mesh PMTs (Hamamatsu R5946) mounted on the conical flange of the vacuum case. A hit in the ACC indicates that the event in question may be contaminated. For very high energy events, hard interactions may occur in the inner tracker, producing secondaries which may exit the detector through the sides and trigger the ACC. If a particle has a hard interaction with the magnet, spallation fragments may enter the tracking volume but will first cross the ACC. The ACC system detects and vetos particles which travel through the tracking volume from the side, outside the main acceptance, in coincidence with a particle going through

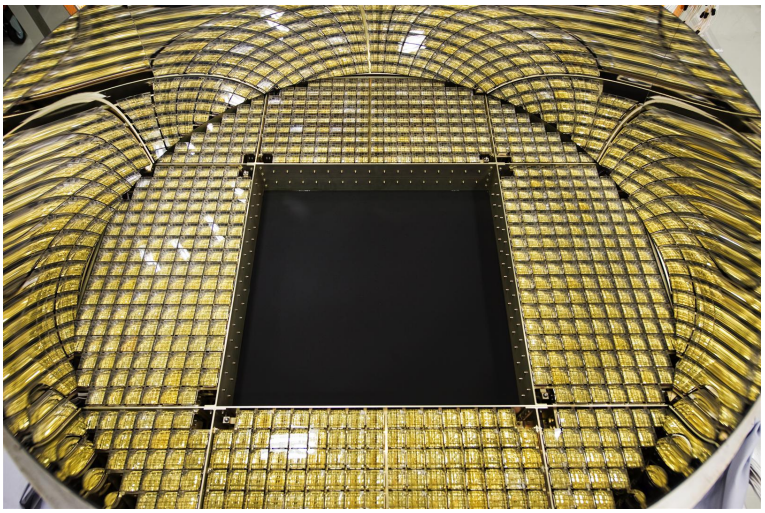

FIGURE 2.18: A view of the RICH conical mirror and the detection plane. The square hole is directly above the ECAL allowing charged particle to pass unabated.

the TOF system and the inner tracker. In these cases, the ACC provides a veto to ensure a clean event sample. The ACC detection efficiency is greater than 0.9999.

2.5.6 RICH

The RICH [42] is located between the lower TOF and the ECAL. The radiator consists of 92 tiles of silica aerogel (refractive index $n = 1.05$) of 2.5 cm thickness surrounding 16 tiles of sodium flouride ($n = 1.33$) of 0.5 cm thickness. The emitted photons are detected by 680 4×4 multi-anode PMTs at the detection plane. A conical mirror separates the radiator from the detection plane. This increases acceptance by reflecting Cherenkov rings back onto the detection plane which would otherwise not be visible. The detection plane and mirror can be seen in Fig. 2.18. The particle velocity is determined by measuring the Cherenkov angle with a precision of 0.001 on β. Absolute charge is determined by the intensity of emitted Cherekov light making up the cone, and allows nuclei determination up to iron.

2.5.7 ECAL

The ECAL [43] is located at the very bottom of AMS-02. The ECAL consists of 16.7 radiation lengths of a lead/scintillator fiber structure, providing 3D reconstruction of showers initiated by leptons and photons (Figs 2.19). The ECAL separates leptons from hadrons with an e/p-rejection of 10^4 in the energy range 1 GeV to 1 TeV. The ECAL energy resolution is well parameterized by:

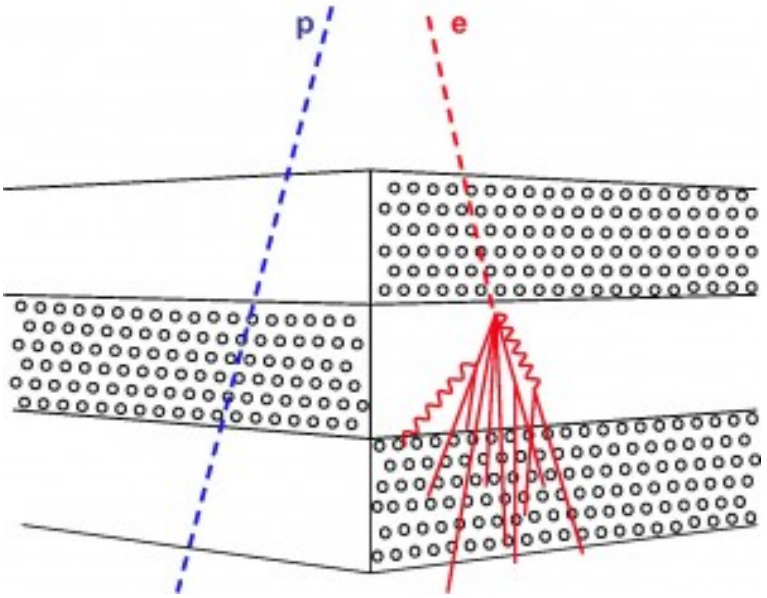

FIGURE 2.19: A diagram illustrating the shower differences between an electron and proton in the ECAL.

$$\frac{\sigma(E)}{E} = \frac{(10.4 \pm 0.2)}{\sqrt{\frac{E}{GeV}}} \oplus (1.4 \pm 0.05)\%. \tag{2.15}$$

2.6 The AMS-02 Monte Carlo

The AMS-02 detector has been modeled very precisely in the Monte Carlo simulations (MC). This is used to model high energy physics interactions of simulated particles traversing the detector volume. The GEANT4.10.4.1 physics package [44–46] is used to simulate physics interactions within the detector. Hadronic interactions are modeled using the QGSP BIC physics list. QGSP is the basic physics list applying the quark gluon string model for high energy interactions of protons, neutrons, pions, kaons, and nuclei. BIC refers to the Geant4 Binary Cascade for primary protons and neutrons with energies below 10 GeV. Nuclear capture of negative particles and neutrons at rest is handled using the Chiral Invariant Phase Space (CHIPS) model. Multiple Coulomb scattering is modeled by the Wentzel-VI MSC model.

Monte Carlo productions are for individual primary species. In the typical simulation scheme, particles are generated isotropically on a 3.9 m by 3.9 m square positioned 1 m above the top of the detector. The dimensions of the generation plane are such that the full field of view of the detector is covered. Particles are generated as a function of starting momentum proportional to the base-10 logarithm of the momentum, $log(p)$. This generation function is used because computation time increases for higher energy particles. The fact that the cosmic ray spectrum is

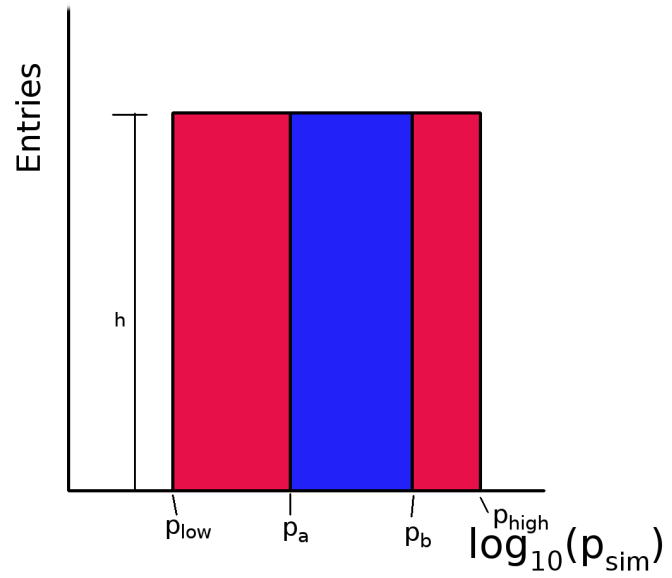

FIGURE 2.20: A cartoon demonstrating how to find the normalization for Monte Carlo.

steeply falling for all species above a few GeV/c implies that fewer simulated events are needed at higher energies.

It becomes necessary under many circumstances to use a spectrum that is not uniform in log momentum. In order to do this, individual events are reweighted by the required spectral shape. The derivative of the generation spectra with respect to momentum is found to be p_{gen}^{-1}. In order to go from this to a uniform derivative a weight factor of p_{gen} should be applied. This gives a spectra which is uniform in generated momentum. Then to obtain an input spectra of the desired spectral shape, one must multiply the uniform weight by the desired spectra.

$$w = f(p_{gen})p_{gen} \tag{2.16}$$

If one needs to proportionally know how many events would have been generated by that input spectrum, this too can be done. The initial generation spectra is uniform in logarithm momentum, with start momentum p_{low}, end momentum p_{high}, and total generated events N_{gen}. Picturing this graphically, Fig. 2.20, with a logarithmic axis, one has a rectangle of area N_{gen} and width log(p_{low}) - log(p_{high}). The subtraction of logarithms simplifies to log(p_{low}/p_{high}). The "height", h, of the rectangle is then N_{gen} / log(p_a/p_b). For a given bin of width Δp_{gen},

the reweighted number of generated events, N', is then the integral of the reweighting function times the "height".

$$N'(p, p + \Delta p) = \frac{N_{gen}}{log\left(\frac{p_a}{p_b}\right)} \int_p^{p+\Delta p} f(p)dp \tag{2.17}$$

Chapter 3

Antiparticle Flux Analysis

In cosmic-ray experiments it is typical to measure the particle flux. Particle flux is calculated using:

$$\Phi(p) = \frac{N_{obs}(p)}{A(p)C(p)\epsilon_{trig}(p)T_{meas}(p)\Delta p}. \tag{3.1}$$

The components which go into $\Phi(p)$, the particle flux as a function of momentum, are $N_{obs}(p)$, the number of observed events, $A(p)$, the geometrical acceptance, T_{meas}, the measurement time, $\epsilon_{trig}(p)$, the trigger efficiency, Δp, the momentum bin width, and $C(p)$, a correction factor. The following chapter will present in detail how each flux parameter is calculated with respect to the AMS-02 Galactic antiproton analysis.

3.1 Identification Considerations for Antideuterons

AMS-02 is a large mass spectrometer. The instrument principally measures particle rigidity (momentum per unit charge), particle velocity, and energy depositions. Particle charge may be measured using the energy depositions in the various sub-detectors. By combining the reconstructed rigidity, velocity, and charge, the particle mass may be reconstructed according to:

$$m = ZR\sqrt{\left(\frac{1}{\beta^2}\right) - 1}. \tag{3.2}$$

Z being the particle charge, R the particle rigidity as measured by the tracker, and β the particle velocity/c.

In practice, the measured particle charge is assumed to be integer to determine the reconstructed mass. The first step of any analysis is to determine the particle charge. The particle charge is measured by multiple sub-detectors in AMS-02. The identification of antideuterons begins by identifying $Z = -1$ particles.

$Z = -1$ data will contain principally electrons, muons, pions, kaons, antiprotons, and antideuterons. This represents the focus species and backgrounds. The potential dark matter antideuteron signal is maximal below a few GeV/n according to Fig. 2.7. Charge confusion, the misidentification of the charge sign, by the tracker is negligible for such low rigidities and therefore charge confused protons may be excluded as a potential background for a low momentum analysis. Of the negative charged backgrounds, electrons are most abundant. For the velocity range of this analysis the momentum of an electron is less than 1 MeV/c. The rigidity range is limited by a restriction on the reconstructed mass. At rigidity 1 GV electrons are highly relativistic and will emit transition radiation in the TRD. Combining the rejection power of the TRD with reconstructed mass allows electrons to be safely excluded by AMS-02.

Muons, pions, kaons, and antiprotons are the most significant background for identification of antideuterons with AMS-02. Pions (rest mass 139.57 MeV/c^2) and muons (rest mass 105.66 MeV/c^2) are close enough in mass to be lumped together and will henceforth only be identified as pions. Pions and kaons are produced near the detection volume by high energy interactions between cosmic rays and nearby material. Antiprotons may also be produced in such a way, but are also present in the cosmic radiation itself.

Muons, pions, and kaons are unstable and will decay rapidly. We should only consider the negative singly charged species. The μ^- half life is 2.2×10^{-6}s, the π^- half life is 2.6×10^{-8}s, and the K^- half life is 1.2×10^{-8}s. The next longest lived negative singly charged particle is the Ξ^- with a half life of 1.6×10^{-10}s. The classical decay length of an unstable particle is the half life multiplied by the velocity. Even at a β of 0.6 a kaon may pass through the detector if generated nearby. But even a β of 0.6 is relativistic and relativistic time dilation should be considered. The relativistic time dilation formula is given in Eq. 3.3. Due to time dilation an unstable particle appears to exist longer from the reference frame of a stationary observer. Thus an unstable particle will have a longer decay length when considering relativistic effects. The range, r, an unstable particle can travel is thus given by Eq. 3.4. It is shown in Fig 3.1 that it is safe to ignore Ξ^- baryons because they only travel a few centimeters for the highest velocities considered in this analysis.

$$t' = \frac{t_0}{\sqrt{1-\beta^2}} \tag{3.3}$$

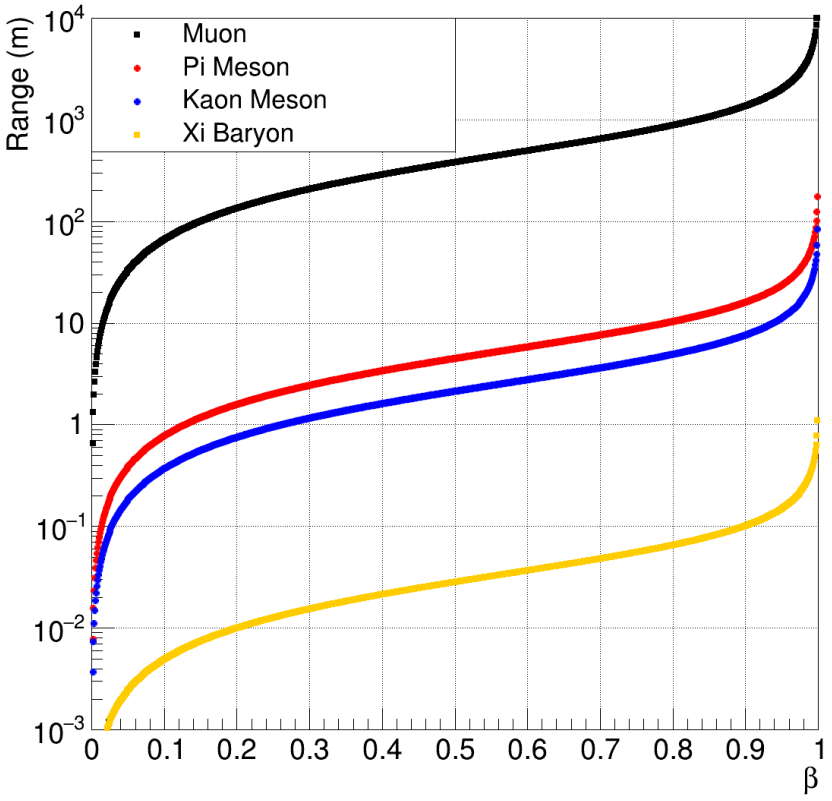

FIGURE 3.1: Decay lengths of the considered background particles. If the decay length is of the order of 1 m the particle may traverse the detector volume if it was generated near the top of the detector.

$$r = \beta c t' \tag{3.4}$$

In order to separate pions, kaons, and antiprotons from antideuterons, AMS-02 will rely mostly on mass reconstruction. Antiprotons are of particular importance because of their closeness in mass to antideuterons. Due to the finite mass resolution of AMS-02, antiprotons constitute an irreducible background for antideuterons which must be studied in great detail. The following sections will detail such analysis of the antiproton flux in Low Earth Orbit. The antiproton flux measurement is used as a calibration tool of sorts to ensure the techniques used for the antideuteron sensitivity are valid. By combining the measured antiproton flux with MC the antideuteron sensitivity for AMS-02 can be estimated.

The majority of the quality cuts to be presented were adapted previous work [47]. A boosted decision tree analysis was performed to minimize the number of MC proton statistics which had a reconstructed mass in the range corresponding deuterons, called fake events, while maximizing the overall proton efficiency. The deuteron mass range was not allowed to vary and was selected

to be 1.50-2.25 GeV/c^2. Many potential cuts were analyzed independently. The cut variables were iterated on in integer steps for integer variables and steps of 0.1 for continuous variables. The resulting cuts were then used as a starting point for this analysis and further quality cuts have been added.

3.2 Galactic Low-Energy Antiproton Flux Analysis

3.2.1 Quality Cuts

In order to identify antiprotons from other particles quality cuts must be applied to the data to select a good sample. First, only periods of time where the detector is operating normally are selected. Next, minimum level cuts are applied to assure that necessary measurements have been made. Lastly, the quality cuts are applied. The complete list of cuts is given in tables 3.1, 3.2, 3.3, and 3.4. The bad run cuts will not be discussed further as they are mission specific and only hold meaning for AMS-02 analysis.

Typically the ISS is oriented such that AMS-02 points about 12 degrees from the zenith. There are times when the station is reoriented, such as during some vehicle approaches, during reboost maneuvers, and when performing collision avoidance with space debris. The BadFacingAngle cut removes these off nominal pointing conditions from the analysis.

The AMS-02 trigger was designed to operate at about 1 kHz in order to manage data taking. During extremely high radiation periods the trigger rate can be much higher than 1 kHz, causing a reduced trigger efficiency. The BadLiveTime cut ensures that the livetime is ≥ 0.5 to exclude these time periods.

Thermal transients cause the AMS-02 detector structure to expand and contract. An infrared laser system constantly monitors the alignment of the inner tracker planes. The external tracker layers, layer 1 and layer 9, are particularly prone to thermal effects and are unfortunately not monitored by the laser system. Instead, Galactic cosmic rays are used to confirm the alignment of layer 1 and layer 9. Two algorithms are used to compute the plane alignment. If the alignment differs by 35 μm or more between the two algorithms for layer 1, or if the alignment differs by more than 45 μm between the two algorithms for layer 9, the planes are considered misaligned. The GoodAlignment cut ensures that only data taking periods where all tracker planes are properly aligned are used. The other unfavorable data taking cuts are hardware specific and will not be discussed.

TABLE 3.1: Exclude bad runs as tagged by the AMS-02 data team.

BadRun(General)
BadRun(DAQ)
BadRun(TOF)
BadRun(Tracker)
BadRun(TRDD)
BadRun(Ecal)

TABLE 3.2: Exclude unfavorable data taking periods.

RTIdataAvailable
MostEventsTriggered
SecondWithinRun
BadReconstructionPeriod
NoMissedEvents
GoodAlignment
BadLiveTime
NoHardwareErrors
BadFacingAngle

TABLE 3.3: Minimum cuts for negative particles.

SingleAMSParticle
SingleTrackerTrack
HasTrackerTrack
HasTrackerTrackFit
HasTofBeta
NegativeRigidity
Downgoing
NotInSAA
NotInSolarArrayShadow

3.2.2 Minimum Cuts

As a minimum criteria the cuts in Tab. 3.3 are applied to events. To begin with, events which have a tracker track, a fit to that tracker track, and a TOF velocity measurement are chosen. In the overall AMS-02 analysis framework, events with a single particle object are selected. In addition, only events with a single reconstructed tracker track are selected. The philosophy behind these cuts are to exclude events which are interaction products from nearby AMS-02. Only down-going particles with respect to AMS-02 are chosen. This means that a particle enters the TRD (top) side of AMS-02 and exits the ECAL (bottom) side. Downgoing particles have positive velocity as measured by the TOF. Particles with negative rigidity are selected. When combined with the down-going cut, this selects negatively charged particles. The ISS has very large solar arrays for power generation. During certain periods of time during flight, the shadow of these solar arrays covers AMS-02 for extended periods of time. The detector gets cold and

TABLE 3.4: Quality cuts used for low-energy antiparticle analysis.

Cut					Cut Group
Tracker Track Zenith Angle at L2			$\leq$	45°	Fiducial Cuts
Tracker Track Zenith Angle at RICH Radiator			$\leq$	45°	Fiducial Cuts
Tracker Track Radius at Z = 0			$<$	47.0 cm	Fiducial Cuts
Extrapolated Tracker Track RICH crossing radius			$<$	80.0 cm	Fiducial Cuts
TOF Clusters Associated with AMSParticle	$=$	4			Hits Cuts
TOF Clusters NOT Associated with AMSParticle			$\leq$	1	Hits Cuts
ACC Hits			$\leq$	1	Hits Cuts
Inner Tracker XY Hits	$\geq$	5			Hits Cuts
RICH Hits			$\leq$	7	Hits Cuts
Tracker Track TOF Hit Matching					Track Matching Cuts
TRD Vtrack Tracker Track residual azimuth angle at UTOF			$<$	6.27°	Track Matching Cuts
TRD Vtrack Tracker Track residual zenith angle at UTOF			$<$	2.19°	Track Matching Cuts
Total UTOF Energy Deposition	$>$	3.0 MeV			Charge Cuts
Total LTOF Energy Deposition	$>$	3.0 MeV			Charge Cuts
Tracker Charge	$>$	0.700	$<$	1.300	Charge Cuts
Overall TOF Charge	$>$	0.700	$<$	1.300	Charge Cuts
UTOF Charge	$>$	0.700	$<$	1.300	Charge Cuts
LTOF Charge	$>$	0.600	$<$	1.300	Charge Cuts
Tracker Track Normalized χ^2 X			$<$	4.0	χ^2 Cuts
Tracker Track Normalized χ^2 Y (bending plane)			$<$	2.0	χ^2 Cuts
TOF BetaH Spatial Normalized χ^2			$<$	2.0	χ^2 Cuts
TOF BetaH Timing Normalized χ^2			$<$	8.0	χ^2 Cuts
Clean TRD Cut					TRD Likelihood Cuts
TRD Active Layers (Used in likelihood calculation)	$\geq$	10			TRD Likelihood Cuts
TRD Electron Proton Log Likelihood	$\geq$	0.4			TRD Likelihood Cuts
TOF Truncated Mean $\mathrm{d}E/\mathrm{d}x$ Cut (remove pions and kaons)					$\mathrm{d}E/\mathrm{d}x$ Cut
No TRD Vertices					TRD Vertex Cut

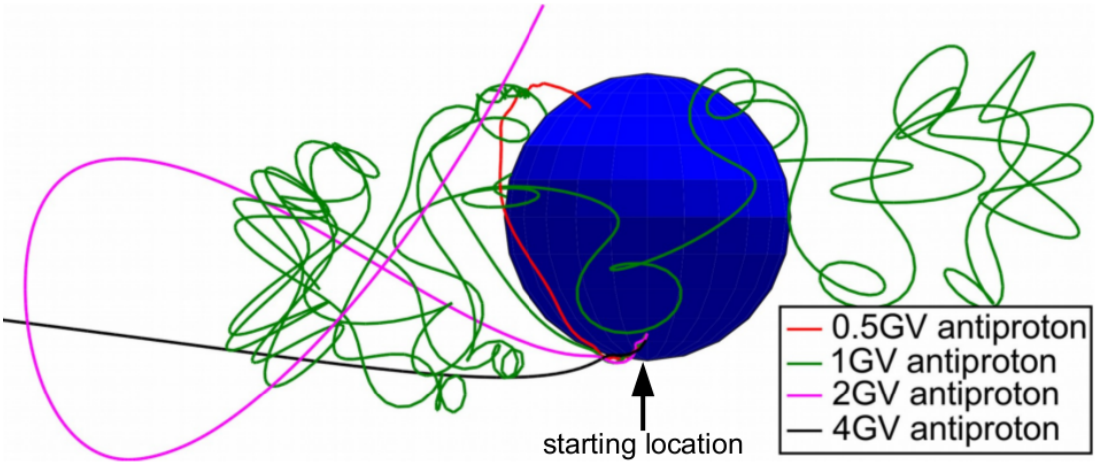

FIGURE 3.2: Backtraced antiprotons with various energies from the same generation location and direction. It is observed that above a certain rigidity the particle no longer re-impacts the Earth. [48]

goes into a healthy, but off nominal, thermal condition. Time periods when AMS-02 is in the solar array shadow are excluded to limit the analysis to nominal thermal conditions.

The Earth's magnetic field can be approximated as a dipole field, tilted off axis from the Earth's axis of rotation, and slightly offset from the geographic center. The South Atlantic Anomaly, SAA, is a region where the geomagnetic field appears to dip close to Earth, because the field is offset from the geographic center. It is in this geographic region, centered over the south Atlantic ocean, where the inner Van Allen radiation belt makes its closest approach to the surface of the earth. The radiation environment is much more intense in the SAA than elsewhere at similar geomagnetic latitudes. The effect on AMS-02 is a high trigger rate because of the intense particle flux. Flight times in this region are excluded for the Galactic flux analysis.

3.2.3 Rigidity Cutoff For Cosmic Rays by Earth's Magnetic Field

Charged particles moving through a magnetic field will experience a force if the velocity of the particle has a component perpendicular to the magnetic field. The Lorenz force is defined as:

$$\overrightarrow{F} = q\overrightarrow{v} \times \overrightarrow{B}. \tag{3.5}$$

It is convenient to define particle rigidity, R, as momentum per unit charge. Rigidity has units of GV.

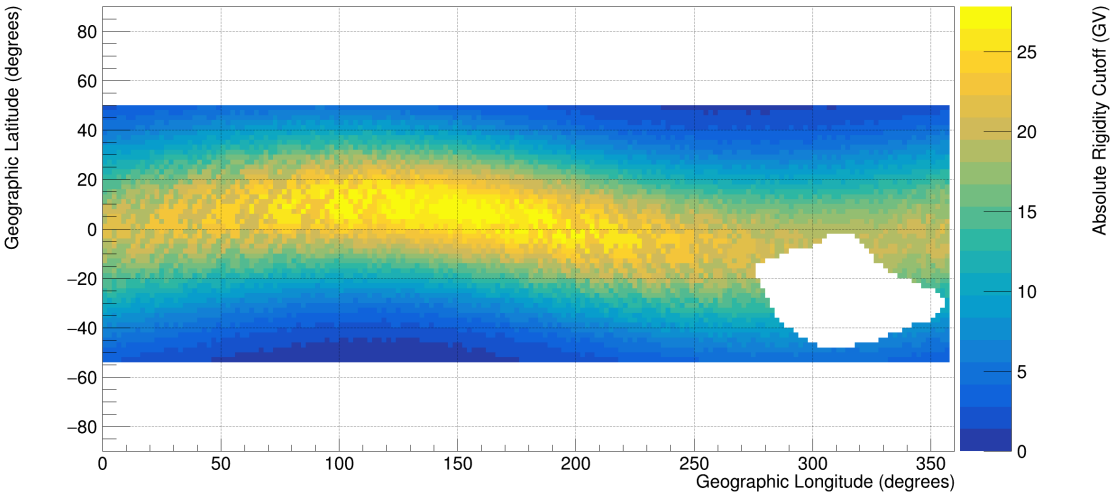

FIGURE 3.3: The geomagnetic cutoff using the Stöermer approximation for the AMS-02 field of view along the ISS flight path. The SAA has been excluded.

$$R = \frac{\gamma \beta m_0}{Z} \ . \tag{3.6}$$

The Earth has a magnetic field approximated as a dipole. Cosmic rays which impinge upon the Earth will experience a Lorenz force which will bend their trajectory. The rigidity at which particles are either deflected away from or penetrate to a reference point is known as the cutoff rigidity [49]. The cutoff rigidity for a certain reference position will in general vary with respect to zenith angle. For the following analysis, the Stöermer approximation [50] will be used to estimate cutoff rigidity values. Charged particles are backtraced to 50 Earth radii using the Stöermer approximation for the magnetic field. Particle rigidity as well as generation zenith angle with respect to the detector are varied. If a particle can escape the 50 Earth radii limit, it is above cutoff. In this way the rigidity cutoff can be obtained for different detector field-of-views and for every geographic position. Given a satellite flying in circular Low Earth Orbit inclined to the magnetic equator, the rigidity cutoff will be maximum at the magnetic equator and minimum nearest to the magnetic poles. For a flight altitude of 400 km and orbital inclination of 51 degrees, the rigidity cutoff varies between about 0.5 GV and 50 GV (Fig. 3.3).

A common technique to distinguish between Galactic cosmic rays and albedo space radiation is to impose that the measured rigidity of the particle is above the rigidity cutoff at the measurement location. Further, a safety factor on the cutoff value is usually used due to uncertainties in the cutoff model. This leads to two distinct classes of cosmic rays. Above cutoff cosmic rays are those which originate beyond Earth's magnetosphere. These are called Galactic cosmic rays. Sub-cutoff cosmic rays can not escape Earth's magnetosphere. Sub-cutoff cosmic rays are

mostly formed by Galactic cosmic rays interacting with Earth's atmosphere. The sub-cutoff radiation may have short or long lifetimes before they re-impact the atmosphere [51–53].

3.2.4 Quality Cuts for Low-Energy Antiparticles

It is useful to analyze variable distributions after all quality cuts have been applied, except for the cut on the variable in question. This is known as the "last cut" distribution. B1128 antiproton Monte Carlo was used with events given a weight such that the generated momentum spectra is uniform. Further, TOF velocity is restricted to β 0.60-0.80 because this is a velocity range where the TOF works particularly well.

3.2.4.1 Charge Determination

The first step towards identifying antiprotons is to select $|Z| = 1$. The charge selection for this analysis is done using the TOF and tracker. The RMS of the tracker and TOF charge distributions may be used to approximate the charge resolution of each detector. The tracker has a measured charge resolution of 0.052 for low velocity $|Z| = 1$ particles. The TOF has a measured charge resolution of 0.047 for low velocity $|Z| = 1$ particles. The TOF can further be subdivided into the upper and lower TOF for two more measurements of charge. The upper TOF has a measured charge resolution of 0.065 for low velocity $|Z| = 1$ particles while the lower TOF has a measured charge resolution of 0.074.

An event is selected if the tracker charge is measured between 0.700 to 1.300 charge units. The same range is chosen for the overall TOF charge and UTOF charge. The range is widened to 0.600 to 1.300 charge units for the LTOF charge measurement. Figs. 3.4, 3.5, 3.6, and 3.7 show the last cut distribution for the charge variables using the B1128 antiproton Monte Carlo. The vertical black lines show the cut positions, and the red and blue lines show the resolution range centered about the cut. The slight bias of the peak is due to the charge calibration being optimized for high rigidity particles. The lower velocity range produces larger energy depositions which in turn translate to an apparently higher measured charge. This peak bias as well as the right skewed nature of the actual charge distributions means that the seemingly large charge selection range is in fact appropriate for maintaining cut efficiency while at the same time ensuring a good charge measurement.

In order to determine the mass of a particle assuming integer charge, the rigidity and velocity of the particle must be measured at the same location in the detector. In order to obtain the best mass resolution, quality cuts must be applied to the rigidity and velocity measurements.

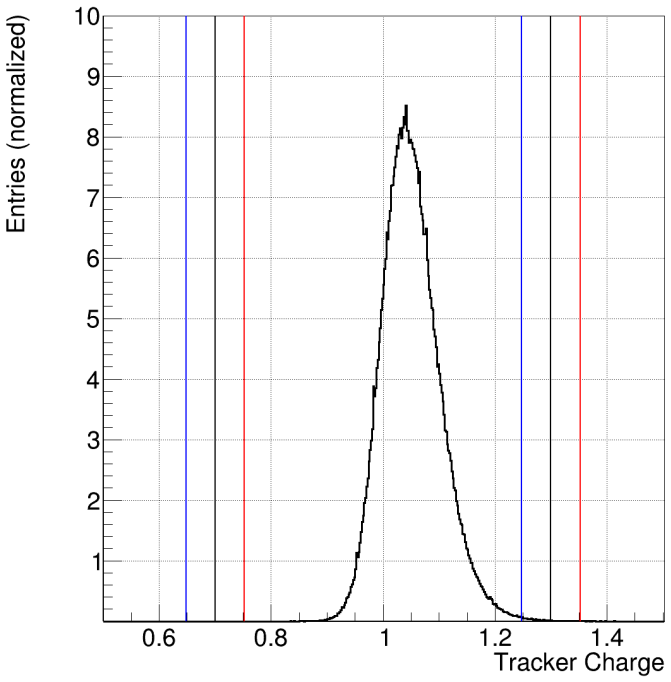

FIGURE 3.4: The tracker charge for B1128 antiproton MC. The vertical black lines represent the cut bounds. The vertical red and blue lines bound the charge resolution around the cut position.

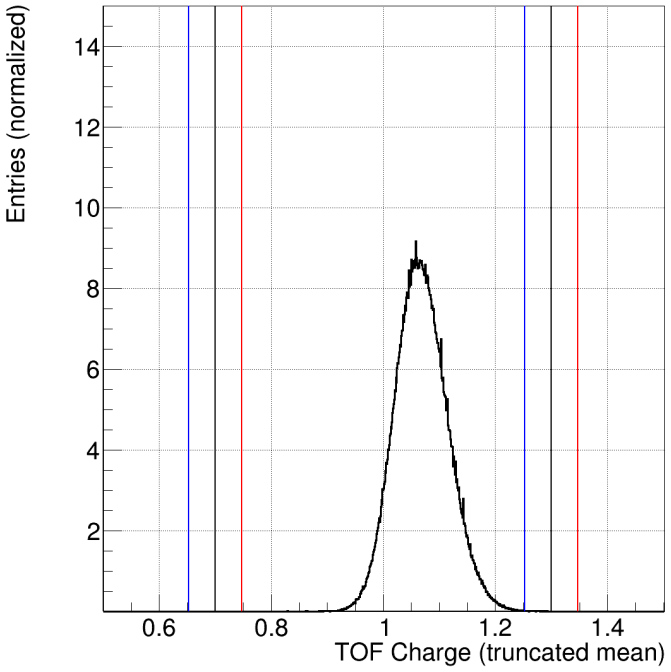

FIGURE 3.5: The TOF charge for B1128 antiproton MC. The vertical black lines represent the cut bounds. The vertical red and blue lines bound the charge resolution around the cut position.

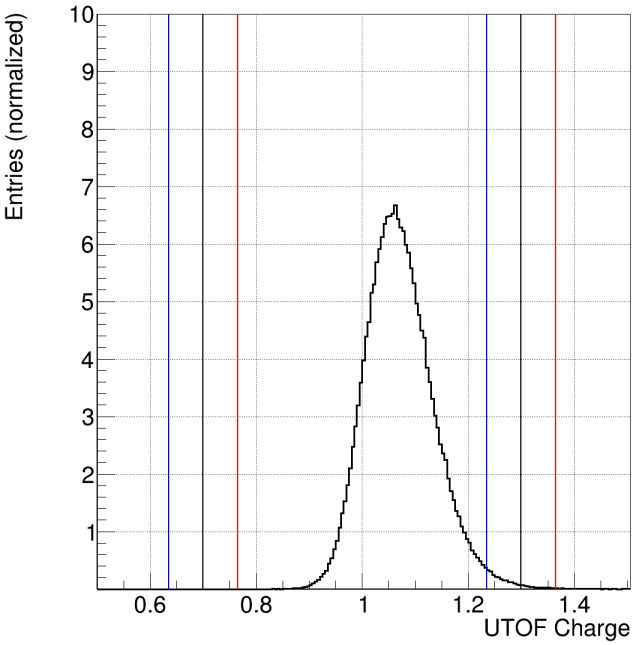

FIGURE 3.6: The upper TOF charge for B1128 antiproton MC. The vertical black lines represent the cut bounds. The vertical red and blue lines bound the charge resolution around the cut position.

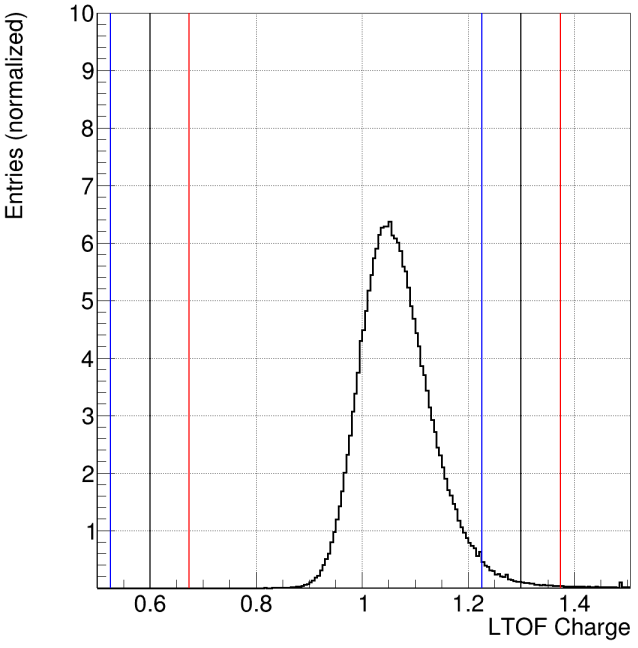

FIGURE 3.7: The lower TOF charge for B1128 antiproton MC. The vertical black lines represent the cut bounds. The vertical red and blue lines bound the charge resolution around the cut position.

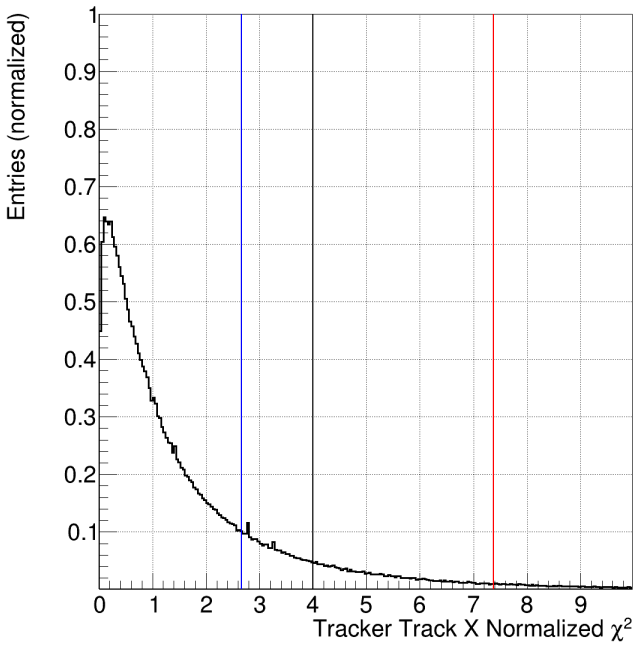

FIGURE 3.8: The tracker track fit χ^2/n.d.f. for the X (non-bending plane) component of the Choutko algorithm for B1128 antiproton MC. The black vertical line shows the cut value. The red and blue vertical lines represent the ± 10% efficiency of the cut.

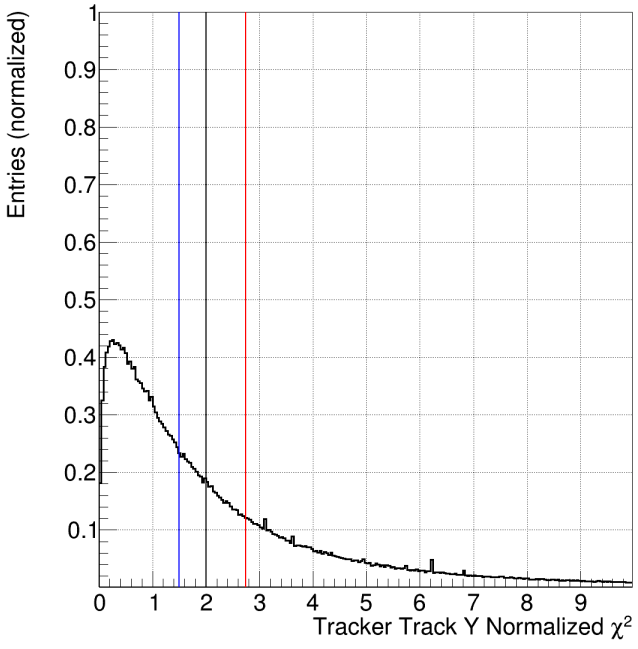

FIGURE 3.9: The tracker track fit χ^2/n.d.f. for the Y (bending plane) component of the Choutko algorithm for B1128 antiproton MC. The black vertical line shows the cut value. The red and blue vertical lines represent the ± 10% efficiency of the cut.

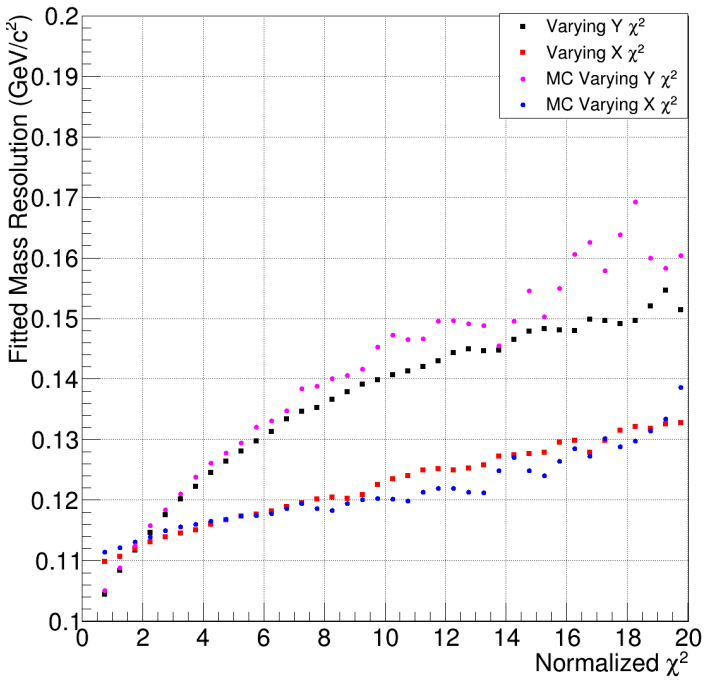

FIGURE 3.10: Mass resolution as a function of tracker χ^2. A few months of mostly proton ISS data was used. B1068 antiproton MC shows good agreement to data.

Particle rigidity is measured using the tracker. This analysis requires a minimum of 5 inner tracker XY hits associated with the AMS-02 particle. The tracker track fit is performed to determine the radius of curvature of the track and therefore the inverse rigidity. The fitting algorithm used is the Choutko method. The χ^2 / degrees of freedom is required to be less than 4.0 for the X fit, which is the non-bending plane (Fig. 3.8). The χ^2 / degrees of freedom is required to be less than 2.0 for the Y fit, which is the bending plane (Fig. 3.9).

The bending plane fit requirement is more rigorous than the non-bending plane because it affects mass reconstruction to a greater degree. Fig. 3.10 demonstrates this trend. The full quality cutset, with the exception of the normalized tracker χ^2 cuts, was applied to a few months of ISS data. The proton mass peak was reconstructed and fitted with a Gaussian and the standard deviation was taken to be the fitted mass resolution. A systematic trend is observed. Mass resolution is clearly correlated with the track fit χ^2 / ndf.

3.2.4.2 Velocity

Velocity is measured by the TOF and the RICH. For the low-energy study, only the TOF is used. To ensure the best possible velocity reconstruction many quality cuts are applied to the TOF. Events must have exactly 4 TOF clusters associated to the track. This ensures that all 4

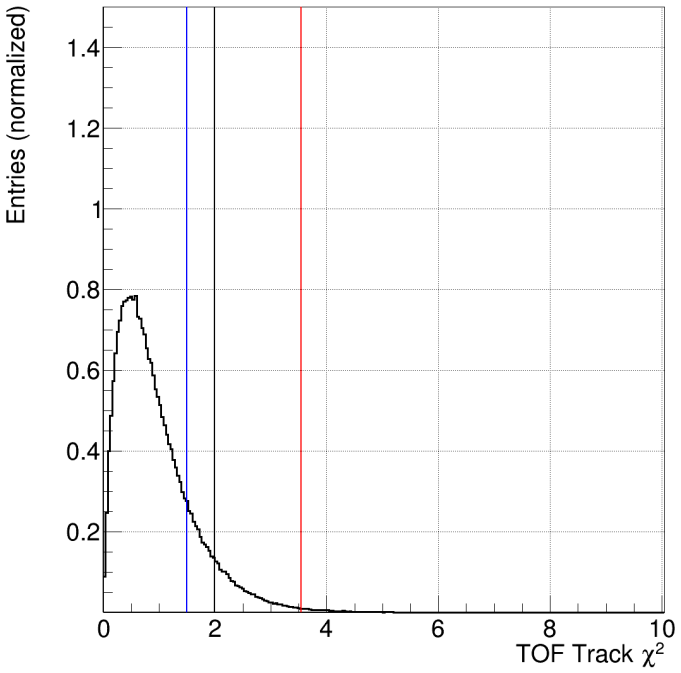

FIGURE 3.11: The BetaH spatial fit χ^2/n.d.f. distribution for B1128 antiproton MC. The black vertical line shows the cut value. The red and blue vertical lines represent the ± 10% efficiency of the cut.

TOF layers are used for the velocity reconstruction. Only one extra TOF cluster is allowed in the event, where an extra cluster is one which fired, but was not associated to the AMS particle.

The TOF velocity is calculated using the BetaH algorithm. The BetaH algorithm works by comparing the tracker track with the TOF clusters used for the velocity measurement. The velocity fit is performed independently for the spatial information as well as the timing information. The χ^2 / degrees of freedom of the spatial fit must be less than 2.0. The variable distribution is given in Fig. 3.11. The χ^2 / degrees of freedom of the timing fit must be less than 8.0. The variable distribution is given in Fig. 3.12.

An additional spatial matching is imposed between the extrapolated tracker track to the TOF clusters to insure that the correct paddle was indeed hit. For a later analysis using energy deposition information, this simplifies the energy deposition per unit length calculation. This spatial matching is called "Tracker Track TOF Hit Matching" in table 3.4.

The TOF spatial hit positions are recorded differently depending on if the position coordinate is parallel or perpendicular to the paddle orientation. Consider a central paddle in the first layer of the TOF. Paddles in the first TOF layer are oriented along the X direction. Therefore, the Y coordinate of a layer 1 TOF hit will be given as the central Y coordinate of that paddle. The X coordinate will be measured from the timing of the 4 PMTs of the paddle. The scintillation

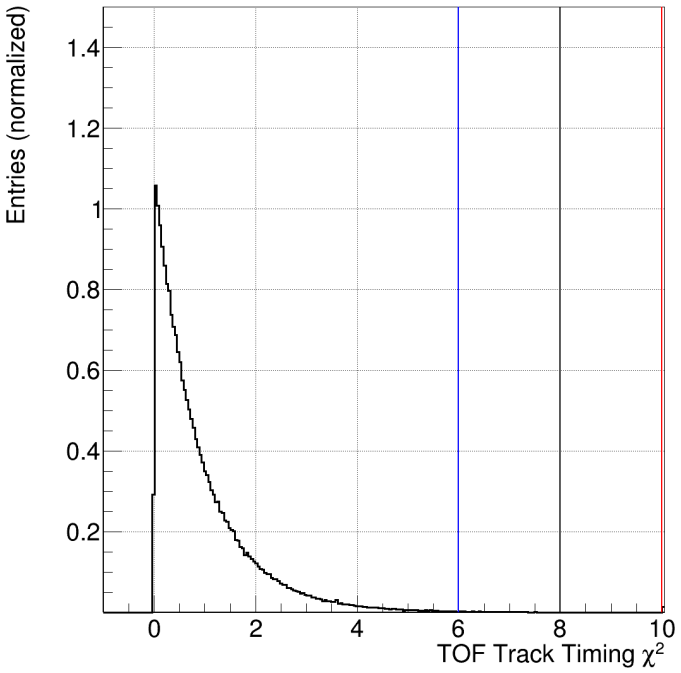

FIGURE 3.12: The BetaH temporal fit χ^2/n.d.f. distribution for B1128 antiproton MC. The black vertical line shows the cut value. The red and blue vertical lines represent the ± 10% efficiency of the cut.

light will radiate out from the hit position at the speed of light of the paddle material. By measuring the timing between when the two pairs of PMTs record the scintillation signal, an X hit position can be calculated.

The goal of the cut is to insure that the correct paddle was identified for the event. Therefore, it is important to look at the residual between the TOF hit position and the tracker track position at the TOF layer, presented in Figs 3.13, 3.14, 3.15, and 3.16. It is immediately clear which TOF hit coordinate is derived from the PMT timing information as this will be Gaussian in shape. The hit residual from the fixed paddle center appears as two superimposed plateaus. The wider plateau corresponds to edge paddles, which are wider than the central paddles.

The cut positions are presented as vertical lines, where the edge paddles have the wider cut to account for their greater width compared with the central paddles. Central paddles have a width of 12 cm. The residual should therefore be -6 cm to 6 cm, which is where the cut is placed. The edge paddles have different widths for different layers. The cut for the edge paddles of layer 1 and 2 are set at -12.75 cm to 12.75 cm. The cut for the edge paddles of layer 3 is set at -11.5 cm to 11.5 cm. The cut for the edge paddles of layer 4 are set at -14.5 cm to 14.5 cm. The residual distribution from PMT timing for layers 1, 3, and 4 were found to be very similar.

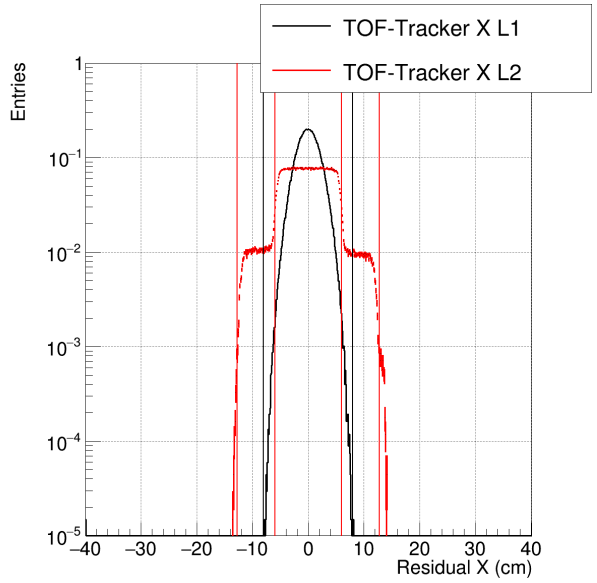

FIGURE 3.13: TOF hit position minus tracker hit positon for B1128 antiproton MC. X hit residuals for the UTOF.

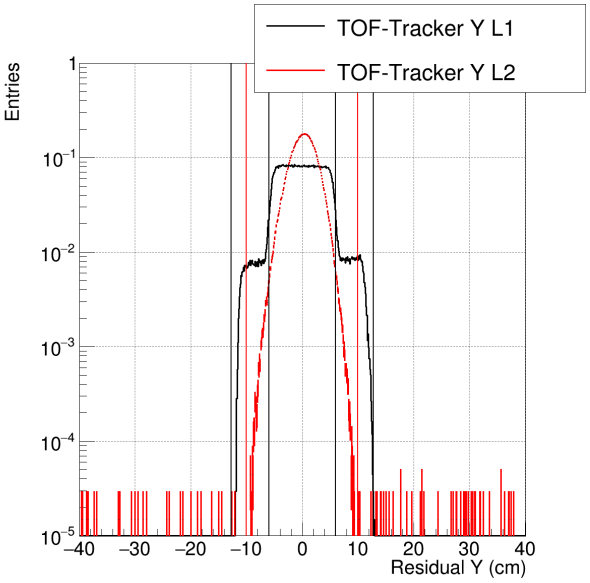

FIGURE 3.14: TOF hit position minus tracker hit positon for B1128 antiproton MC. Y hit residuals for the UTOF.

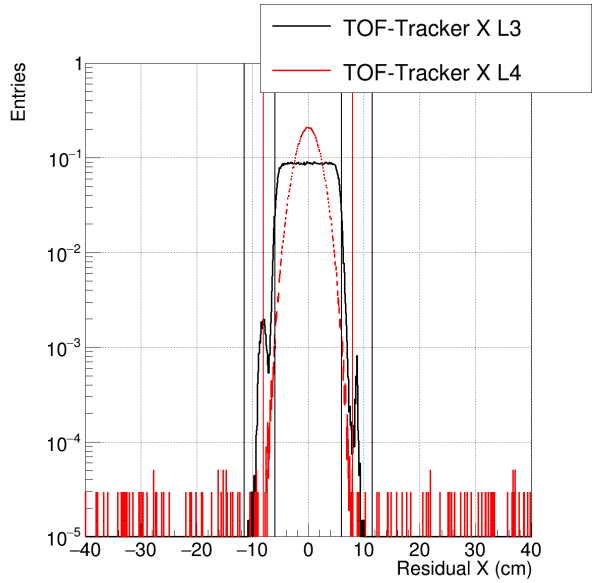

FIGURE 3.15: TOF hit position minus tracker hit position for B1128 antiproton MC. X hit residuals for the LTOF.

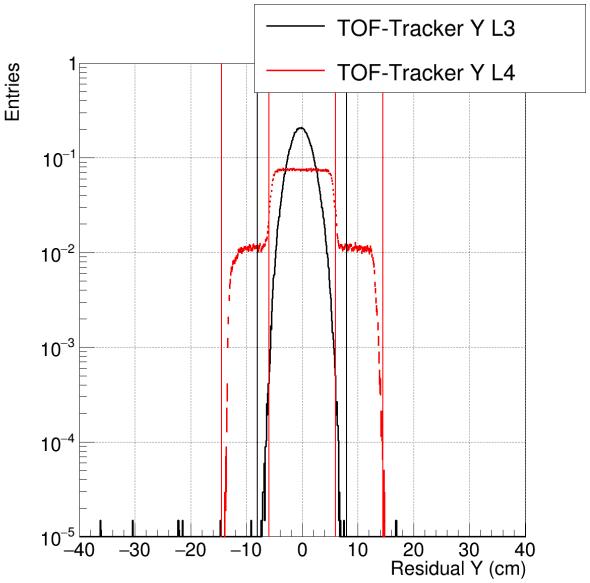

FIGURE 3.16: TOF hit position minus tracker hit position for B1128 antiproton MC. Y hit residuals for the LTOF.

The cut was placed at -8 cm to 8 cm for these layers. The residual distribution for layer 2 was found to be slightly wider, and the cut is thus set to -10 cm to 10 cm for this layer.

The detector volume is fiducialized to exclude the edges of the detector medium. If considering the detector in cylindrical coordinates, the radial value of the tracker track is cut on at two Z positions. At the RICH radiator, Z = -73.6 cm, a radius $<$ 80.0 cm is cut on. At tracker layer 5-6, Z = 0.0 cm, a radius of $<$ 47.0 cm is cut on. The Z = 0.0 cm cut was recommended by S. Haino [54] from a study which found a large fraction of charge confused events concentrated at the tracker edge. Both fiducial cuts are taken "as is" by the author and not investigated further. The zenith angle of the incoming particle is restricted to $< 45°$ at tracker layer 2, Z = 53.06 cm. The zenith angle is restricted to $< 45°$ at the RICH radiator, Z = -73.90 cm.

The RICH has a minimum velocity threshold of $\beta = 0.76$ for the NaF radiator. TOF events are defined such that below the NaF threshold no RICH ring can be present and above the NaF threshold a ring may be present. It was found from Monte Carlo that events which have a large number of RICH hits but no RICH ring can fake an antiparticle signal. In order to limit this behavior for the antiparticle flux analysis a maximum of 7 random RICH hits are allowed in a TOF event.

The main tracker volume is surrounded by the ACC. It is important to exclude events which have a simultaneous crossing event. Only a single particle should cross AMS-02 from top to bottom. If a particle enters the tracking volume from the side, it can potentially produce hits which can fool the tracking algorithm depending on the hit positions. In order to exclude these tracker crossing events from the sides of AMS-02 no more than 1 ACC hit may be present for an event to be accepted.

3.2.4.3 Background Suppression

Background rejection is very important as mentioned in 3.1. The TRD can be used to reject electrons and to a lesser extent low mass mesons from antiprotons and antideuterons. In order to use the TRD accurately it must be assured that the independent TRD track corresponds to the particle tracker track. The matching is accomplished by comparing the zenith and azimuth angles of the TRD track and tracker track at the UTOF, Z = 63.65 cm. A few months of ISS data were analyzed with all cuts applied except the TRD tracker matching cuts. The reconstructed TOF velocity was restricted to 0.60c-0.76c. This provided a clean mostly proton sample. The resulting residuals (TRD - tracker) between TRD and tracker zenith and azimuth were plotted. The distributions, Fig. 3.17, were fit to a Gaussian and the cut was set at 3σ.

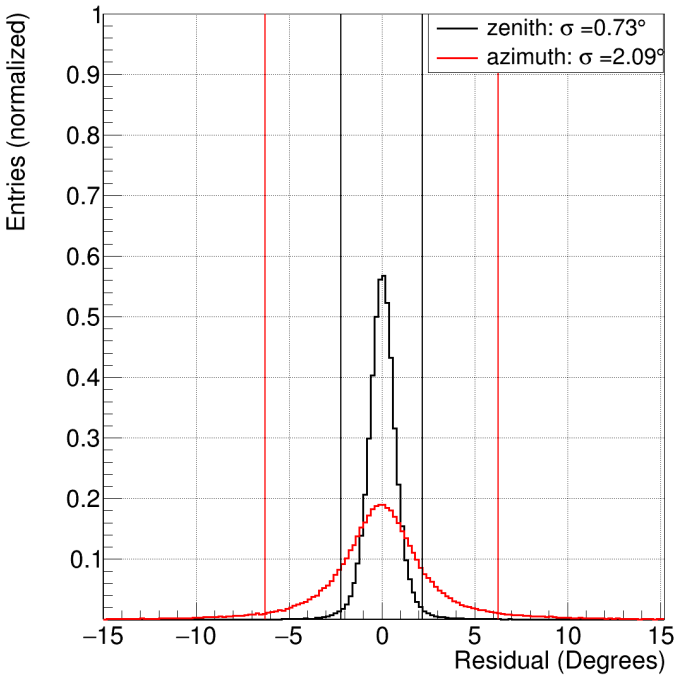

FIGURE 3.17: TRD angle minus tracker track angle at the UTOF for several months of ISS data.

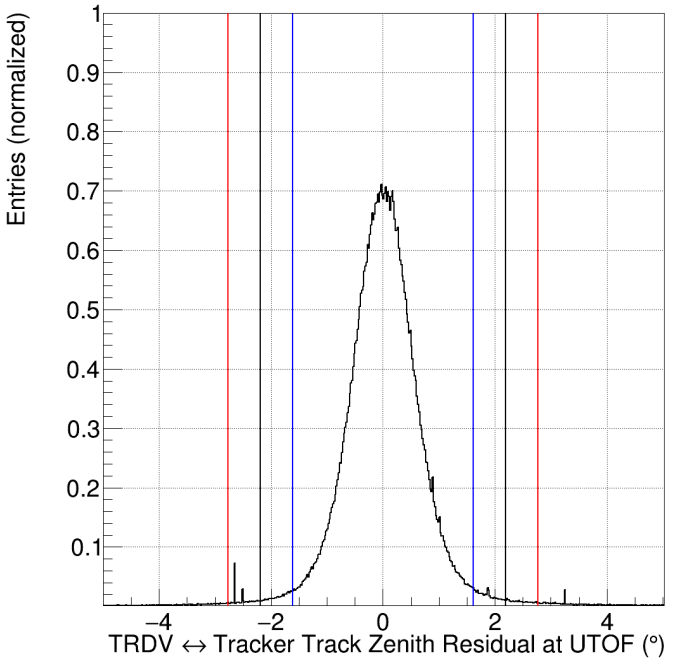

FIGURE 3.18: The TRD minus tracker track zenith angle residual for B1128 antiproton MC. The vertical black lines identify the cut position. The vertical red and blue lines bound the resolution around the cut position.

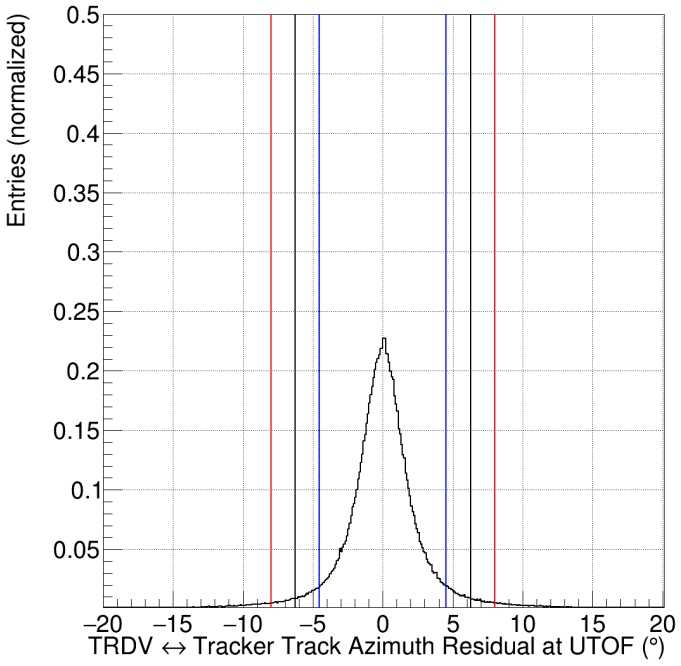

FIGURE 3.19: The TRD minus tracker track azimuth angle residual for B1128 antiproton MC. The vertical black lines identify the cut position. The vertical red and blue lines bound the resolution around the cut position.

The procedure was repeated on antiproton Monte Carlo, Figs. 3.18 and 3.19, and the results were found to be comparable to the proton data. To be cautious the data derived cut is used. The residual is restricted to be less than $|2.19°|$ for zenith and less than $|6.27°|$ for azimuth.

The large acceptance of the TRD can be problematic at high magnetic latitudes and in the SAA as many coincident particles may enter the TRD due to the very high particle fluxes in those locations. There must be found a way to allow coincident tracks in the TRD as long as they are clearly separate from the tracked AMS-02 particle. The "Clean TRD" cut attempts to ensure clean TRD tracks while maintaining a uniform cut efficiency over all geographic positions. A TRD segment is a linear fit of hit TRD tubes in either the XZ or YZ plane. The TRD is composed of 4 tubes oriented in the X plane, 12 tubes oriented in the Y plane, and 4 more tubes oriented in the X plane. A segment may be located in any of the three sections. Thus, if only a single particle crosses the TRD from top to bottom, 3 segments can be reconstructed. TRD hits may or may not be associated to a given segment. If a TRD hit is used to construct a segment, it is tallied as an associated hit. If a TRD hit is not used to construct a segment it is classified as unassociated. There should thus be a correlation between hits generated by real particles traversing the TRD and the total segment count. However, for statistical reasons a hit may be missed when a segment is reconstructed. Therefore one must allow

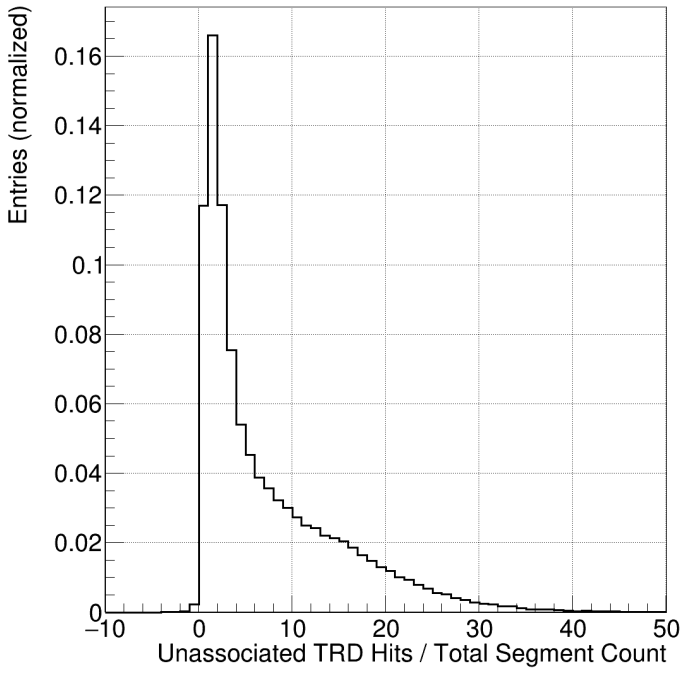

FIGURE 3.20: The TRD Clean cut variable distribution. Negative values are due to TRD hits associated with more than one TRD segment.

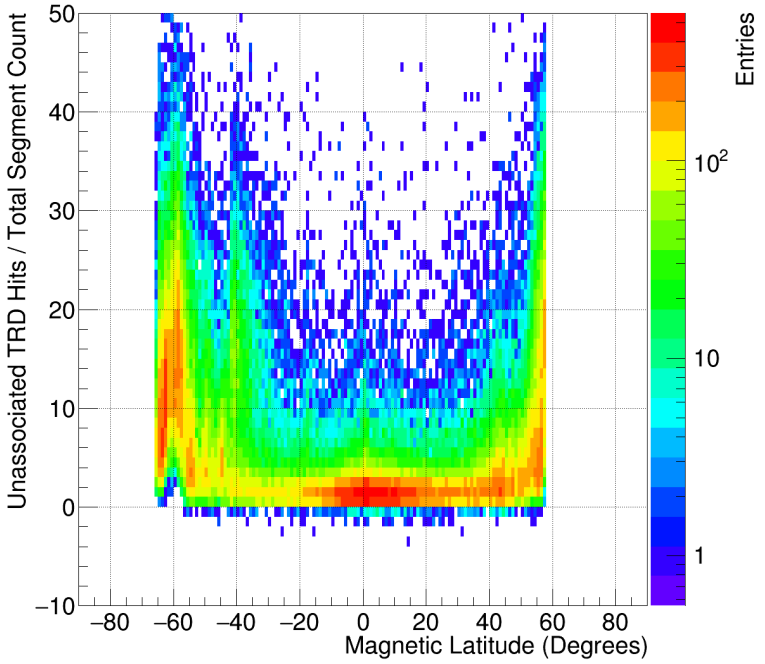

FIGURE 3.21: The TRD Clean variable plotted with respect to magnetic latitude. It can be seen that near the magnetic poles the variable becomes larger. The cause is coincident tracks, which are more common near the poles due to the high particle flux.

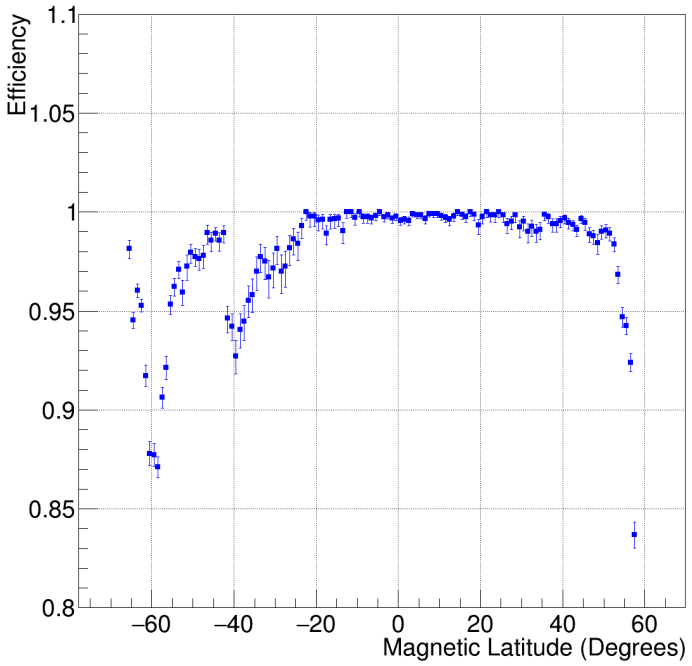

FIGURE 3.22: The TRD Clean cut efficiency with respect to magnetic latitude. The asymmetry between positive and negative magnetic latitude is due to the SAA, which is the feature at -40 degrees magnetic latitude.

a certain number of unassociated hits and this number should be proportional to the total segment count. In this way one does not restrict the total number of TRD hits but instead restricts the number of unassociated hits compared to the total segment count.

A few months of ISS data were analyzed with all other quality cuts applied except for the TRD clean cut. The resulting mostly proton sample was then restricted to reconstructed TOF velocity 0.60c-0.76c. Fig. 3.20 shows the variable distribution of unassociated TRD hits divided by the total TRD segment count. Fig. 3.21 shows the same information plotted with respect to magnetic latitude. It is clearly seen that there is an increase in the variable value as the ISS approaches the magnetic poles. As a compromise between overall efficiency and uniform efficiency with respect to location, a cut value of < 25 was chosen. The resulting cut efficiency with respect to magnetic latitude is presented in Fig. 3.22.

The TRD was designed to reject protons from positrons at a level of better than 10^{-3} in the energy range of 3 - 100 GeV with an efficiency of 90%. This rejection power may also be used to discriminate antiprotons from electrons. A TRD likelihood method was developed by AMS-02 collaboration members for this purpose. A minimum of 10 tubes, half of the TRD, must be used to construct the likelihood. Events with electron-proton TRD log likelihood ≥ 0.4 are

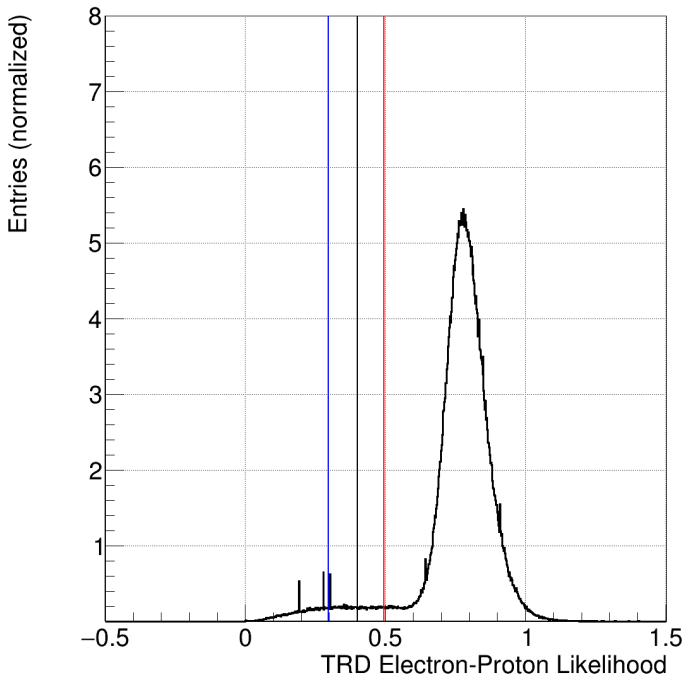

FIGURE 3.23: The electron-proton log likelihood distribution for B1128 antiprotons. Events are selected if their likelihood value is greater than or equal to 0.4. The black vertical line shows the cut value. The red and blue vertical lines represent the ± 10% efficiency of the cut.

accepted. From Fig. 3.23 it can be seen that the cut value is not very restrictive because the bulk of events are not excluded.

High energy cosmic rays can impact the support structure of the TRD and undergo hard interactions. This is a sinister scenario because a proton may produce for instance, antiprotons or more protons. For certain geometries, the protons can escape AMS-02 without impacting the TOF or ACC, and a lone antiproton may enter the tracker volume. This is a real antiproton and may have an exceptionally clean track in the tracker. An event display for such a signature is shown in Fig. 3.24.

TRD segments are compared two at a time and, if they are found to cross in the TRD, a TRD segment crossing is defined by the Z position of the crossing and if it is an X or Y segment. In theory a true interaction vertex should have two or more TRD segment crossings, at least one XZ and YZ pair. If an XZ and a YZ segment crossing are within 5 cm in Z, a TRD vertex is assumed to have been found. 5 cm vertical matching was chosen because this is roughly 2 fleece and tube layers and should be well within the resolution of the TRD segment reconstruction uncertainty. If a single vertex is found, regardless of if it matches the tracker track or not, the event is rejected. Fig. 3.25 shows the reconstructed mass distribution of events before and after the TRD vertex cut is applied. Also presented is the reconstructed mass distribution of the

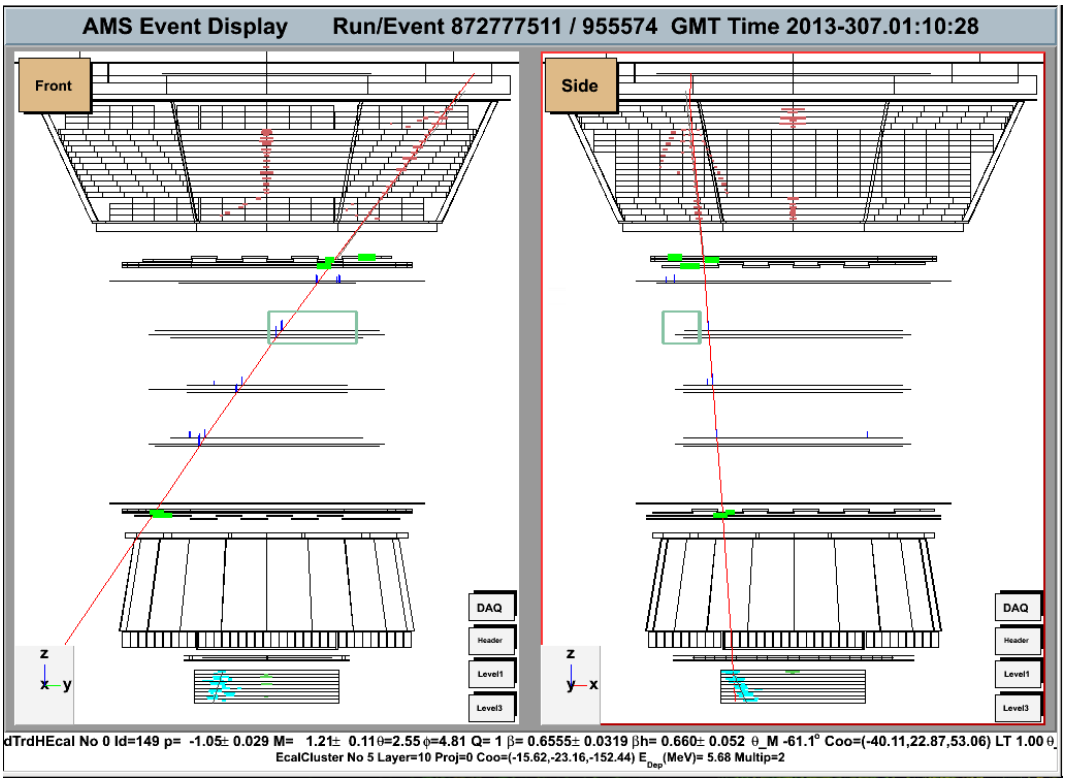

FIGURE 3.24: Event display of a Monte Carlo 572 GeV/c proton generating a secondary antiproton in the TRD.

rejected events. It is observed that several vertex events are removed by this cut which have an antiproton like reconstructed mass. The trend towards low mass removed events may be due to kaons being removed, which should make up a fraction of vertex events due to the short kaon lifetime.

A substantial amount of low-energy charged pions and kaons are produce near the top of AMS-02 and in structures of the ISS. In order to remove these events a method has been developed using energy deposition and rigidity.

For a given charge and rigidity, the energy deposition per unit length, $\mathrm{d}E/\mathrm{d}x$, will be higher for heavier particles. This difference can be used to distinguish particles of differing mass. It is convenient to normalize raw energy depositions to the energy deposition of a minimally ionizing particle, MIP. Protons with a velocity of about $\beta = 0.9$, or a momentum of about 3 GeV/c, will be minimally ionizing in most materials. The MIP normalization is obtained from Monte Carlo for B1128 antiprotons as follows.

Good events are selected by passing the quality cuts. No distinction is made between TOF, NaF, or aerogel events. To be sure that minimally ionizing particles are chosen, the events are sampled from the generated momentum range 3.0 to 4.0 GeV/c. The reconstructed tracker track is extrapolated to the central Z position of each TOF plane and the zenith angle is found.

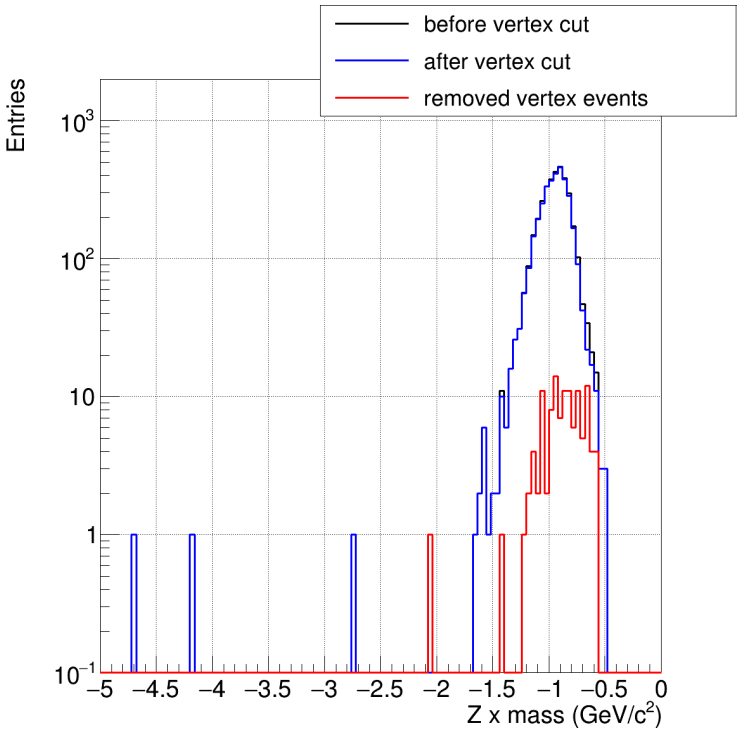

FIGURE 3.25: The reconstructed mass distribution for negative rigidity particle before and after the TRD vertex cut. Also shown is the mass distribution of the removed vertex events.

The energy deposition recorded on that plane is multiplied by the cosine of the zenith angle in order to account for the path length of material traversed. The peak is then found and used as the MIP normalization for that TOF layer.

Although there are only 4 TOF layers, a truncated mean $\mathrm{d}E/\mathrm{d}x$ is calculated. This is done by taking the average of the two lowest $\mathrm{d}E/\mathrm{d}x$ values.

This cut was initially developed using the B1068 antiproton Monte Carlo. The methodology will thus be described to explain why the particular cut line was chosen. This cut has since been validated for B1128 antiproton Monte Carlo, but the removed percent of events is not the same as for B1068 because of the differing amounts of low mass secondaries contained in the two Monte Carlo versions. The percentage removed necessarily depends on the amount of pions produced in the MC, which can vary between production versions. The important consideration should be the removal of distinct populations.

The B1068 antiproton Monte Carlo was analyzed with all the preselection cuts, with the exception of the TOF Truncated Mean Cut. The selection cut was determined per rigidity bin to exclude 11 % of events below the cut value, keeping the remaining 89%. When applied to data, pions and kaons sit below the cut and are excluded.

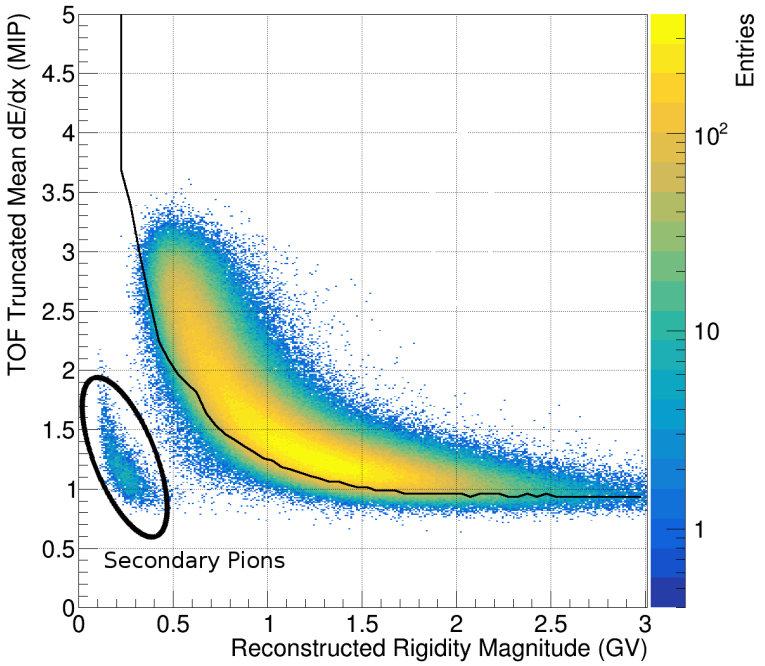

FIGURE 3.26: B1128 antiproton Monte Carlo TOF $\mathrm{d}E/\mathrm{d}x$ information as a function of reconstructed rigidity. All quality cuts have been applied except for the TRD vertex cut, the TRD active layers cut, and the TRD electron-proton likelihood cut. The black curve shows the "Pion $\mathrm{d}E/\mathrm{d}x$" cut. The ellipse highlights the population of secondary pions. Due to kinematic reasons, pions are produced in greater abundance than kaons and are thus more visible. Due to their higher mass, the kaon population will be nearer to the antiproton population.

The cut value remains effective for B1128 antiproton Monte Carlo. Fig. 3.26 demonstrates how the cut removes the distinct pion population while keeping the majority of antiprotons. The plot was constructed by omitting the TRD vertex cut, the TRD active layers cut, and the TRD electron-proton likelihood cut in order to show a clear population of secondaries.

The quality cuts may be grouped into similar categories. It is helpful to then observe the reconstructed mass of data events as successive groups of similar cuts are applied. Fig. 3.27 shows the cut progression for ISS data recorded between May2011-May2017 for negatively charged down-going particles. Of the 1.37 billion events which passed the minimum cuts, 3429 events survive all the quality cuts in the TOF velocity range $0.50c$-$0.80c$.

3.2.5 Trigger Efficiency

The trigger efficiency of AMS-02 is estimated directly from flight data. It is assumed that the proton and antiproton trigger efficiency is equivalent. The AMS-02 fast physics trigger logic requires the 4 TOF planes to have a coincidence signal. These are the so called physics trigger events, N_{phys}. An unbiased sample of events is selected by using a reduced trigger logic.

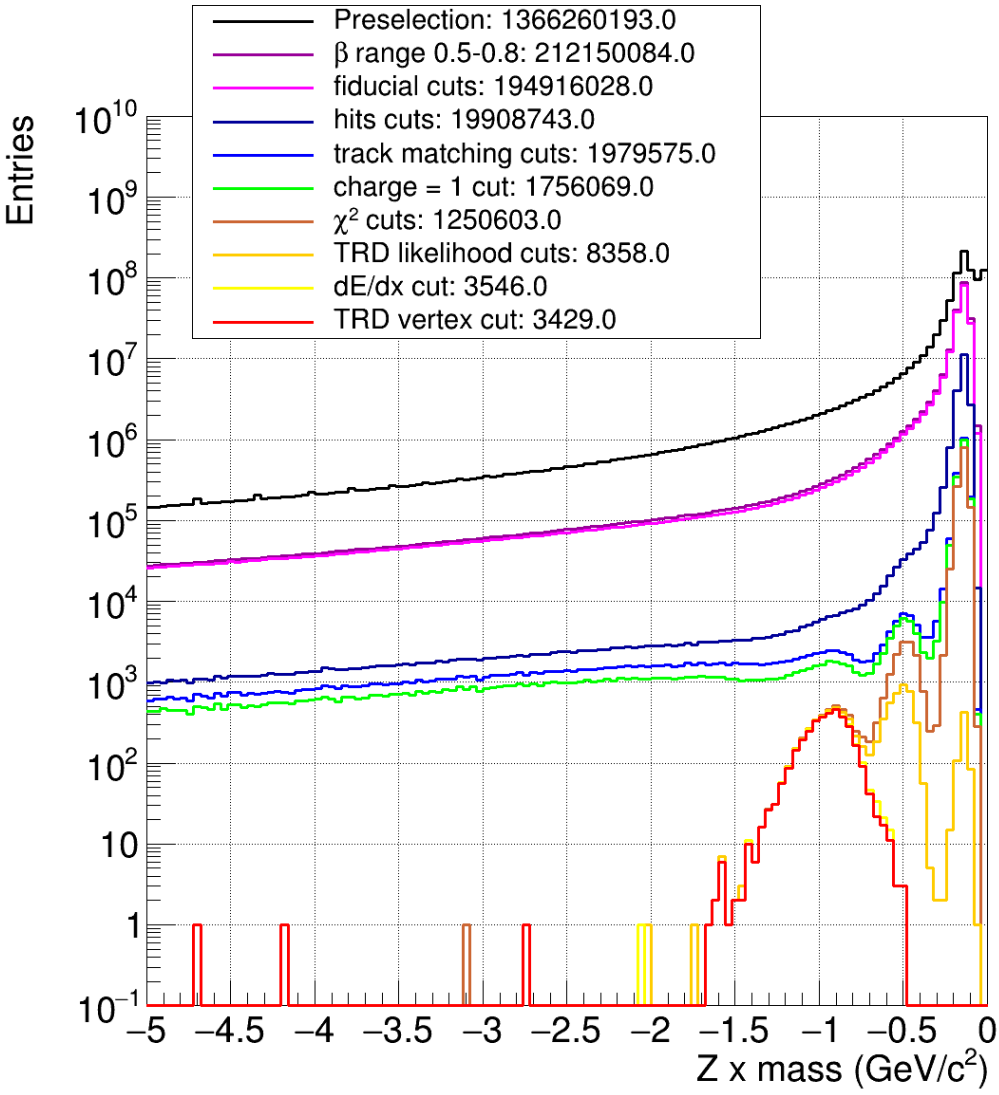

FIGURE 3.27: ISS data B950 Pass6 May2011-May2017. This plot begins with the minimum cuts and shows the cut progression with corresponding statistics. No restriction on geomagnetic cutoff is applied.

There are three classes of unbiased triggers, TOF, ECAL, and hybrid (flagged as both TOF and ECAL). Unbiased TOF and hybrid events trigger on 3 of the 4 TOF planes. Only 1/100 of TOF or hybrid unbiased triggers, N_{unbTOF} or $N_{unbHybrid}$, are kept in order to reduce data size. Only 1/1000 ECAL unbiased triggers, $N_{unbECAL}$, are kept. Eq. 3.7 shows how the trigger efficiency is calculated. Since the majority of charge 1 events in flight data are protons no charge sign cut is applied. The trigger efficiency is calculated as a function of reconstructed TOF β after all quality cuts have been applied. Due to the very large size of the full AMS-02 dataset a subset of ISS data is used which evenly samples the analysis time period.

$$\epsilon_{trig} = \frac{N_{phys}}{N_{phys} + 100(N_{unbTOF} + N_{unbHybrid}) + 1000N_{unbECAL}} \tag{3.7}$$

The majority of unbiased events are of the unbiased TOF class. It is enough to consider the uncertainty of the trigger efficiency using only the unbiased TOF events, N_{unb}. In order to calculate the uncertainty, let us consider ϵ' as defined by equation 3.8. The uncertainty for ϵ' is obtained from Gaussian error propagation as follows.

$$\epsilon' = \frac{N_{phys}}{N_{phys} + N_{unb}} \tag{3.8}$$

$$\frac{\sigma_{\epsilon'}}{\epsilon'} = \sqrt{\left(\frac{\sigma_{N_{phys}}}{N_{phys}}\right)^2 + \left(\frac{\sigma_{N_{unb}}}{N_{unb}}\right)^2} \tag{3.9}$$

This simplifies to:

$$\frac{\sigma_{\epsilon'}}{\epsilon'} = \sqrt{\frac{N_{phys}N_{unb}^2 + N_{phys}^2 N_{unb}}{(N_{phys} + N_{unb})^4}}. \tag{3.10}$$

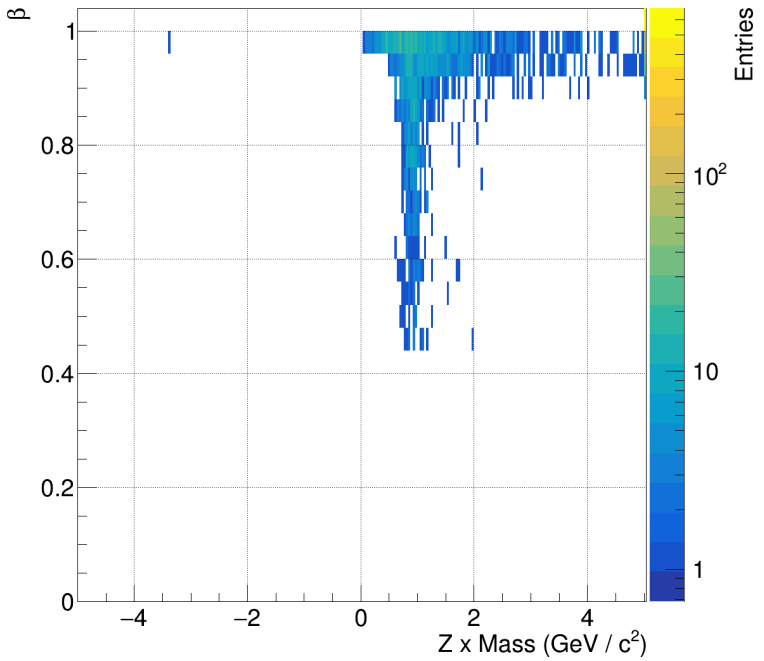

FIGURE 3.28: The distribution of unbiased TOF events for a few months of flight data during the analysis time period. It is evident that the majority of unbiased events are protons.

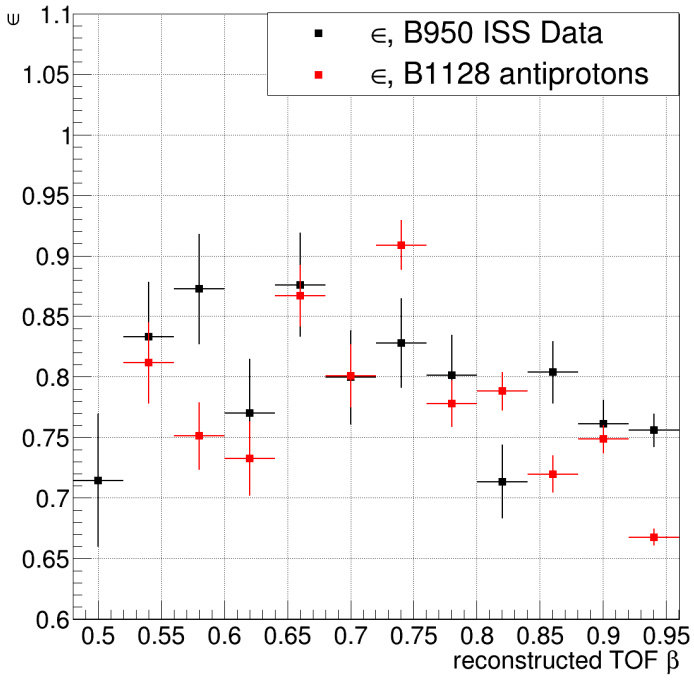

FIGURE 3.29: The measured trigger efficiency for B950 Pass6 ISS data and B1128 antiproton MC is presented. Although there appears to be some discrepancies between data and MC, the agreement is good between β 0.52-0.80, with a $\chi^2/\text{ndf} = 1.28$.

It is useful to solve for N_{phys} in terms of the scaling factor, f, the unbiased counts, and the trigger efficiency.

$$N_{phys} = f N_{unb} \frac{\epsilon_{trg}}{1 - \epsilon_{trg}}. \tag{3.11}$$

Substituting equation 3.11 into 3.8 yields:

$$\epsilon' = \frac{f\epsilon_{trg}}{1 + f(\epsilon_{trg} - 1)}. \tag{3.12}$$

And solving for ϵ_{trg} gives:

$$\epsilon_{trg} = \frac{\epsilon'}{f - (f-1)\epsilon'}. \tag{3.13}$$

Finally, we may solve for $\sigma_{\epsilon_{trg}}$, the uncertainty of the trigger efficiency:

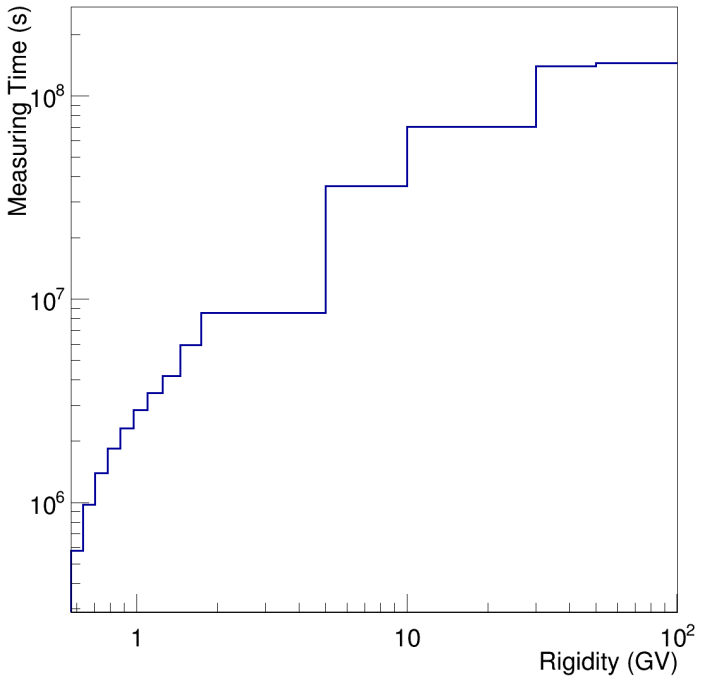

FIGURE 3.30: The measurement time above geomagnetic cutoff. This has been calculated using the Stöermer approximation with a 1.2 safety factor for the full TOF field of view.

$$\frac{\sigma_{\epsilon_{trg}}}{\epsilon_{trg}} = \frac{f}{(f-(f-1)\epsilon')^2}\sigma_{\epsilon'}. \tag{3.14}$$

The trigger efficiency is also calculated for the B1128 antiproton Monte Carlo. It is seen that there is agreement between the flight data trigger efficiency, which is mostly protons, and the trigger efficiency of MC antiprotons. A comparison of MC and data was done for the data points between TOF β 0.52-0.80 and the χ^2/ndf was found to be 1.28. Therefore the data trigger efficiency may be used without the negative rigidity cut applied. Fig. 3.29 shows the trigger efficiency for TOF events for data and antiproton Monte Carlo.

3.2.6 Measurement Time

In order to determine the particle flux, the amount of time the detector was taking data must be known precisely. The AMS-02 detector electronics have an onboard clock which precisely monitors the time that the detector is active. In addition, data processing on the ground accounts for any time period during which calibration or other off nominal data taking occurred.

The measurement time for AMS-02 combines detector livetime and flight parameters. For the Galactic antiproton flux analysis it is important to only consider data taking periods when the

detector is in a region where above cutoff cosmic rays may reach the detector. The Stöermer approximation of the geomagnetic rigidity cutoff (Sec. 3.2.3) is used with a 1.2 safety factor for the field of view of the TOF.

Measurement time will in general be a function of rigidity due to the dependence on the geomagnetic cutoff. Measurement time is calculated for top of the detector rigidity. Fig. 3.30 shows the calculated measurement time above cutoff for AMS-02. The ambient measurement time will correspond to the highest bin because it is well above the maximum cutoff value. The ambient measurement time includes detector livetime but excludes all geomagnetic cutoff effects.

3.2.7 Acceptance

The detector acceptance [55] is estimated from Monte Carlo as a function of generated momentum. For the simulation, particles are generated isotropically over a square 3.9 m on each side located 1 m above the top of the detector. The cube face has been made large enough such that it covers the entire field of view of the detector. Due to isotropy of the particle generation, the detector acceptance may be expressed as the number of events which are selected divided by the total number of generated events, times a geometrical factor A_o.

The geometrical factor is found as follows:

$$A_o = \int_\Omega \mathrm{d}\omega \int_S \mathrm{d}\sigma \hat{r} \tag{3.15}$$

where $\mathrm{d}\sigma$ is the element of surface area, S, and $\mathrm{d}\omega$ is the element of solid angle Ω. Expressed in spherical coordinates, this integral may be written as:

$$A_o = \int_\Omega \int_S \cos\theta \mathrm{d}\sigma \mathrm{d}\omega = S \int_\Omega \cos\theta \mathrm{d}\cos\theta \mathrm{d}\phi \tag{3.16}$$

The surface integral integrates to

$$A_o = S \int_0^1 \int_0^{2\pi} \cos\theta \mathrm{d}\cos\theta \mathrm{d}\phi = 2\pi S \int_0^1 \cos\theta \mathrm{d}\cos\theta = \pi S[\mathrm{sr}] \tag{3.17}$$

The geometrical factor A_o has been found to be πS, where S is the surface area of generation. Finally, A_o is found to be 47.78 m^2 sr. The detector acceptance is thus given by 3.18.

$$A(p_{gen}) = 47.78 \frac{N_{pass}}{N_{gen}} [\mathrm{m}^2\mathrm{sr}] \tag{3.18}$$

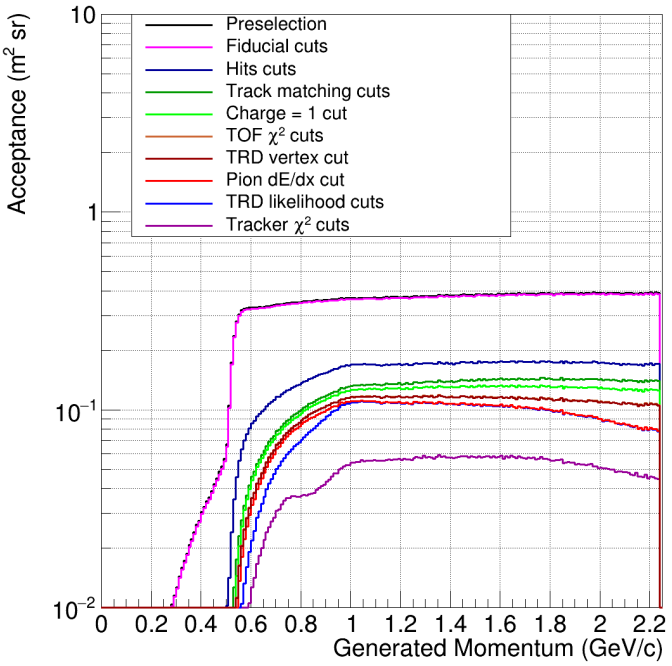

FIGURE 3.31: The Monte Carlo acceptance progression as a function of generated momentum for B1128 antiprotons.

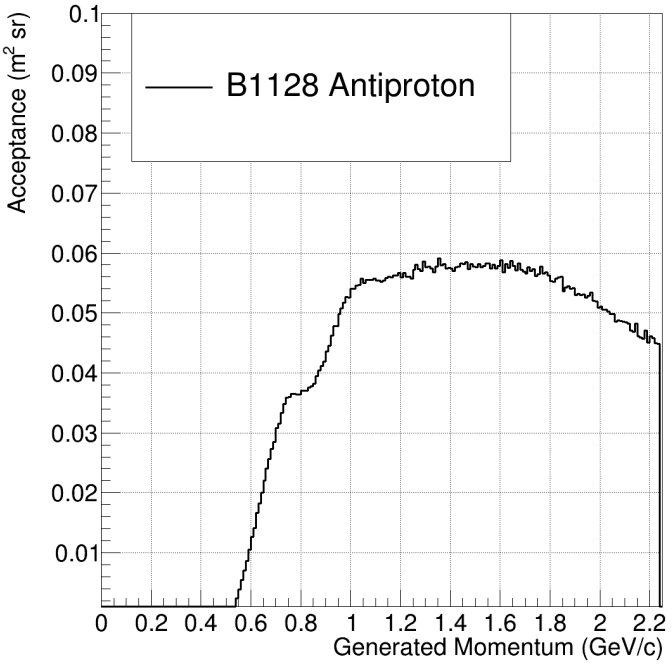

FIGURE 3.32: The Monte Carlo acceptance as a function of generated momentum. This corresponds to the full TOF geometry and accounts for all selection and quality cuts.

It is interesting to look at how the detector acceptance evolves as successive quality cuts are applied, Fig. 3.31. Similar cuts may be grouped together. It can be seen that a few cuts produce interesting features in the acceptance. It should be noted that many cut sequence permutations were analyzed and the presented order was chosen to best illustrate the features. The cut on the tracker χ^2 produces a dip in acceptance at roughly 0.8 GeV/c and has been traced to an overall correction applied to the tracker reconstruction during production. The overall detector acceptance as a function of generated momentum is shown in Fig. 3.32. The MC acceptance is roughly 0.058 m^2 sr for this analysis.

3.2.8 Data/Monte Carlo Cut Correction Factors

The simulations represent the high energy physics interactions with the detector very well. However, there are certain slight mismatches between data and Monte Carlo that should be corrected for. A multiplicative correction factor is constructed by comparing the last cut efficiencies of data and Monte Carlo.

For each quality cut, all other quality cuts are applied. The last cut efficiency is then the number of events passing the cut divided by the number of events before applying the cut. This last cut efficiency is evaluated for both data and simulation. The cut correction factor for the cut, C_i, is then $\epsilon_{data,i}/\epsilon_{MC,i}$. Fig. 3.33 shows the distribution of the C_is for different velocity bins. It is seen that the majority of C_is are nearly equal to 1. The overall cut correction factor, C, is then the multiplication of all the individual cut correction factors:

$$C = \prod_i C_i = \prod_i \frac{\epsilon_{data,i}}{\epsilon_{MC,i}}. \tag{3.19}$$

Certain correction factors are omitted. Cut correction factors are omitted if the behavior of the variable distribution in data is not expected to agree with MC. The ACC correction factor is omitted because the Monte Carlo does not generate particles from the sides, nor many particles simultaneously, nor are the ISS structures simulated which are known pion sources, and therefore is not expected to match the data environment. Another example would be the dE/dx cut for pions. Since pions are typically generated by the high energy proton flux impinging on materials near the AMS-02 detector, the number of secondary particles is underestimated in the MC. In order to ensure that only slight corrections are applied, a cut correction factor is set to 1 if its calculated value is less than 0.9 or greater than 1.1.

The distributions of many cut variables change slightly depending on the generated momentum spectra. This is one indicator if the input spectra for Monte Carlo matches the data spectrum.

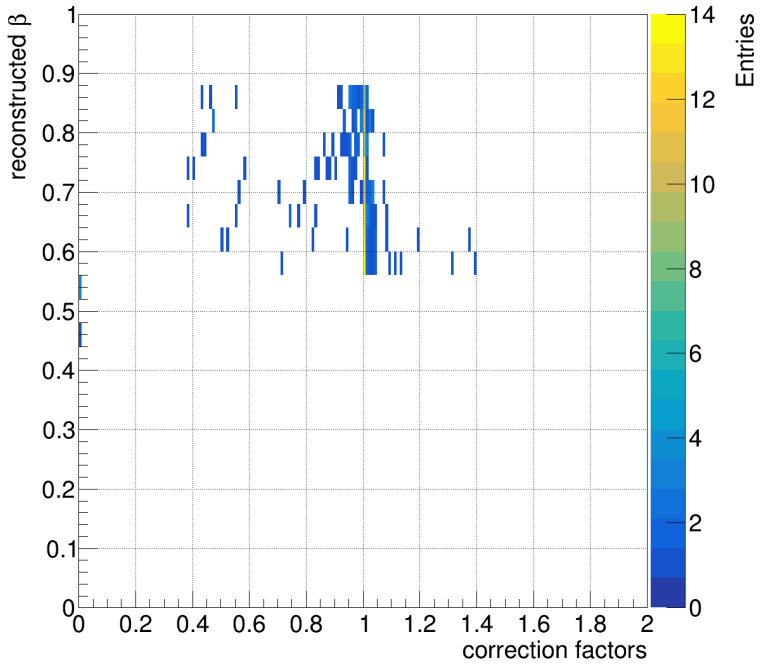

FIGURE 3.33: The individual cut correction factors as a function of reconstructed TOF β. Cut correction factors are excluded if they are less than 0.9 or greater than 1.1. It is seen that the majority of cut correction factors are nearly equal to 1 as indicated by the yellow bins at that value.

Cut corrections factors typically approach 1 as the generation spectrum converges to the true data spectrum.

3.2.9 Energy Loss Correction

The velocity of charged particles are measured by two independent detectors in AMS-02. The TOF measures velocity by precisely measuring the time difference between hits in the upper and lower TOF systems. Higher velocity particles can independently be measured by the RICH, which has a velocity threshold of $0.75c$ for the NaF radiator and $0.95c$ for the silica aerogel radiator. As a particle traverses the detector, energy is deposited in the detector material. For this analysis it is important to consider the energy lost before the particle crosses the UTOF. This analysis aims to measure the energy spectrum of the Galactic radiation as it is in free space, not modulated by the detector itself. The majority of energy loss before a particle reaches the UTOF will be in the passive structure of the TRD. Being passive there is no physical measurement of the energy loss in these structures. One must rely on the simulation to account for this energy loss, where the generated momentum is known for every simulated particle:

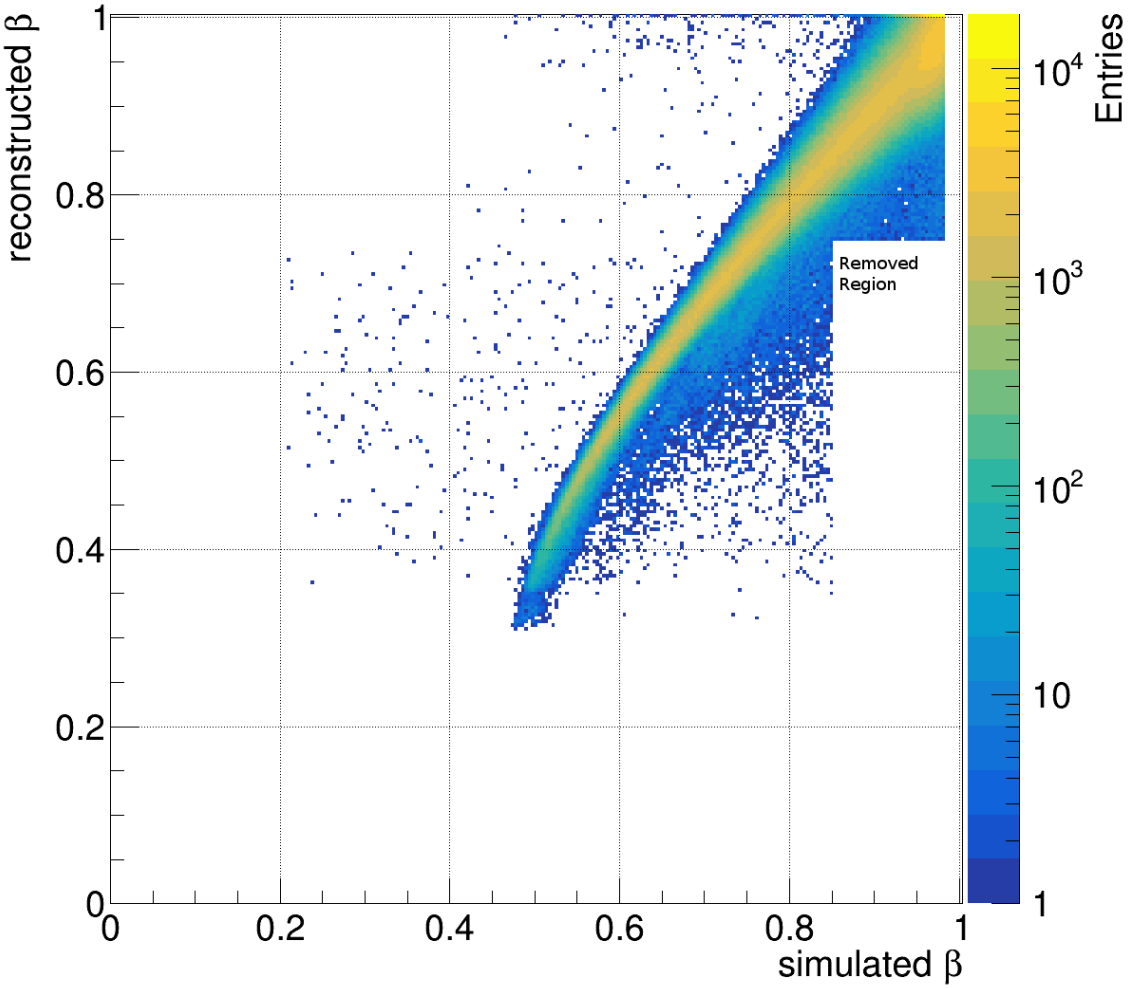

FIGURE 3.34: The velocity map for B1128 antiproton MC events which pass all quality cuts. A region has been manually removed, which is clearly distinct from the region of interest, due to its interference with the peakfinding procedure.

$$\beta_{gen} = \frac{p_{gen}}{\sqrt{m_0^2 + p_{gen}^2}}. \tag{3.20}$$

The mass of the particle is known exactly thus generated velocity can be computed using equation 3.21. It is then useful to plot the distribution of reconstructed velocity as a function of generated velocity for events which pass all quality cuts (Fig. 3.34). In order to properly account for the energy loss, which manifests as a velocity shift, the correction must be applied to a distribution of events. A given bin in reconstructed velocity can be mapped to a true velocity bin by changing the bin edges as well as the bin center. This will modify the bin width in the process.

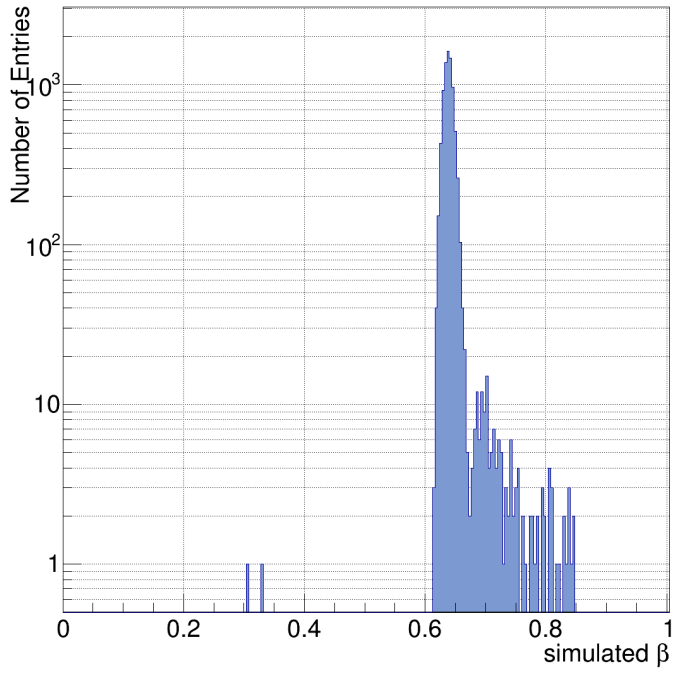

FIGURE 3.35: The reconstructed to true velocity map which contains $\beta = 0.60$. The distribution peaks at $\beta_{true} = 0.64$. Assuming proton mass the true momentum is 0.77 GeV/c.

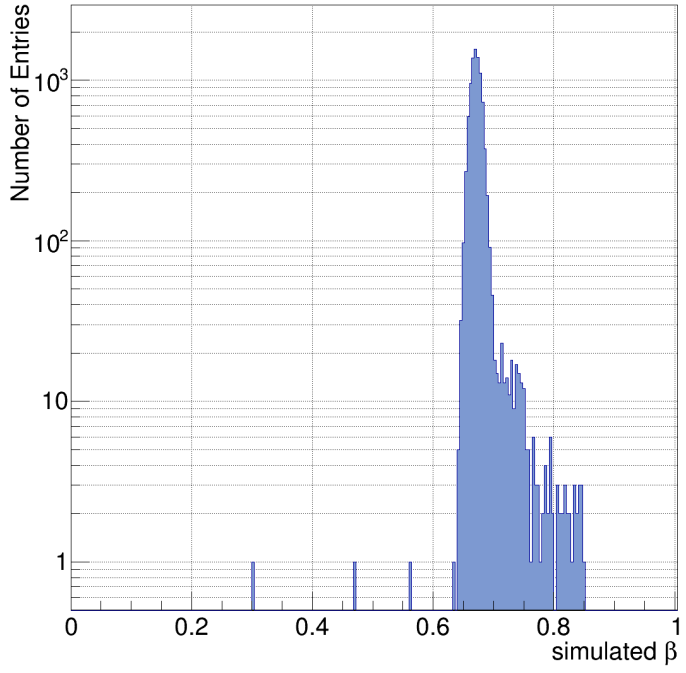

FIGURE 3.36: The reconstructed to true velocity map which contains $\beta = 0.64$. The distribution peaks at $\beta_{true} = 0.67$. Assuming proton mass the true momentum is 0.84 GeV/c.

It is easiest to explain the process by example. Let us consider the reconstructed velocity bin centered at $\beta = 0.62$ with low edge 0.60 and high edge 0.64. Because the velocity map has such fine binning, it is possible to look up the reconstructed to true velocity map nearest to the reconstructed velocity bin value in question. Figs. 3.35 and 3.36 correspond to the low edge and high edge bin map, respectively. The most likely true velocity is the velocity of the peak of the distribution. It is found that 0.60 maps to 0.64 and 0.64 maps to 0.67. The true velocity bin is now defined.

The velocity shift procedure is done for all bins used in the Galactic antiproton flux. Since the energy deposition is proportional to β^{-2} there is a greater effect on the lower velocity bins. Once all the velocity bins are defined, it is then simple to convert these into top of the detector momentum bins using:

$$p = \frac{m_0 \beta}{\sqrt{1-\beta^2}} \tag{3.21}$$

3.2.10 Unfolding

Unfolding is the technique of accounting for bin-to-bin migration of events due to detector resolution. The bin-to-bin migration is in reference to the function independent variable, TOF velocity in the case of this analysis. The detector has a finite velocity resolution which causes leakage of events from a particular velocity bin to neighboring bins. For this analysis a folded acceptance technique is used [56] to account for the bin-to-bin migration. If one assumes that the detector simulation accurately reflects the true detector, then it can be used to estimate the bin-to-bin migration.

For the first iteration, the Monte Carlo is used as is and a flux is produced. The flux is then normalized to area 1. The normalization to 1 is not needed for the procedure, but it makes reweighting the MC easier by having a consistent normalization. A smooth function of the form $y = Ax^b$ is fit to the resulting normalized flux because large variations tend to be amplified with this iterative procedure. It should be noted that using a smooth curve does not wash out these variations. A single power law fit is performed to the initial energy shifted flux to provide a smooth curve. The fit is restricted to the momentum range 0.90-2.00 GeV/c. This range is chosen because it is known a priori that above 2 GeV/c the Galactic antiproton flux does not behave as a single power law. The low range is selected because the energy shifted lowest bin is typically not used due to potential instabilities of the fit.

The MC is reweighted by this fit function and a new flux is calculated, causing the variable distributions to change slightly. This will affect the cut correction factors as a function of β_{rec}.

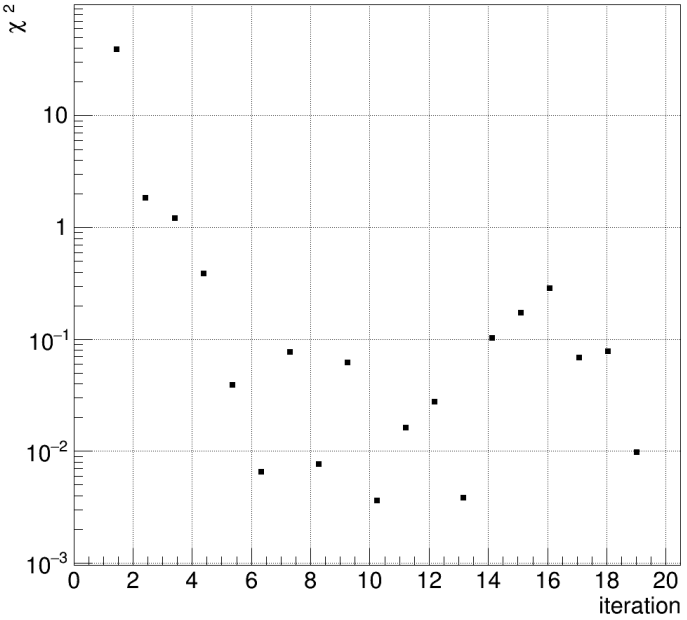

FIGURE 3.37: A χ^2/dof comparison is performed for the i^{th} flux to the i^{th}-1 flux. The procedure is stopped once the χ^2/dof is less than or equal to 1, which occurs at iteration 5 as shown.

In this way, the calculated flux will change. As the iterative procedure progresses, the changes between each iteration will become smaller and eventually reach an oscillatory solution. The i^{th} flux is compared to the i^{th} - 1 flux and a χ^2/dof (degrees of freedom) is calculated. The procedure is repeated until the χ^2/dof is less than 1.0. The iterative procedure was allowed to continue for twenty iteration to produce Fig. 3.37. It can be seen that an oscillation sets in from $i = 5$ as the unfolding procedure continues.

3.2.11 Systematic Uncertainties

There are four main sources of systematic uncertainty which are considered in this analysis. The uncertainty of the nuclear cross section is the dominant systematic. Next is the uncertainty attributable to the selection cuts. A third uncertainty considered is due to the uncertainty of the geomagnetic cutoff. The last uncertainty considered is due to the unfolding procedure.

The cross section uncertainty is estimated by varying the total inelastic cross sections in the simulation and recalculating the measured flux. The structure of AMS-02 is mostly carbon fiber composite and aluminum. Figs. 3.38 and 3.39 present the nuclear cross sections for antiprotons on carbon and aluminum respectively. The cross section models used in the Geant4 simulation are overlayed.

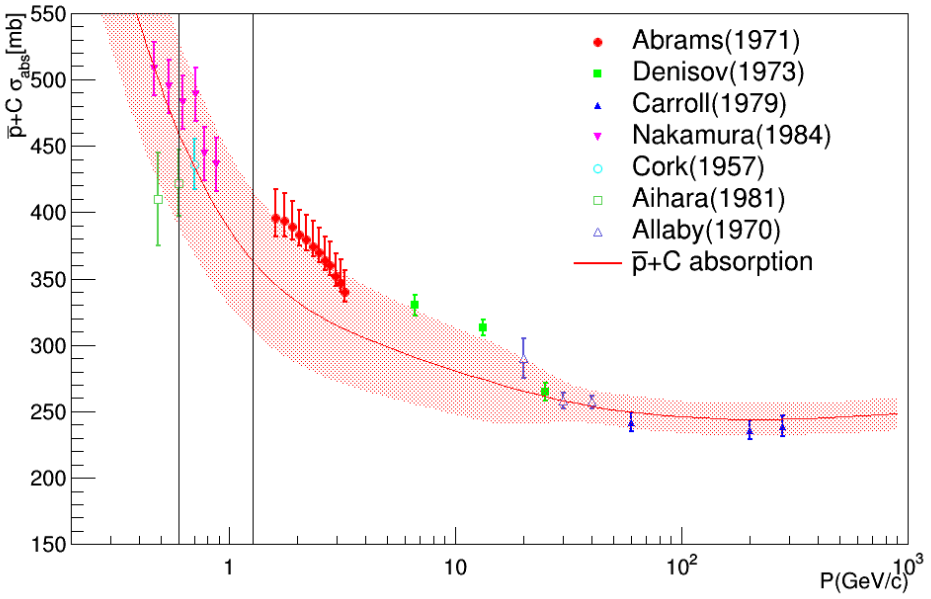

FIGURE 3.38: The nuclear cross sections for antiprotons on carbon as measured by various experiments. The cross section models used by Geant are overlayed. The maximum deviation of the absorption cross section is 11.8% in the true momentum range corresponding the reconstructed TOF velocity range 0.50c-0.80c.

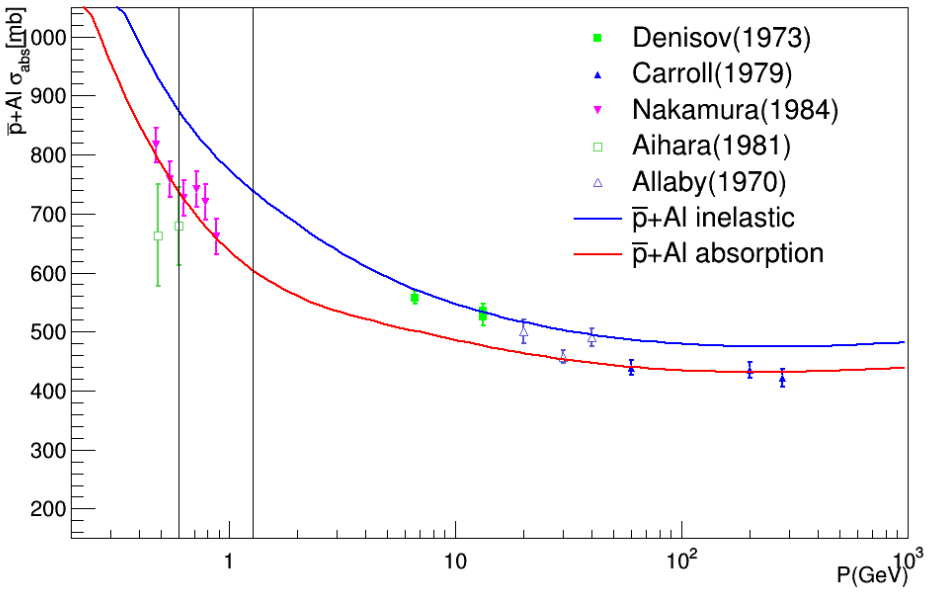

FIGURE 3.39: The nuclear cross sections for antiprotons on aluminum as measured by various experiments. The cross section models used by Geant are overlayed. The maximum deviation of the absorption cross section is 8.8% in the true momentum range corresponding the reconstructed TOF velocity range 0.50c-0.80c.

It is useful to examine the deviation of the cross section model from experimental data in the true momentum range corresponding to the reconstructed velocity range $0.50c$ to $0.80c$. The true momentum range of interest is delineated by the vertical lines. The maximal deviation of the model from data in the momentum range of interest for antiprotons on carbon is 11.8%. The maximal deviation of the model from data in the momentum range of interest for antiprotons on aluminum is 8.8%. The way the simulation handles the inelastic cross section is as a total inelastic cross section for all materials. As such it was decided to vary the total inelastic cross section $\pm$ 10%.

The Galactic antiproton flux was then computed with increased and decreased interaction cross sections. The individual flux data points were then compared to the unvaried cross section result. The maximum deviation from the unvaried cross section flux was then used for the uncertainty value due to the inelastic cross section uncertainty. It was found that this uncertainty is roughly 30% for the region of interest.

How much a single cut should be varied is a semi arbitrary choice. The method used here was chosen to give some meaning. If a quality cut variable has a measured resolution, the cut value will be varied within that resolution range. An example of a cut variable of this type is tracker charge. The tracker charge resolution is measured to be 0.05 for charge 1. The tracker charge cut is greater than 0.70 and less than 1.30. The lower cut is varied between 0.65 and 0.75 while the upper charge cut is varied between 1.25 and 1.35. If a quality cut variable does not have a well defined resolution, the cut variable last cut efficiency is varied $\pm$ 10% for Monte Carlo and the same range is applied to data. An example of this type of variable is the tracker normalized χ^2 cuts. If the quality cut has high efficiency such that $\pm$ 10% is not achievable, the cut is varied by -10% efficiency. Quality cut variables with integer values are varied $\pm$ 1 when possible. Cuts which have a known data specific behavior or are for secondary particle suppression are not varied. These cuts are the ACC hits cut, the TRD clean cut, the TRD vertex cut, and the $\mathrm{d}E/\mathrm{d}x$ pion cut. Fiducial cuts are not varied because such changes would affect the measurement conditions in ways which are inconsistent with a selection bias. The number of TOF clusters associated with the tracked particle is not varied because exactly 4 hits are required by the physics trigger condition. Table 3.5 shows how much each cut is varied.

The uncertainty attributed to the quality cuts is calculated by simultaneously and randomly varying the quality cuts and then unfolding the flux. This is done 1000 times and all the unfolded fluxes are filled in a histogram. For a single flux bin the resulting distribution of fluxes is approximately Gaussian (Figs 3.40 and 3.41). A fit is performed to this distribution and the standard deviation, σ_{total}, is the combined selection cut uncertainty and statistical uncertainty. The event statistics are known for each flux in each flux bin distribution. Also known is the deviation of the counts. The average event count, N, is used to calculate the

TABLE 3.5: Cut groups and variation ranges for the estimation of systematic uncertainty due to the selection cuts.

Cut		Primary Cut	Low	High		Primary Cut	Low	High	Variation Group
Tracker Track Zenith Angle at L2					$\leq$	45°			Unvaried
Tracker Track Zenith Angle at RICH Radiator					$\leq$	45°			Unvaried
Tracker Track Radius at Z = 0					$<$	47.0 cm			Unvaried
Extrapolated Tracker Track RICH crossing radius					$<$	80.0 cm			Unvaried
TOF Clusters Associated with AMSParticle	$=$	4							Unvaried
TOF Clusters NOT Associated with AMSParticle					$\leq$	1	0	2	Integer
ACC Hits					$\leq$	1			Unvaried
Inner Tracker XY Hits	$\geq$	5	4	6					Integer
RICH Hits					$\leq$	7	6	8	Integer
Tracker Track TOF Hit Matching									Unvaried
TRD Vtrack Tracker Track azimuth					$<$	6.27°	4.54°	8.00°	Resolution
TRD Vtrack Tracker Track zenith					$<$	2.19°	1.61°	2.77°	Resolution
Total UTOF Energy Deposition	$>$	3.0 MeV							Unvaried
Total LTOF Energy Deposition	$>$	3.0 MeV							Unvaried
Tracker Charge	$>$	0.70	0.65	0.75	$<$	1.30	1.25	1.35	Resolution
Overall TOF Charge	$>$	0.70	0.65	0.75	$<$	1.30	1.25	1.35	Resolution
UTOF Charge	$>$	0.70	0.64	0.77	$<$	1.30	1.24	1.37	Resolution
LTOF Charge	$>$	0.60	0.53	0.67	$<$	1.30	1.23	1.37	Resolution
Tracker Track Normalized χ^2 X					$<$	4.0	2.7	7.4	Last Cut Efficiency
Tracker Track Normalized χ^2 Y (bending plane)					$<$	2.0	1.5	2.7	Last Cut Efficiency
TOF BetaH Spatial Normalized χ^2					$<$	2.0	1.5	3.5	Last Cut Efficiency
TOF BetaH Timing Normalized χ^2					$<$	8.0	6.0	10.0	Last Cut Efficiency
Clean TRD Cut									Unvaried
TRD Active Layers	$\geq$	10	9	11					Integer
TRD Electron Proton Log Likelihood	$\geq$	0.4	0.3	0.5					Last Cut Efficiency
TOF Truncated Mean $\mathrm{d}E/\mathrm{d}x$ Cut									Unvaried
No TRD Vertices									Unvaried

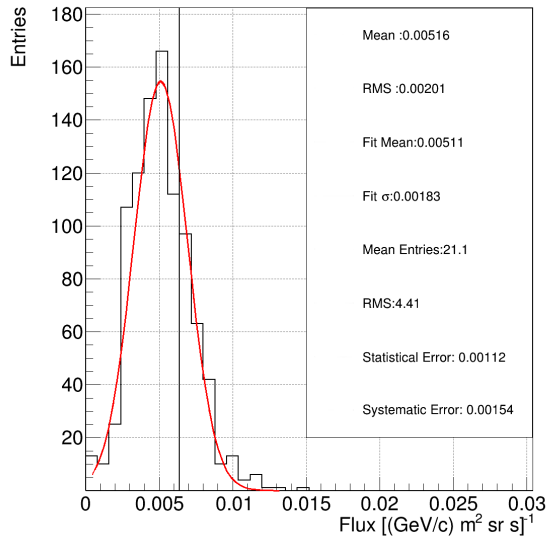

FIGURE 3.40: The distribution of resultant fluxes from the selection cut variation procedure for the reconstructed β bin 0.68-0.72.

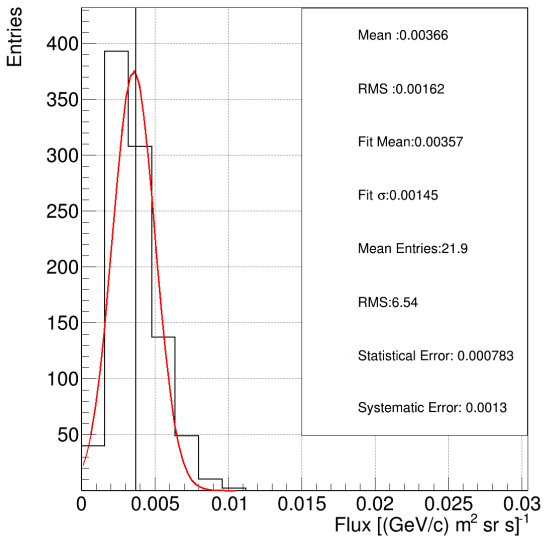

FIGURE 3.41: The distribution of resultant fluxes from the selection cut variation procedure for the reconstructed β bin 0.72-0.76.

Poisson statistical uncertainty, which is proportional to $\sqrt{N}$. The statistical variation in this procedure is not exactly the $\sqrt{N}$ uncertainty. In fact, the statistical fluctuations that should be subtracted is due to the events which are present in most of the flux permutations. This number is approximated by the mean statistics, N, minus the deviation of the counts, σ_N.

$$\sigma_{count} = \sqrt{N - \sigma_N}\frac{\Phi}{N} \tag{3.22}$$

The systematic uncertainty of the selection cuts is then:

$$\sigma_{sys} = \sqrt{\sigma^2_{total} - \sigma^2_{count}} \tag{3.23}$$

The uncertainty attributable to the unfolding procedure was estimated by looking at the spread of the oscillatory result for each flux bin. As noted in the unfolding section, the iterative procedure eventually sets up an oscillatory result. It can be seen from the fit χ^2 between iterations, Fig. 3.37, that after iteration 5 the χ^2/dof stays below 1. The following iterations are the oscillatory result. The uncertainty due to the unfolding procedure will be the RMS of the oscillatory result.

The unfolding procedure was allowed to continue beyond the exit condition, iterating a total of 20 times. Each iteration is normalized to the flux value at iteration 5. The flux ratio for the

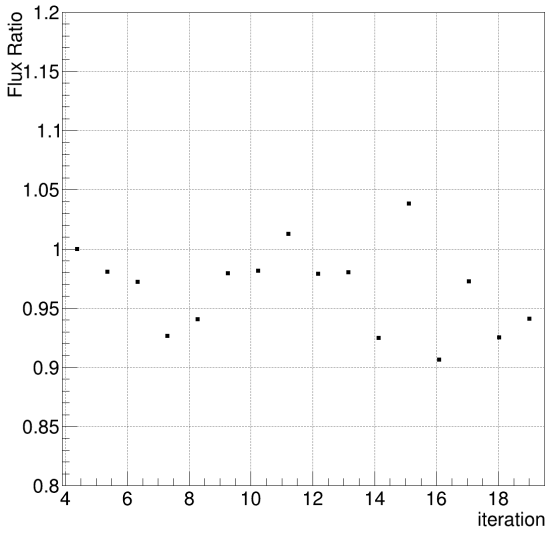

FIGURE 3.42: The oscillatory result for β bin 0.68-0.72 which defines the uncertainty of the unfolding procedure. The mean is 0.966 and the standard deviation is 0.035.

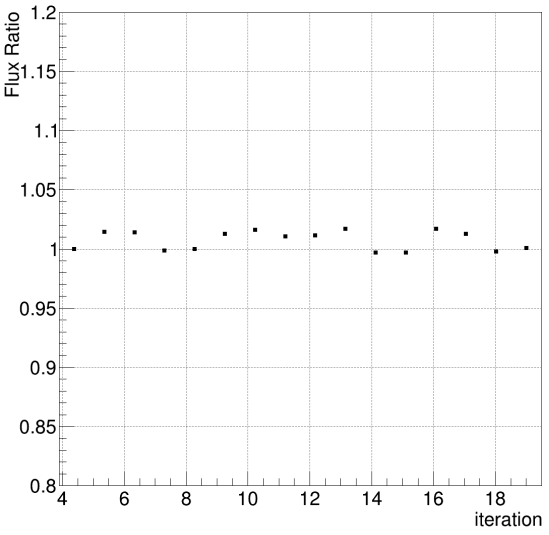

FIGURE 3.43: The oscillatory result for β bin 0.72-0.76 which defines the uncertainty of the unfolding procedure. The mean is 1.007 and the standard deviation is 0.008.

oscillatory result is presented for two example flux bins in Figs. 3.42 and 3.43. The mean flux ratio is consistent with 1. The average RMS is found to be about 2%.

The uncertainty attributable to the geomagnetic cutoff is estimated by varying the cutoff safety factor from 1.2 to 1.4. Altering the safety factor used for the geomagnetic cutoff can affect the analysis in two ways. The first way is by changing the number of events measured. If events are very near the cutoff value then it is obvious that changing the cutoff may then select more or fewer events. The other way that changing the safety factor can affect the analysis is by changing the measurement time. Since the measurement time is strongly affected by the geomagnetic cutoff for low rigidities, any change in its magnitude will affect the measurement time. The safety factor is included in the cutoff calculation, and thus the measurement time calculation as well.

As mentioned, the safety factor is varied up to 1.4. The flux is recomputed with the new measurement time using the new safety factor. The unfolding procedure is allowed to run for twenty iterations, and the average of the last 15 permutations is used for the value of the flux. The absolute deviation of the resultant flux between the value obtained using the 1.2 safety factor and the value obtained using the 1.4 safety factor is attributed as the uncertainty. Fig. 3.44 shows the percent difference between the different safety factors.

The overall estimate of uncertainty is obtained by adding all uncertainties considered in quadrature. The total uncertainty is shown as a percent in Fig. 3.45.

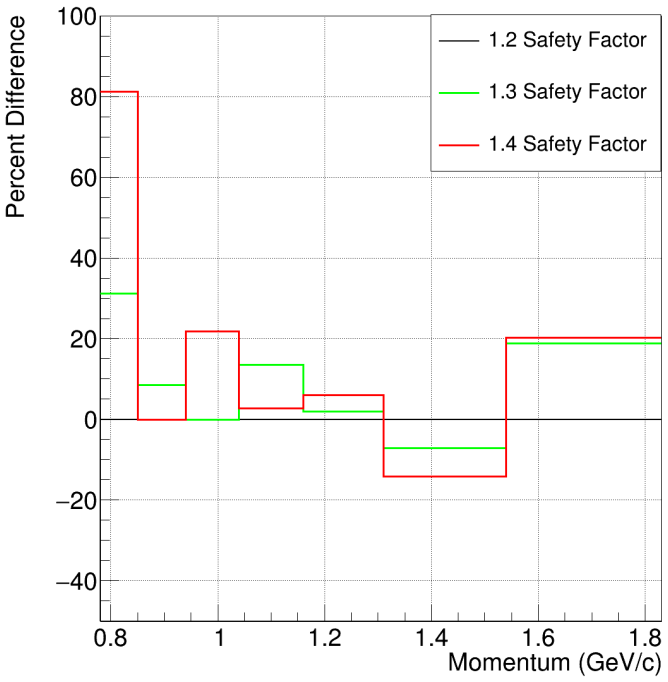

FIGURE 3.44: The percent difference between the flux calculated using the 1.2 safety factor and the 1.3 and 1.4 safety factor fluxes.

3.2.12 Galactic Antiproton Flux

The Galactic antiproton flux as measured by AMS-02 using the TOF for momentum reconstruction is presented. This analysis analyzed data taken between May 20, 2011 and May 12, 2017 using the B950 pass6 data reconstruction. Flux is calculated according to equation 3.1 as a function of momentum.

Observed Events $N_{obs}(p)$ is the number of events passing all cuts observed in a given momentum bin, Fig. 3.46. The "pion $\mathrm{d}E/\mathrm{d}x$" cut removes nearly all negatively charged pions and kaons. Electrons are effectively rejected by the TRD electron-proton likelihood cut. The predicted antideuteron flux, dark matter produced or not, is expected to be many orders of magnitude less than the antiproton flux at all energies. We may safely concluded that a mass cut is not needed for the antiproton flux analysis.

Momentum Binning Momentum in this analysis is calculated from the reconstructed TOF β, so in effect momentum bins may be thought of as β bins since we consider only one particle type, antiprotons. The bin width, Δp, should be greater than or equal to the resolution. The TOF has a constant measured β resolution of 4% for $\beta \simeq 1$. The reconstructed TOF β bin width is set to 0.04 to be always greater than the resolution of the TOF. Flux bins

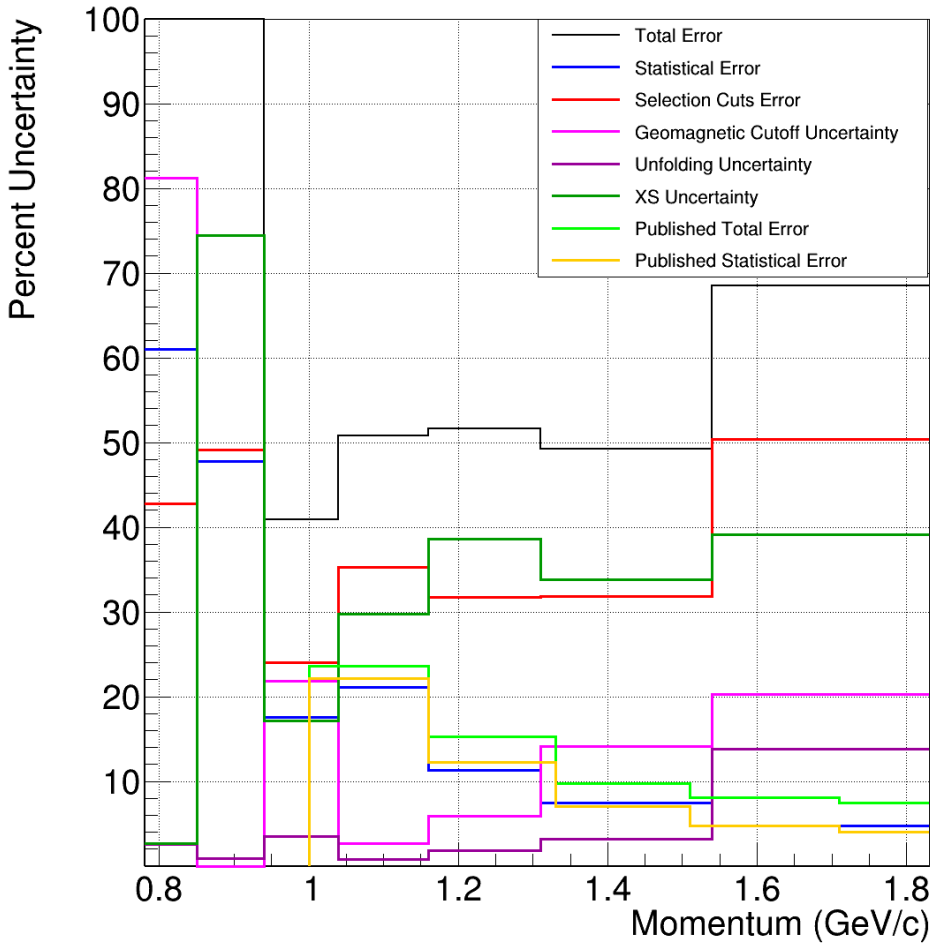

FIGURE 3.45: The percent uncertainty for the Galactic antiproton flux analysis.

must then be converted to top of the detector binning using the energy shift method from section 3.2.9. When converting to the top of the detector binning, a single flux bin will change in the following way. The bin edges and center will be shifted from reconstructed to true values. Changing the bin edges will typically change the bin width. The flux value is then rescaled by the ratio of the reconstructed bin width to the top of the detector bin width.

Trigger Efficiency The trigger efficiency, ϵ_{trig}, is measured as a function of reconstructed TOF β as shown in section 3.2.5. The binning was chosen to be the same as for the flux for ease of use. Because the trigger efficiency is measured as a function of reconstructed TOF β and the energy loss correction simply rescales the flux no modifications are needed.

Acceptance The detector acceptance is calculated from simulation as a function of generated momentum, where the generated momentum is the same as the top of the detector

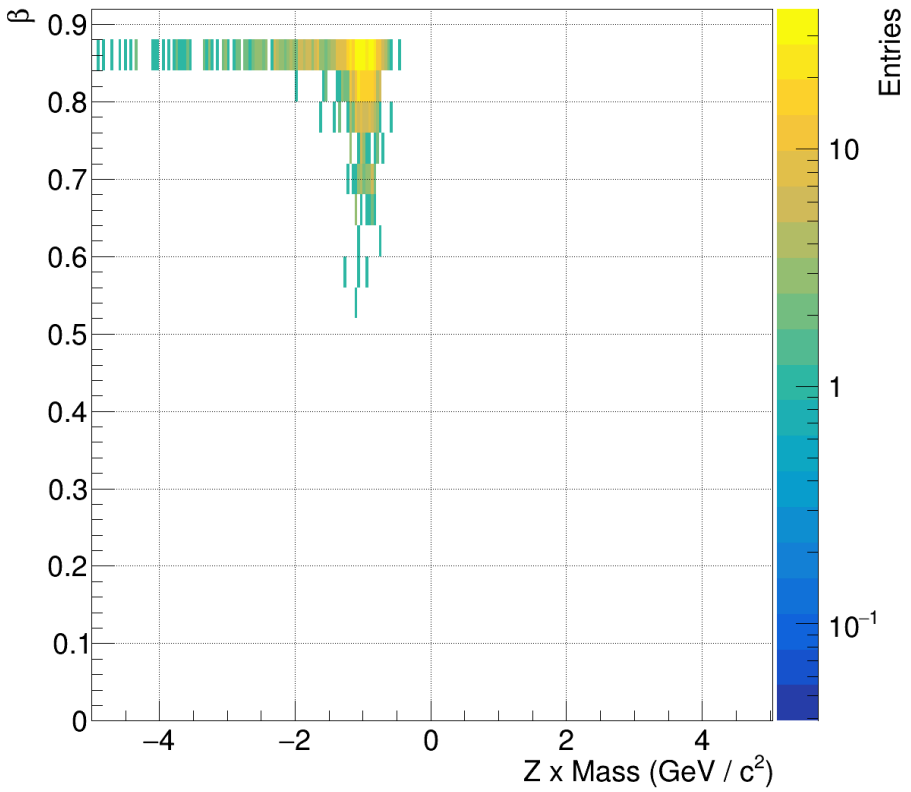

FIGURE 3.46: The distribution of observed Galactic Z = -1 events for reconstructed TOF $\beta \leq 0.88$ passing all cuts.

momentum. Therefore, the detector acceptance must be calculated using the top of the detector momentum binning obtained from the energy loss correction procedure.

Cut Correction Factor The overall cut correction factor is calculated as a function of reconstructed TOF β with the same binning as the flux. Each individual correction factor is restricted to 1.0 ± 0.1 so as to exclude unphysical corrections. As it turns out, most cut correction factors are nearly equal to 1.0, as can be seen in Fig. 3.33.

Measurement Time The measurement time, $T_{meas}(p)$, takes into account detector livetime spent above the geomagnetic rigidity cutoff. Because of the cutoff dependency, the measurement time is a function of rigidity. This analysis considers charge one particles, meaning that rigidity is equal to momentum. Therefore, the measurement time presented in section 3.2.6 is used for the Galactic antiproton flux calculation.

An event is considered to be of Galactic origin if the measured rigidity is greater than the Stöermer Geomagnetic Cutoff with a 1.2 safety factor. Typically, rigidity is obtained from the tracker. As this analysis is TOF velocity based, the reconstructed TOF β is used to calculate

rigidity assuming the antiproton mass. Consistency is kept by using reconstructed TOF β for both the cutoff cut as well as the measurement time calculation.

Before the Galactic antiproton result can be finalized it is important to consider the validity of the resultant flux. The first flux bin, corresponding to a reconstructed TOF β 0.60-0.64, contains only 2 events. It may not be appropriate to consider the flux a precision measurement given such low statistics. In addition to low statistics, this is an "edge bin" which are typically omitted. The two highest velocity bins, TOF β 0.80-0.84 and 0.84-0.88, are potentially beyond the scope of the TOF antideuteron analysis. At such high TOF velocities the reconstructed mass resolution degrades. As such, these bins will be dropped.

The Galactic antiproton flux measured by this analysis is presented in Fig. 3.47. Also compared are the already published AMS-02 results [12] as well as results from the BESS-Polar II balloon mission [57] and the PAMELA space based experiment [30]. It is seen that the results from this analysis are in agreement with previous results. This validates the use of the TOF for momentum binning as well as the quality cuts used.

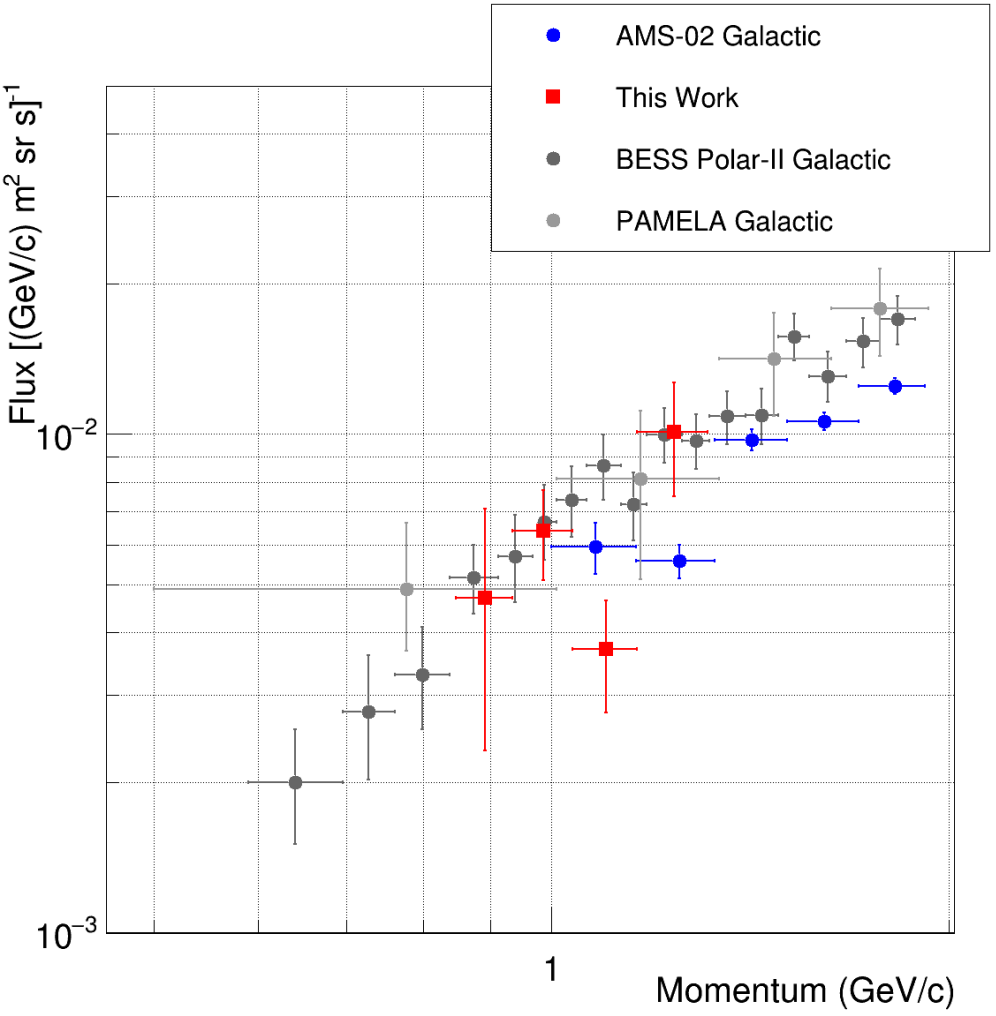

FIGURE 3.47: The Galactic antiproton flux measured as function of momentum. Also presented are the antiproton flux published by AMS-02 and other experiments.

TABLE 3.6: The $\bar{p}$ flux $\Phi^{\bar{p}}$ in units of $[\mathrm{m}^2\ \mathrm{sr\ s\ (GeV}/c)]^{-1}$ as a function of particle momentum at the top of AMS. $N^{\bar{p}}$ is the number of antiprotons observed in each momentum bin. σ_{stat} and σ_{syst} are the respective statistical and systematic errors.

Momentum [GeV/c]	TOF Velocity [c]	N$^{\bar{p}}$	$\Phi^{\bar{p}}$	σ_{stat}	σ_{syst}
0.85 - 0.94	0.64 - 0.68	9	0.0047	0.0022	0.0042
0.94 - 1.04	0.68 - 0.72	25	0.0064	0.0011	0.0024
1.04 - 1.16	0.72 - 0.76	19	0.0037	0.0008	0.0017
1.16 - 1.31	0.76 - 0.80	65	0.0101	0.0011	0.0051

Chapter 4

Low-Energy Antideuteron Analysis

The Galactic antiproton analysis was undertaken to inform the antideuteron analysis. This chapter first investigates the ambient flux given the very high antiproton statistics of this sample. The high statistics allows for the reconstructed mass resolution to be measured in data for a wide range of velocities. Reconstructed particle mass plays a critical role in differentiating antideuterons from antiprotons. In addition, energy deposition will be used to suppress antiprotons for the antideuteron analysis.

4.1 Ambient Antiproton Flux in Low Earth Orbit

As the Galactic antiproton result from this analysis compares well with previous results, it is concluded that the methods used are validated.

Antiprotons in Low Earth Orbit are not solely of Galactic origin. Antiprotons may be produced by cosmic rays impinging on the upper atmosphere of the Earth and get trapped in the geomagnetic field. Some of these antiprotons may survive long enough to reach the AMS-02 detector. These antiprotons will be below the geomagnetic cutoff and are thus not included in the Galactic antiproton flux analysis. The flux of below-geomagnetic-cutoff antiprotons has been measured to be an order of magnitude lower than the Galactic flux [58].

Although the below-cutoff flux is small relative to the Galactic flux, the flight path of AMS-02 means that the instrument spends the majority of the time in regions where the TOF rigidity range is below cutoff. What this amounts to is that the majority of antiproton events which are recorded by AMS-02 in the TOF range are near or below the geomagnetic cutoff.

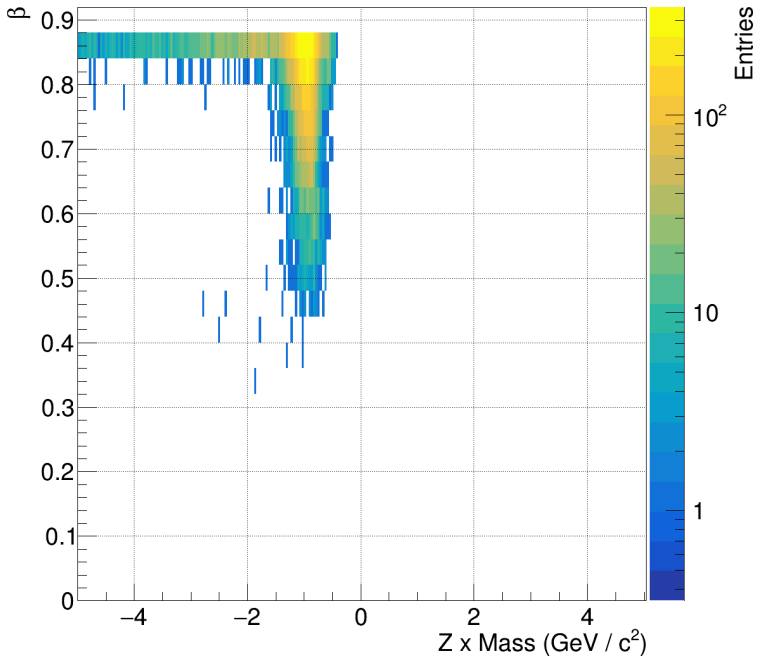

FIGURE 4.1: The distribution of observed Z = -1 events for reconstructed TOF $\beta \leq 0.88$ passing all cuts. No restriction has been placed on the geomagnetic cutoff.

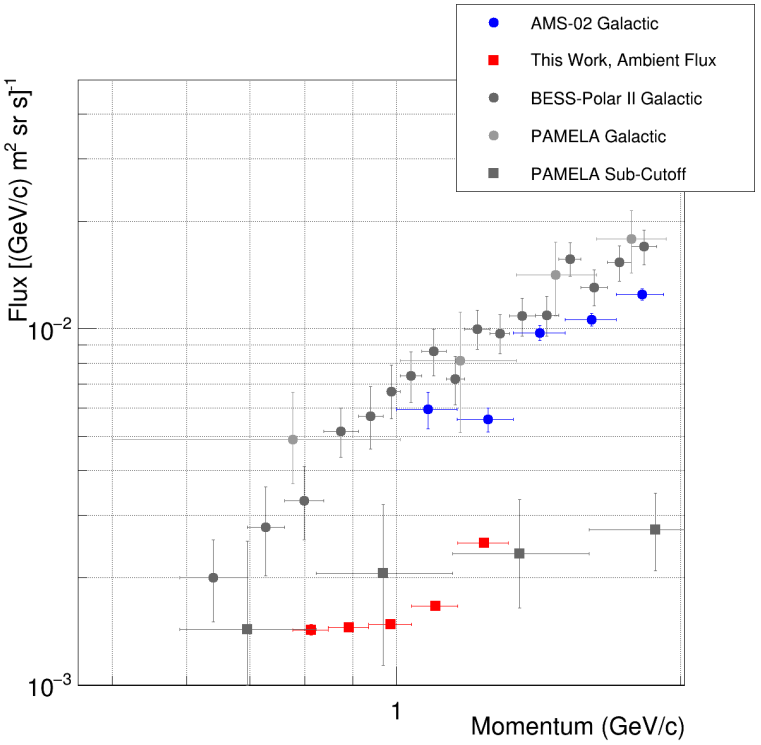

FIGURE 4.2: The ambient antiproton flux measured by AMS-02. The reconstructed velocity range was restricted to TOF β 0.60-0.80.

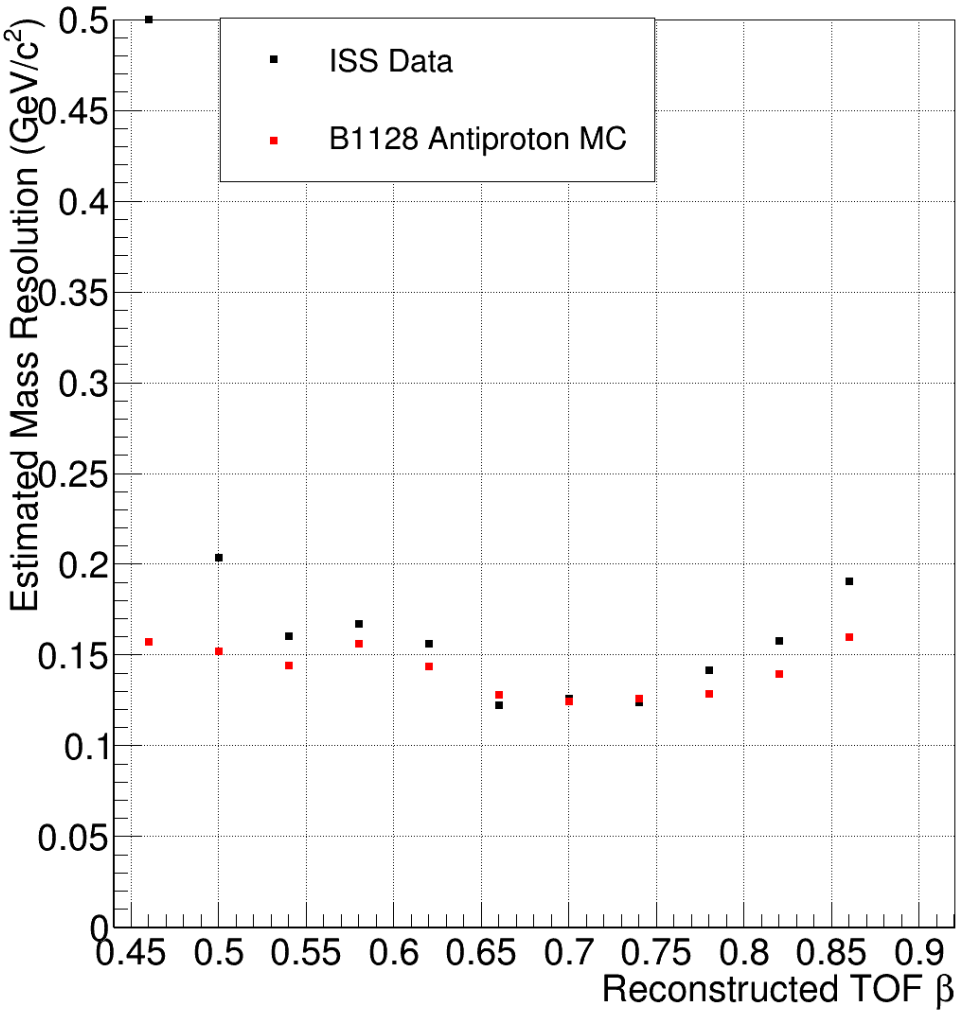

FIGURE 4.3: The estimated mass resolution (RMS) for observed Z = -1 events as a function of reconstructed TOF β. This is compared to B1128 antiproton MC which was reweighted with the ambient flux.

It is interesting to investigate the antiproton flux without imposing the cut on geomagnetic rigidity cutoff. This is the ambient antiproton flux, which is specific to the AMS-02 flight environment. The measurement time is no longer modulated by the geomagnetic cutoff and is a constant value for all momentum bins. Because of these reasons there will be significantly higher antiproton statistics when compared to the Galactic antiproton analysis.

All of the quality cuts were applied and the event distribution is shown in Fig. 4.1. A very clear antiproton peak is visible. The high statistics is a clear reason why the ambient flux is interesting.

Fig. 4.2 shows the ambient antiproton flux measured by AMS-02. The flux measurement was

restricted to a reconstructed TOF velocity range of β 0.60 to 0.80. The velocity selection was chosen to match the Galactic antiproton flux analysis. The error bars for the ambient flux are statistical.

It is interesting to investigate the reconstructed mass distribution for the different velocity bins. The increased data statistics for antiprotons allows the reconstructed mass distributions to be investigated for all velocity bins used in the Galactic antiproton analysis. The mass resolution was estimated by restricting the reconstructed mass to be between 0.5 GeV/c^2 and 1.5 GeV/c^2 and then taking the RMS of the distribution. The same procedure was done for B1128 antiproton simulation after it had been reweighted by the ambient antiproton flux. It is seen that the mass resolution measured from ISS data is comparable to that obtained from Monte Carlo (Fig 4.3). It is also seen that the resolution becomes very wide for the reconstructed TOF β bin 0.44-0.48. Clearly at this low velocity an antideuteron study is not feasible. A minimum velocity of $\beta >$ 0.50 should be imposed.

4.2 Antideuteron Analysis

4.2.1 Suppression of Antiprotons using Energy Depositions

Additional separation power between particles of different mass for low rigidities comes from using specific energy loss ($\mathrm{d}E/\mathrm{d}x$.) Energy depositions are notably recorded by the four TOF layers and the nine double sided tracker planes.

It is convenient to combine the energy deposition measurements from the tracker and TOF. In order to do this, the $\mathrm{d}E/\mathrm{d}x$ information must be normalized to the $\mathrm{d}E/\mathrm{d}x$ of minimum ionizing particles, called MIPs. This allows $\mathrm{d}E/\mathrm{d}x$ information from different materials, i.e. silicon and plastic, to be compared. Protons with a velocity of about $\beta = 0.9$, or a momentum of about 3 GeV/c, will be minimally ionizing in most materials. The MIP normalization is obtained from B1128 antiproton simulations as follows.

Good events are selected by passing the quality cuts from Ch. 3. No distinction is made between TOF, NaF, or aerogel events. To be sure that minimally ionizing particles are chosen, the events are sampled from the generated momentum range 3.0 to 4.0 GeV/c. The reconstructed tracker track is extrapolated to the central Z position of each TOF and tracker plane and the zenith angle at this layer is found. The energy deposition recorded on that plane is multiplied by the cosine of the zenith angle in order to account for the path length of material traversed. A peakfinding function is used to find the peak of the layer by layer $\mathrm{d}E/\mathrm{d}x$ distributions, Fig. 4.4. The peak is then used as the MIP normalization for that layer.

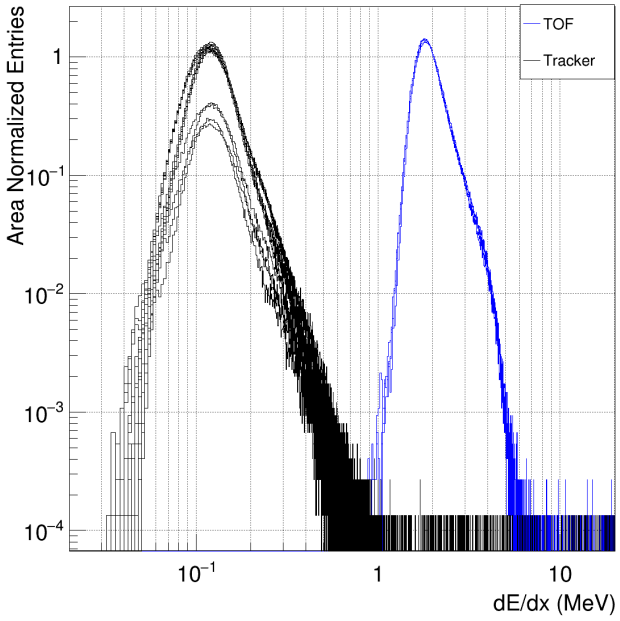

FIGURE 4.4: Energy depositions ($\mathrm{d}E/\mathrm{d}x$) observed in the tracker and TOF layers using the B1128 antiproton MC. Minimally ionizing particles were selected. The histograms have been rescaled for presentation such that the TOF histograms have area 1 and the tracker histograms have area 0.1. The average peak position was found to be 116 keV for tracker Y planes, 120 keV for tracker X planes, and 1.80 MeV for TOF planes.

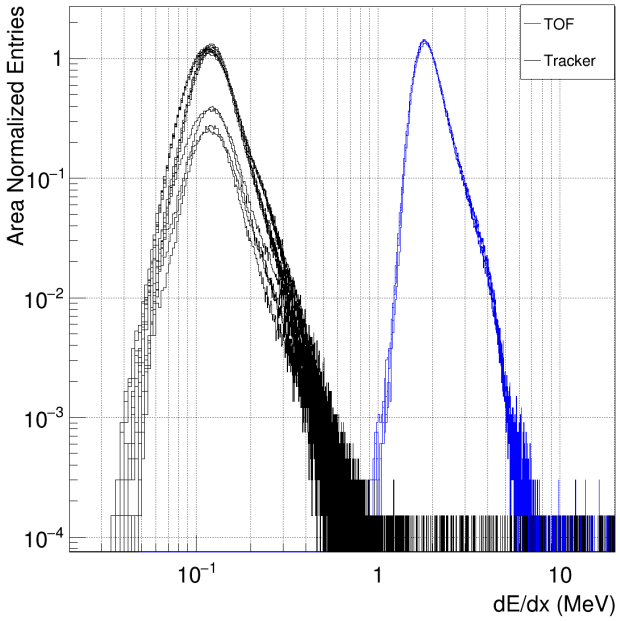

FIGURE 4.5: Energy depositions ($\mathrm{d}E/\mathrm{d}x$) observed in the tracker and TOF layers using the B1128 antideuteron MC. Minimally ionizing particles were selected. The histograms have been rescaled for presentation such that the TOF histograms have area 1 and the tracker histograms have area 0.1. The average peak position was found to be 116 keV for tracker Y planes, 121 keV for tracker X planes, and 1.80 MeV for TOF planes.

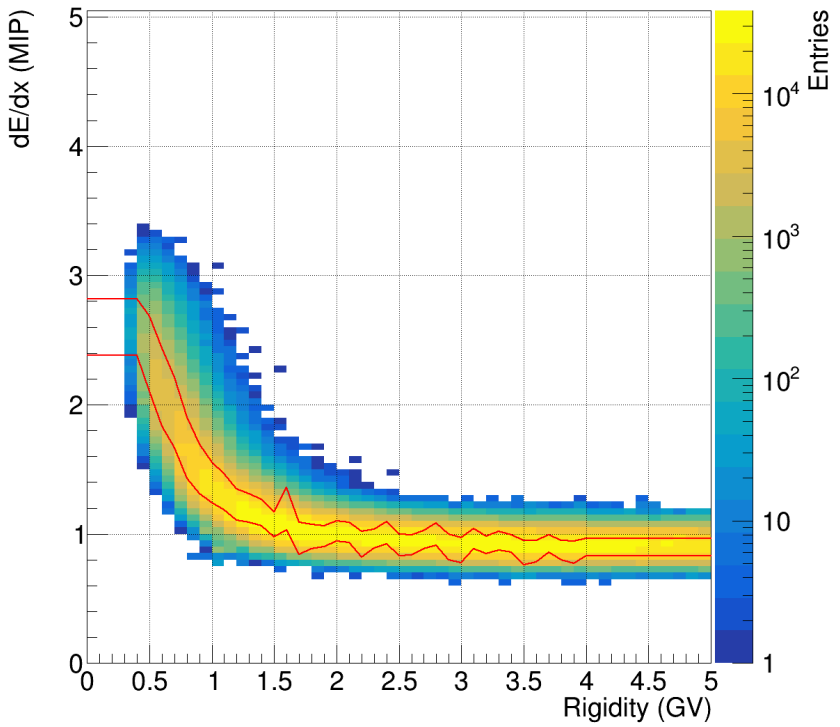

FIGURE 4.6: Energy depositions ($\mathrm{d}E/\mathrm{d}x$) as a function of reconstructed rigidity for B1128 antiproton MC. The 68% confidence interval is superimposed.

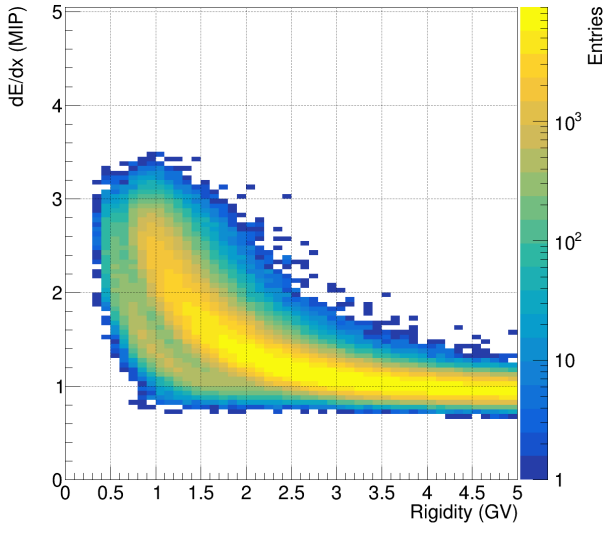

FIGURE 4.7: Energy depositions ($\mathrm{d}E/\mathrm{d}x$) as a function of reconstructed rigidity for B1128 antideuteron MC.

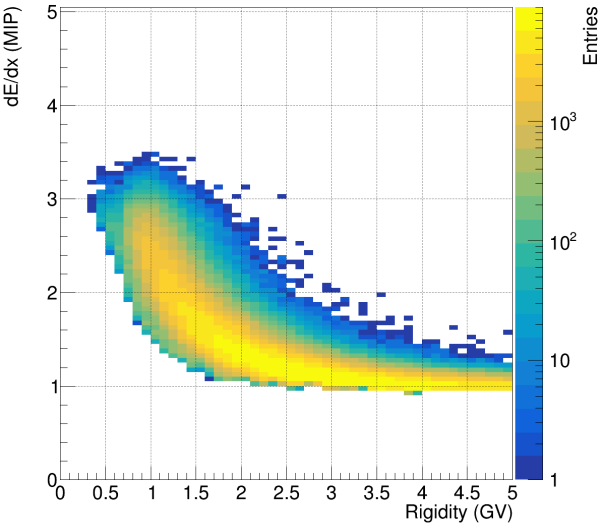

FIGURE 4.8: The upper antiproton $\mathrm{d}E/\mathrm{d}x$ bound has been applied as a lower edge cut.

$$-\left\langle \frac{dE}{dx} \right\rangle = Kz^2 \frac{Z}{A} \frac{1}{\beta^2} \left[\frac{1}{2} \ln \frac{2m_e c^2 \beta^2 \gamma^2 T_{max}}{I^2} - \beta^2 - \frac{\delta(\beta\gamma)}{2} \right] \tag{4.1}$$

From Eq. 4.1 it is evident that $\mathrm{d}E/\mathrm{d}x$ is a function of charge and velocity. Because antiprotons and antideuterons have the same charge, the MIP normalization is independent of which isotope is used as long as the events selected are in fact minimally ionizing. The B1128 antideuteron Monte Carlo was analyzed to confirm this, Fig. 4.5. The procedure was repeated with the generated momentum region selected to be 6.0-8.0 GeV/c to correspond to the MIP regime for deuteron mass. All MIP normalization values were found to be within one bin width of the antiproton values. Therefore, we may use the normalizations obtained from the antiproton Monte Carlo alone.

Events are reweighted with a spectra uniform in generated momentum. For each event, a truncated mean $\mathrm{d}E/\mathrm{d}x$ is obtained. Reconstructed hits on the track with non-zero energy depositions are path length corrected. These $\mathrm{d}E/\mathrm{d}x$ values are normalized to MIPs. Once the hits are expressed in MIPs, they are sorted and the average of the lower half is computed. For events which pass all quality cuts, the distribution of truncated mean $\mathrm{d}E/\mathrm{d}x$ is investigated as a function of reconstructed rigidity. A 2D-histogram is formed from these variables. Slices of rigidity are then taken and the 68% confidence interval of each resultant $\mathrm{d}E/\mathrm{d}x$ distribution is calculated. These confidence intervals as a function of rigidity set the bounds for the $\mathrm{d}E/\mathrm{d}x$ identification cut. The procedure was implemented for antiproton Monte Carlo shown in Fig. 4.6.

In order to compute the antideuteron $\mathrm{d}E/\mathrm{d}x$ band the following was done. Events were given a weight uniform in generated momentum. Next, the upper boundary of the antiproton $\mathrm{d}E/\mathrm{d}x$ band was used as a lower bound cut to remove breakup antiprotons from the antideuteron MC. Fig. 4.7 shows the distribution before applying the antiproton cut while Fig. 4.8 shows the distribution after the cut was applied. Finally, the 68% confidence interval is obtained for this antideuteron distribution. The antiproton and antideuteron $\mathrm{d}E/\mathrm{d}x$ bands are superimposed onto the antideuteron Monte Carlo distribution in Fig. 4.9.

4.2.2 Reconstructed Mass of Events

The final identification step is to look at the reconstructed mass of events. Mass is reconstructed from charge, velocity, and rigidity of an event by:

$$m = ZR\sqrt{\left(\frac{1}{\beta^2}\right) - 1} \tag{4.2}$$

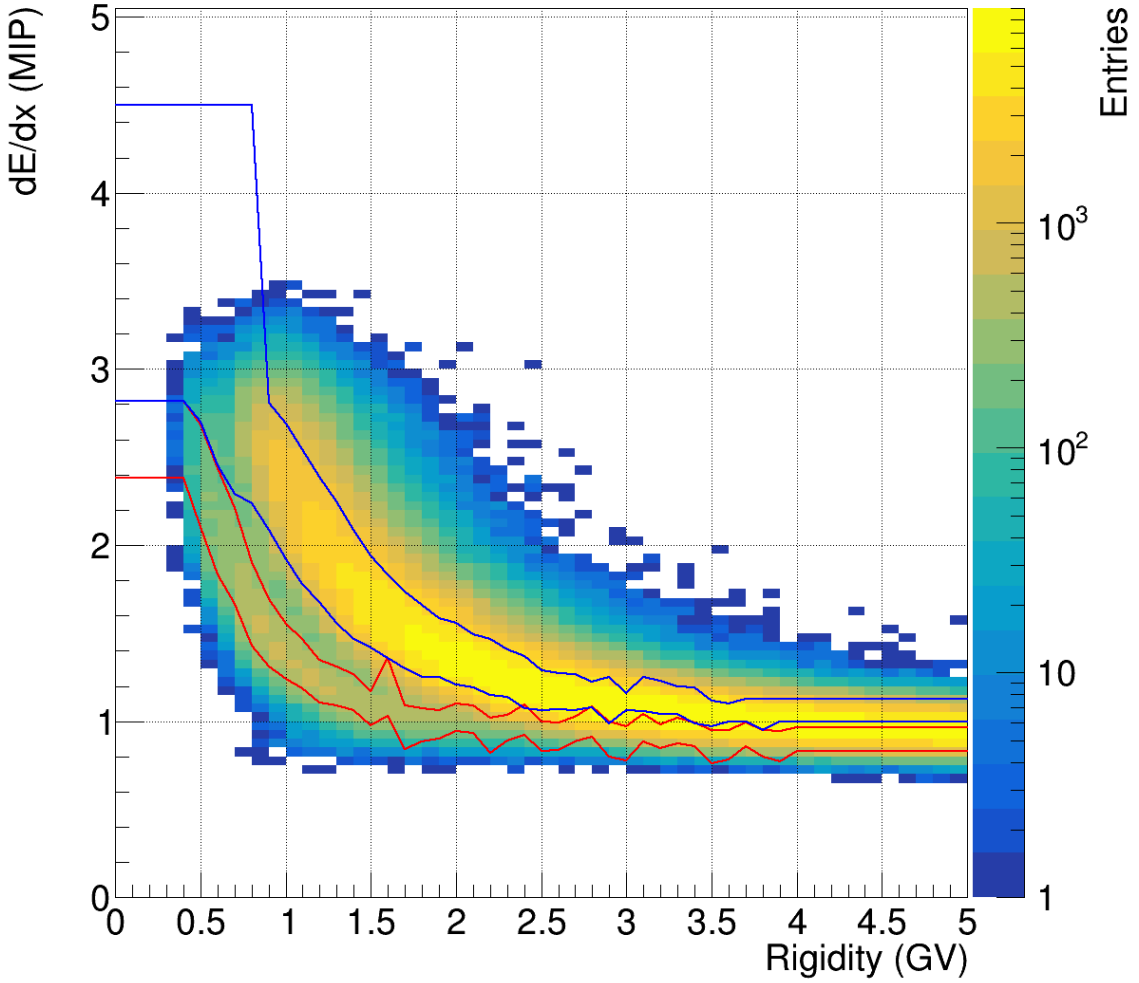

FIGURE 4.9: Energy depositions ($\mathrm{d}E/\mathrm{d}x$) as a function of reconstructed rigidity for B1128 antideuteron MC. Antiproton and antideuteron 68% confidence interval are superimposed.

Z being the particle charge, R the particle rigidity as measured by the tracker, and β the particle velocity/c.

Particle charge is measured by the TOF and the tracker. The quality cuts include a restriction on the overall tracker charge, the overall TOF charge, the Upper TOF charge, and the Lower TOF charge. By restricting the measured charge in these sub-detectors it is assumed that only charge one particles are accepted.

The antiproton MC is reweighted according to the antiproton flux published by the AMS-02 collaboration for high rigidities and those published by BESS-Polar II for low rigidities. It can be seen from the $\mathrm{d}E/\mathrm{d}x$ band cut (Fig. 4.9) that the antideuteron separation vanishes at a momentum of about 2.5 GeV/c. This corresponds to a reconstructed velocity of $\beta \approx 0.8$, which

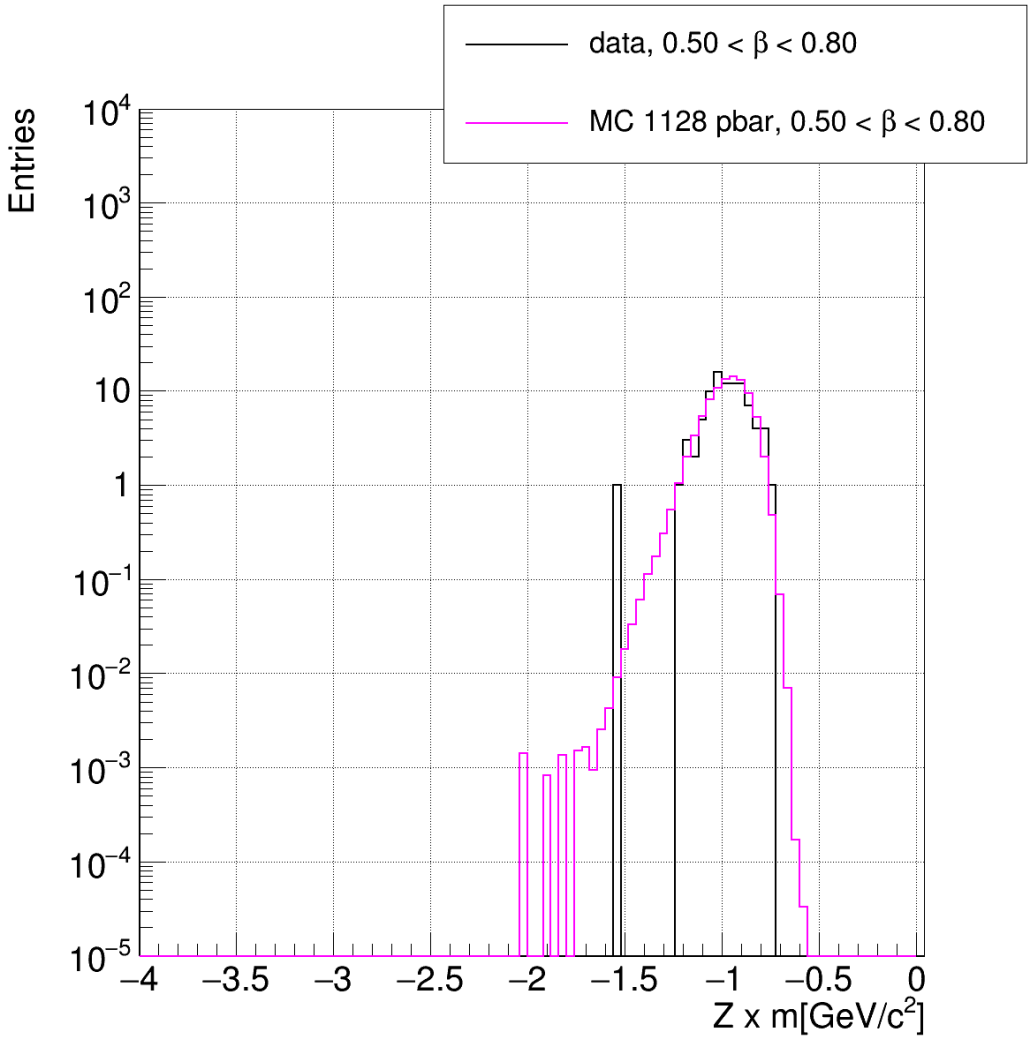

FIGURE 4.10: Galactic events which pass the antiproton band dE/dx cut for TOF β 0.50 to 0.80. B1128 antiproton MC is reweighted by the antiproton flux and rescaled such that the area of the peak is equivalent to the data statistics. The MC to data fit χ^2/ndf is 0.314. It is seen that the MC fits the data well.

is thus used as an upper limit on the reconstructed velocity. A velocity range of β 0.50-0.80 is imposed. The resulting mass distribution for data which passes the antiproton dE/dx band cut is obtained. The resulting mass distribution from antiproton simulation events which pass the antiproton dE/dx band cut is also obtained. This mass distribution is then rescaled such that the area of the distribution is equal to the event statistics of the data distribution, and the scale factor is saved. This same scale factor is then used to rescale the resulting mass distribution for antiproton MC events which pass the antideuteron dE/dx band cut. The now rescaled mass distribution of Monte Carlo antiprotons passing the antiproton dE/dx band is fit to the data mass distribution. It is found the the agreement is very good, with the fit χ^2/ndf less than 1, Fig. 4.10.

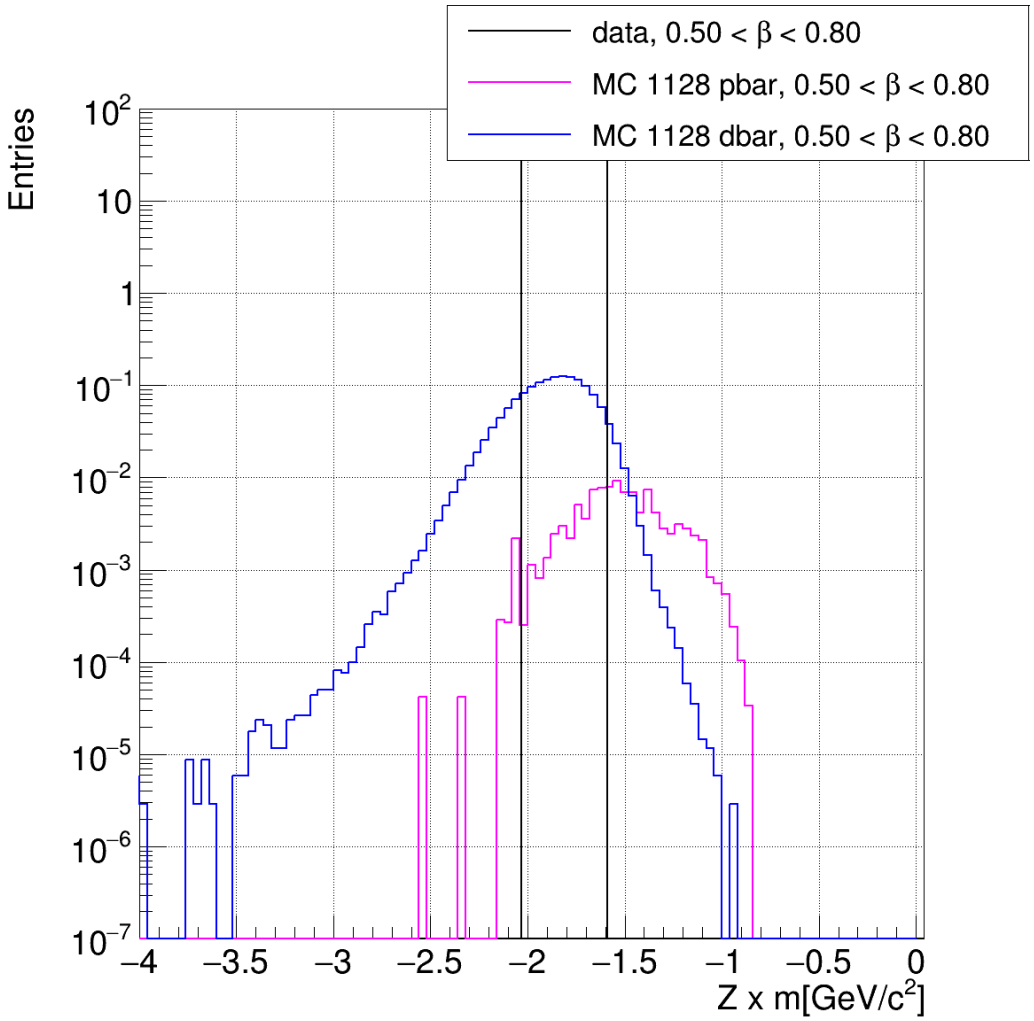

FIGURE 4.11: No Galactic events pass the antideuteron band dE/dx cut for TOF β 0.50 to 0.80. The B1128 antiproton MC has been reweighted by the antiproton flux. The distribution has then been rescaled by the same factor as for the antiproton band cut. B1128 antideuterons passing the antideuteron dE/dx band cut are shown with area equal to 1.5. The vertical lines show the 68% antideuteron mass confidence interval.

In order to determine the antiproton background contamination in the antideuteron mass range, the antideuteron mass range must be established. It is assumed that there is no heavy antimatter background. Therefore, an upper mass limit is not imposed. To find the lower antideuteron mass limit, the antideuteron Monte Carlo is used (Fig. 4.11). The antideuteron Monte Carlo input spectrum is not reweighted since the true flux is unknown. Thus, the generated spectrum being used is uniform in the logarithm of generated momentum. All quality cuts are applied. In addition to the quality cuts, the antideuteron band dE/dx cut is applied, and the reconstructed velocity is restricted to β 0.50-0.80. The 68% confidence interval is calculated for the resulting antideuteron mass distribution. The antideuteron mass range is estimated to be 1.59 GeV/c^2 to 2.09 GeV/c^2. As stated before, only the lower limit is considered.

Returning to the antiproton Monte Carlo mass distribution in the antideuteron $\mathrm{d}E/\mathrm{d}x$ band, the integral of the distribution for mass greater than 1.59 GeV/c^2 is obtained and found to be 0.035. This is the antiproton background for antideuterons.

4.2.3 Galactic Antideuteron Sensitivity

It is assumed that the main background source for the antideuteron search with AMS-02 is antiprotons with a misreconstructed mass due to finite detector resolution. In addition, the only other background to be considered comes from protons. Due to the sheer number of proton statistics, it may become important to consider charge confused events. Charge confusion is typically associated with very high energy events. These events approach the maximal detectable rigidity of the detector, with nearly no bending in the magnetic field. The tracking algorithm may then mistake a positive rigidity track for a negative rigidity track of some rigidity. Under normal circumstances the reconstructed velocity will be nearly equal to 1 and potentially produce a RICH ring if it happens to pass the radiator. However, since protons are wildly abundant, we attempt to estimate this unlikely background with extensive proton simulations.

Over 10 billion simulated proton events were analyzed with the selection cuts applied. No charged confused events were found. Fig. 4.12 shows the cut progression for the B1128 proton Monte Carlo. No event weighting was performed. This MC was generated over the full simulation cube instead of the top plane, producing up-going as well as horizontal events. One can see that all negative rigidity events have been excluded and the majority were excluded prior to the $\mathrm{d}E/\mathrm{d}x$ selection cut. Significantly more simulation will be required in the future to make an accurate estimation of the charge confused proton background.

Another potential possibility of proton contamination comes from misreconstructed up-going events. The time of flight system provides separation between up-going and down-going tracks at the 10^{-9} level [28]. The approximate Galactic proton flux is 1.7×10^3 $[(\mathrm{GeV}/n)\ \mathrm{m}^2\ \mathrm{sr}\ \mathrm{s}]^{-1}$ in the region of interest [59]. The multiplication of the proton flux level and the up/down discrimination power sets a worst case lower limit on the obtainable antideuteron sensitivity to 1.7×10^{-7} $[(\mathrm{GeV}/n)\ \mathrm{m}^2\ \mathrm{sr}\ \mathrm{s}]^{-1}$.

$$S = \sqrt{2N_o \ln\left[1 + \frac{N_o - N_{bg}}{N_{bg}}\right] - 2(N_o - N_{bg})} \tag{4.3}$$

Eq. 4.3 [60] gives the significance of a signal above a background in terms of Gaussian sigmas. Once the significance level has been decided, one may calculate the sensitivity to antideuterons by solving for N_o and substituting this for N_{obs} in the flux formula 4.4.

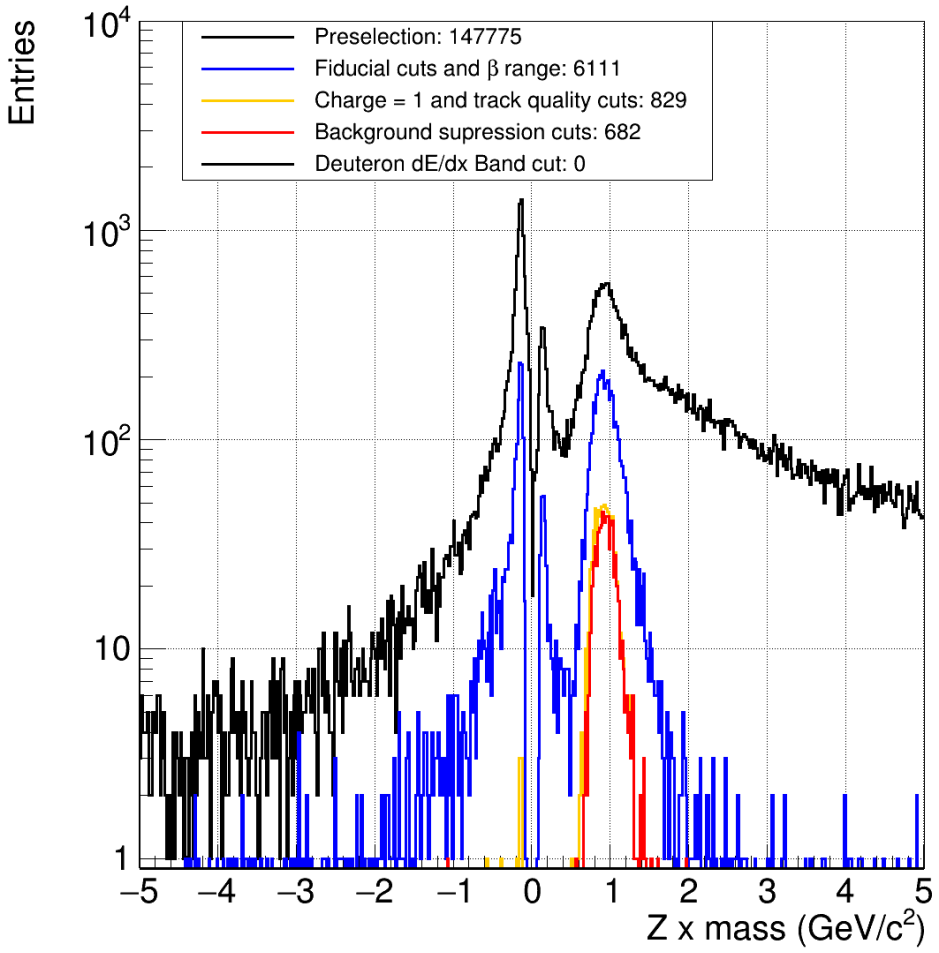

FIGURE 4.12: Reconstructed mass of B1128 proton Monte Carlo events as subsequent quality cuts are applied. No charge confused events are observed after all cuts.

$$\Phi(KE/n) = \frac{N_{obs}}{A(KE/n)\epsilon_{trig}(KE/n)T_{meas}(KE/n)\Delta KE/n} \tag{4.4}$$

The sensitivity is to be calculated for the reconstructed TOF velocity range 0.50-0.80 as a single bin. As energy is lost between the top of the detector and the TOF measurement, the top-of-the-detector, tod, momentum needs to be determined. To do this, the procedure from 3.2.9 is used. For this case, the antideuteron velocity map (Fig. 4.13) must be used. The input antideuteron momentum spectra is uniform in the logarithm of generated momentum. This is unchanged from the AMS-02 simulation generation scheme because the theoretical astrophysical antideuteron source spectra is unknown. It is found that $\beta_{rec} = 0.50$ maps to $\beta_{tod} = 0.54$ and $\beta_{rec} = 0.80$ maps to $\beta_{tod} = 0.81$.

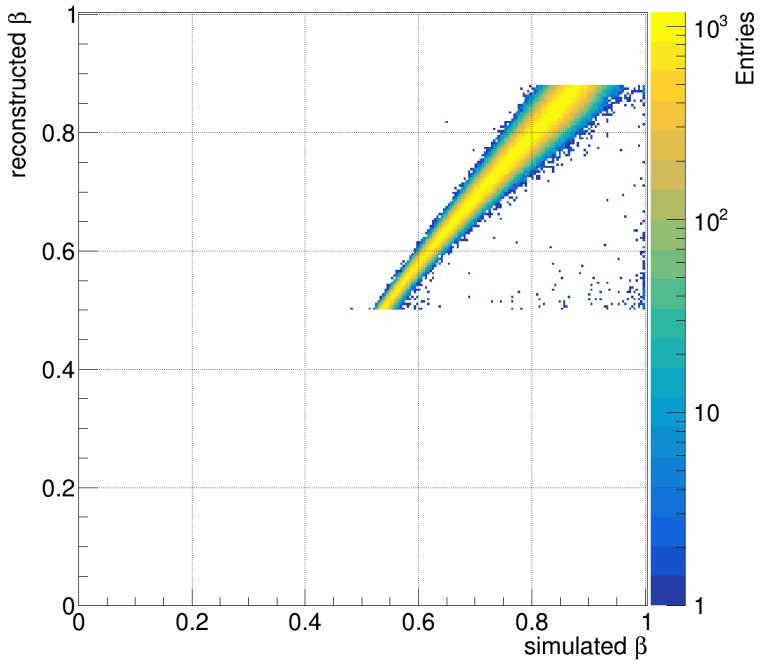

FIGURE 4.13: The velocity map for B1128 antideuteron MC events which pass all quality cuts, including the antideuteron band $\mathrm{d}E/\mathrm{d}x$ cut. A reconstructed velocity restriction of $0.50c$-$0.88c$ has been applied to reduce computation time.

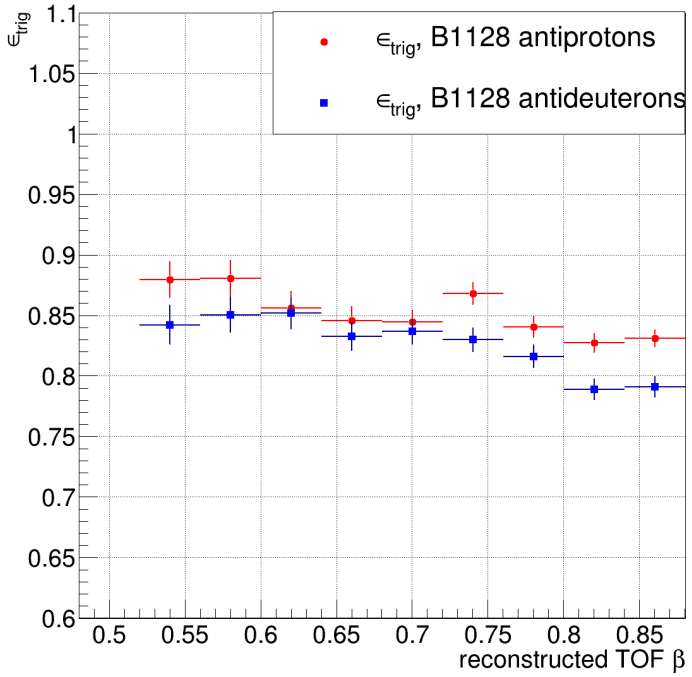

FIGURE 4.14: The B1128 MC trigger efficiency for antiprotons and antideuterons after all cuts, including the $\mathrm{d}E/\mathrm{d}x$ band cut.

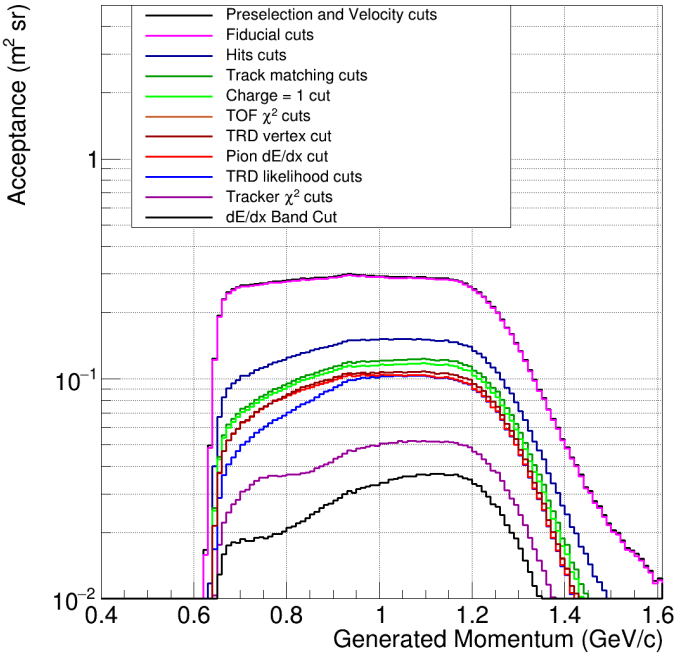

FIGURE 4.15: The B1128 antiproton MC acceptance as a function of generated momentum.

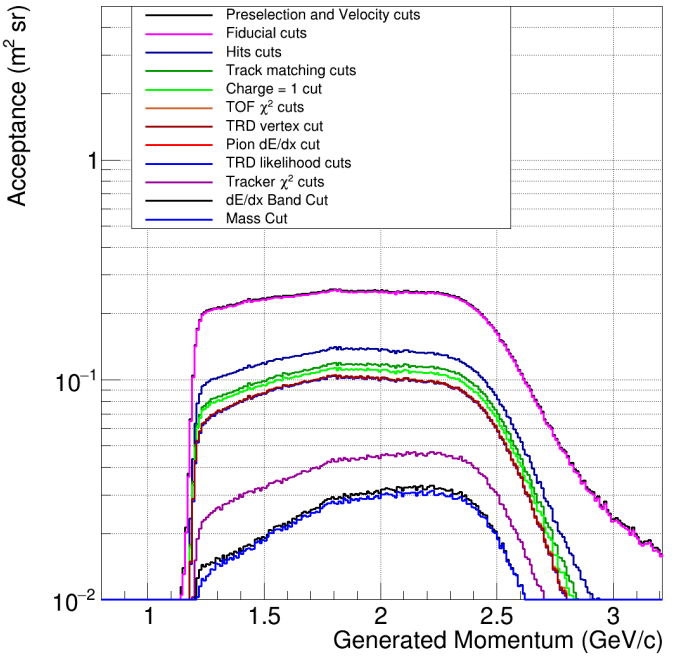

FIGURE 4.16: The B1128 antideuteron MC acceptance as a function of generated momentum.

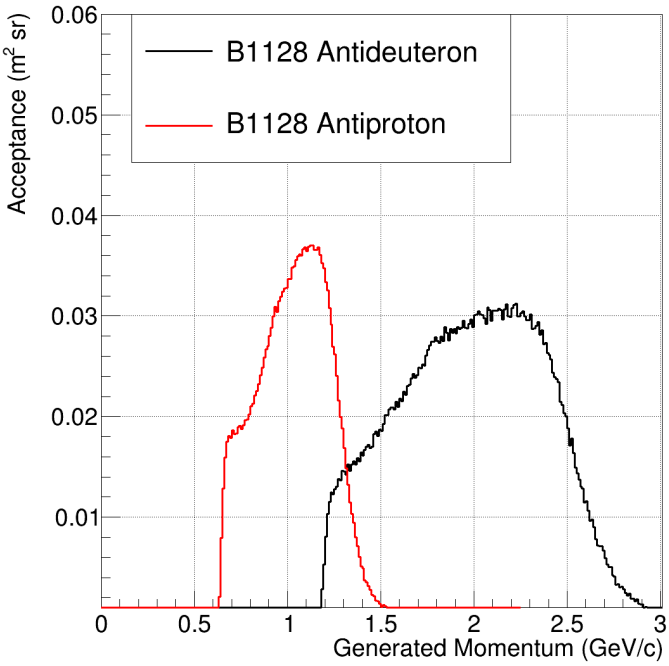

FIGURE 4.17: The B1128 antiproton and antideuteron MC acceptance as a function of generated momentum.

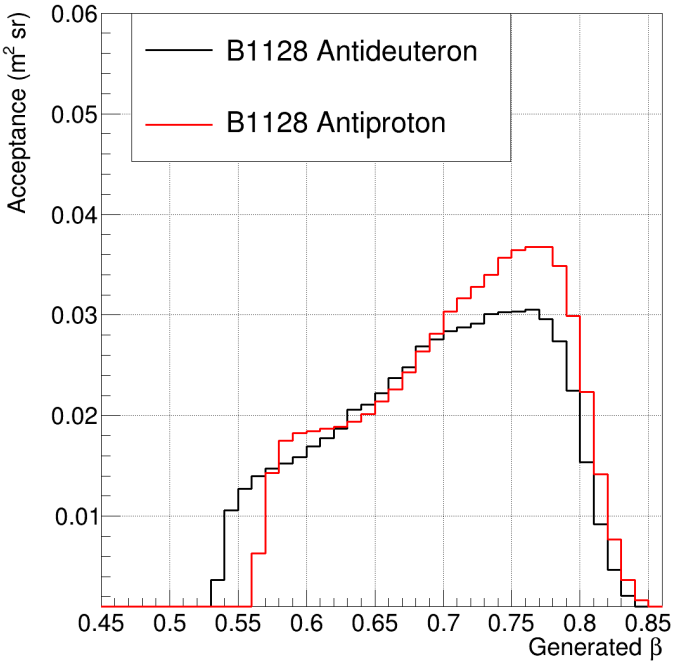

FIGURE 4.18: The B1128 antiproton and antideuteron MC acceptance as a function of generated velocity.

These top-of-the-detector velocity limits correspond to the kinetic energy per nucleon range of 0.17-0.65 GeV/n, which sets $\Delta KE/n$ to be 0.47 GeV/n. The top-of-the-detector velocity is also used to calculate the top of the detector rigidity for antideuterons. The velocity $0.54c$ corresponds to an absolute rigidity of 1.20 GV for antideuterons. The velocity $0.81c$ corresponds to an absolute rigidity of 2.55 GV for antideuterons. These rigidity limits are used to find the measurement time above geomagnetic cutoff, Fig. 3.30. A weighted average is computed to calculate the measuring time for this rigidity range, and it is found to be 7925455 s.

The antideuteron trigger efficiency is obtained from simulation. All quality cuts are applied in addition to the antideuteron band $\mathrm{d}E/\mathrm{d}x$ cut. The trigger efficiency is obtained as a function of reconstructed velocity, thus an average trigger efficiency in the velocity range 0.50-0.80 is used. This average antideuteron trigger efficiency is estimated to be 0.83 ± 0.01. Fig. 4.14 shows the Monte Carlo trigger efficiency after all cuts have been applied.

The antideuteron acceptance is estimated from Monte Carlo. It is important to ensure that the acceptance as the quality cuts are applied is well behaved for both antiproton and antideuteron MC. Figs. 4.15 and 4.16 show the acceptance progression of antiprotons and antideuterons, respectively. With all the analysis cuts applied the final acceptance is analyzed. Fig. 4.17 shows the final acceptances as a function of generated momentum. By investigating the acceptance as a function of generated velocity an accurate comparison of antiprotons to antideuterons can be made. Fig. 4.18 shows that the behavior of antiprotons and antideuterons are very similar, indeed.

An average acceptance is calculated. The acceptance is estimated as a function of generated momentum, which can be converted to generated velocity. All quality cuts, including the antideuteron band $\mathrm{d}E/\mathrm{d}x$ cut, are applied. In addition, a restriction of $0.50c$ to $0.80c$ is imposed on the reconstructed TOF velocity. Finally, the reconstructed mass is restricted to greater than 1.59 GeV/c^2. It is then simple to calculate the average antideuteron acceptance by integrating the acceptance histogram and then dividing by the range of integration. The average antideuteron acceptance is found to be 0.024 m^2 sr.

It can be shown by using Eq. 4.3 that to have a higher than 3σ antideuteron signal given a total background of 0.035 one must observe 1.59 events. Since it is not possible to see fractional events, 2 events must be observed. We may substitute 2 for N_{obs} into equation 4.4. The calculated discovery sensitivity at the 3σ-level to antideuterons is then found to be 2.69×10^{-5} [(GeV/n) m^2 sr s]$^{-1}$.

4.2.4 Optimization of the Antideuteron Sensitivity

No events survived all cuts and were above the geomagnetic cutoff. Because no candidate events were found, one may ask whether the selection cuts were too restrictive. On the assumption that there were no candidate events, it was decided to investigate varying the selection cuts in order to improve the antideuteron sensitivity. This was done using the antiproton and antideuteron simulations.

As has been emphasized, secondary particle suppression is very important to isolating a clean antiproton sample. No secondary suppression cuts should be tampered with. Fiducialization cuts should also not be adjusted.

4.2.5 Updating the $\mathrm{d}E/\mathrm{d}x$ Cut

The $\mathrm{d}E/\mathrm{d}x$ band cuts were developed to provide further separation power between antiprotons and antideuterons. This cut has good antiproton rejection power at the expense of moderate efficiency. One may recall that the bands are such that 68% of events of either antiprotons or antideuterons fall within their band. The choice of using a 68% confidence interval to define the cut was to be analogous to a 1 sigma region and was not to meet a certain rejection power. Since the goal of the cut is to reduce the antiprotons in the antideuteron region, one may ask whether the upper limit is necessary for the antideuteron band. By imposing only the lower edge of the antideuteron band cut the antideuteron last cut efficiency is improved while still providing strong separation power. Removing the upper $\mathrm{d}E/\mathrm{d}x$ band for antideuterons was investigated. The rejection power was found to be nearly identical for both the edge and band cuts.

4.2.6 Updating the Quality Cuts

In total eight of the quality cuts were selected for variation. The cuts to be varied are the TRD electron-proton likelihood, the number of inner tracker XY hits, the number of extra TOF clusters, the number of RICH hits, the normalized χ^2 of the tracker track fit for both X and Y, and the spatial and temporal normalized χ^2 of the TOF BetaH fit. The variation ranges for each cut were chosen to be looser than what was done for the study of systematic errors of the Galactic antiproton flux (3.2.11).

TRD electron proton likelihood The TRD electron proton likelihood (Fig. 4.19) cut is allowed to vary between 0.3 and 0.6. For antiproton MC it was observed that the majority of antiprotons have a TRD electron proton likelihood value between 0.6 and 1.0. There

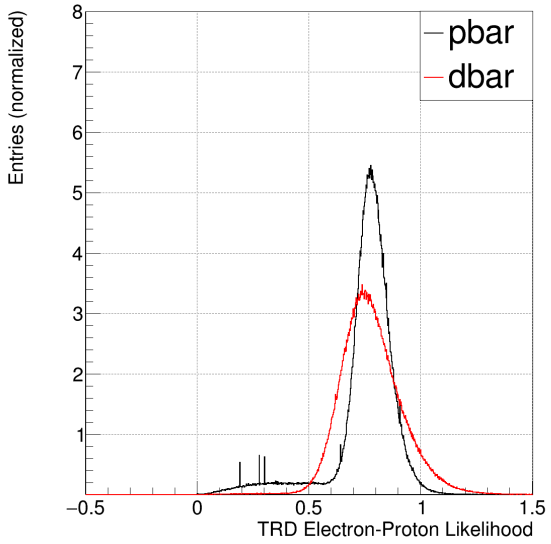

FIGURE 4.19: The B1128 Monte Carlo electron-proton likelihood distribution for antiprotons and antideuterons.

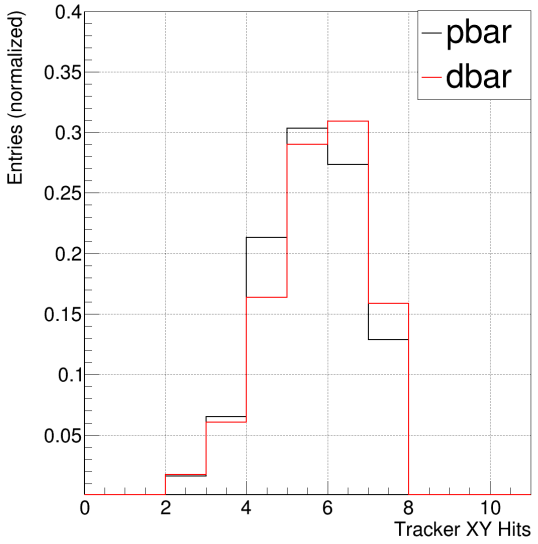

FIGURE 4.20: The B1128 Monte Carlo inner tracker XY hits distribution for antiprotons and antideuterons.

is also a plateau of events which have a likelihood value between 0.3 and 0.6. When only considering antiproton MC the plateau makes it not evident why a cut value of 0.4, the cut value used for the analysis, is any more useful than somewhere else in the plateau region. However, upon inspecting the antideuteron Monte Carlo the plateau is not present, and the antideuteron peak starts at very near an electron proton likelihood value of 0.4. It is useful to investigate this cut region.

Inner Tracker XY Hits The number of inner tracker XY hits (Fig. 4.20) used for the rigidity fit is required to be at least 5 for the Galactic antiproton flux analysis. In general the number of inner tracker hits can vary from 3 to 7. The fitting algorithm requires at least 3 inner tracker hits which sets the minimum. It was decided to investigate requiring one less or one more hit for the tracker fit, 4 or 6. By allowing one less hit there is a gain in cut efficiency. By requiring one more hit there is potential that the rigidity resolution, and thus the mass resolution, will improve.

Extra TOF Clusters Numerous cuts are devoted to ensuring that the TOF velocity measurement is of high quality. One way this is done is by requiring that the extrapolated tracker track matches the TOF cluster associated with the particle. It is therefore reasonable to assume that any TOF cluster which has a hit but does not match the tracker track will not influence the TOF β reconstruction. Only a single extra TOF cluster (Fig. 4.21) was allowed for the analysis. It was decided to investigate this selection cut in the range of no extra TOF clusters to a maximum of 1.

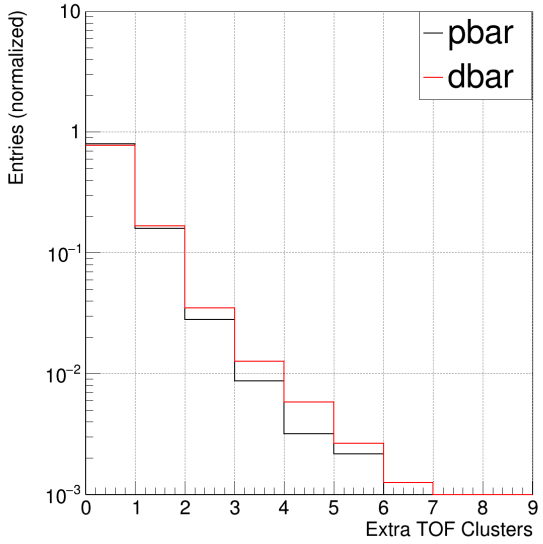

FIGURE 4.21: The B1128 Monte Carlo extra TOF clusters distribution for antiprotons and antideuterons.

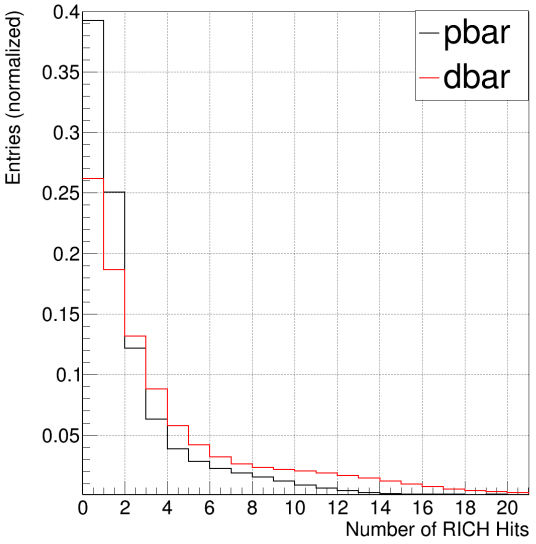

FIGURE 4.22: The B1128 Monte Carlo RICH hits distribution for antiprotons and antideuterons.

RICH Hits The number of RICH hits (Fig. 4.22) should not affect the separation of antiprotons from antideuterons. In fact, the maximum number of RICH hits restriction was put in place in an earlier stage of the analysis when it was seen in simulation that a few charge confused protons had a large number of RICH hits but no RICH ring. These events went away with the implementation of other cuts, but the RICH hits cut remained because it had high efficiency. The maximum number of RICH hits is allowed to vary up to 10 hits. It is also investigated if making this cut more strict can somehow help. The cut is allowed to vary to a low of no more than 2 RICH hits for completeness.

Tracker Track Fit χ^2 The tracker track normalized χ^2 (Figs. 4.23 and 4.24) cuts are some of the most restrictive cuts in the analysis (see Figs. 4.15 and 4.16). This was allowed because it was shown (Fig. 3.10) that the reconstructed mass resolution is correlated with the cut level on these variables. Since it is reasonable to consider that improved mass resolution leads to improved separation between antiprotons and antideuterons a restrictive cut was selected. However, since no candidate events survived the selection cuts, it becomes useful to see how much these cuts can be opened. Improving the cut efficiency will improve the antideuteron acceptance. If the background contamination can likewise remain reasonable, the sensitivity may be improved.

Another factor to consider is that the published AMS-02 antiproton flux used a cut level of 10 for both X and Y normalized tracker χ^2. The cut value for both the X and Y normalized χ^2 is investigated between the low value used for the systematic study, and

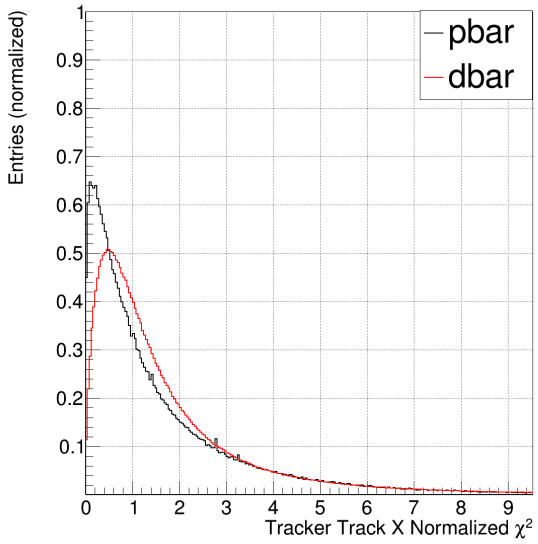

FIGURE 4.23: The B1128 Monte Carlo tracker track X fit normalized χ^2 distribution for antiprotons and antideuterons.

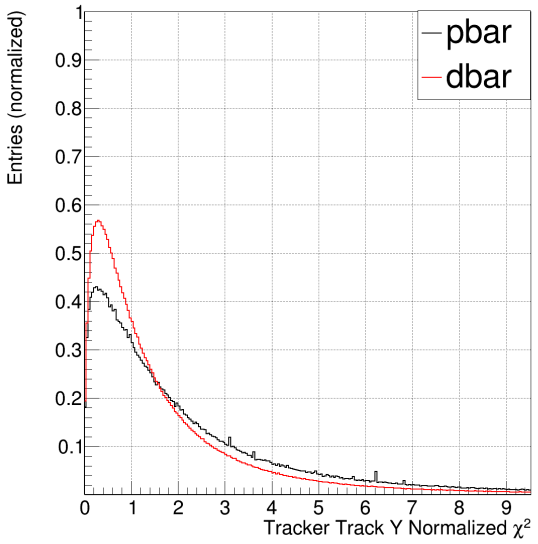

FIGURE 4.24: The B1128 Monte Carlo TOF BetaH spatial fit χ^2 distribution for antiprotons and antideuterons.

a high value of 10. For X the lower limit investigated is 2.66. For Y the lower limit investigated is 1.5.

TOF BetaH Spacial Fit χ^2 The TOF BetaH spatial χ^2 fit (Fig. 4.25) compares the tracker track to the TOF clusters used for the velocity measurement. Due to the fact one of the track matching cuts requires that the tracker track extrapolate to the hit TOF clusters, this cut can most likely be relaxed. Still, it may even be useful to tighten this cut in case the even more rigorous cut improves the background rejection. The cut value is investigated between ten percent lower efficiency at 1.5 to a high efficiency cut at 10.

TOF BetaH Timing Fit χ^2 The last cut variable to be investigated is the TOF BetaH timing χ^2 (Fig. 4.26). This cut compares the timing of the TOF clusters used for the velocity measurement with the tracker track. It may be beneficial to tighten this cut to improve the velocity measurement. This cut is allowed to vary from 6 to 10.

With the variables chosen for investigation and the ranges established for the cuts it is then a matter of how to investigate the resultant sensitivities. Both the antiproton and antideuteron Monte Carlo are analyzed. All the chosen cuts are varied simultaneously and randomly within the range of variation. The cut level for each cut is selected by sampling a uniform probability distribution. Tab. 4.1 summarizes the cuts which are varied and the ranges of variation.

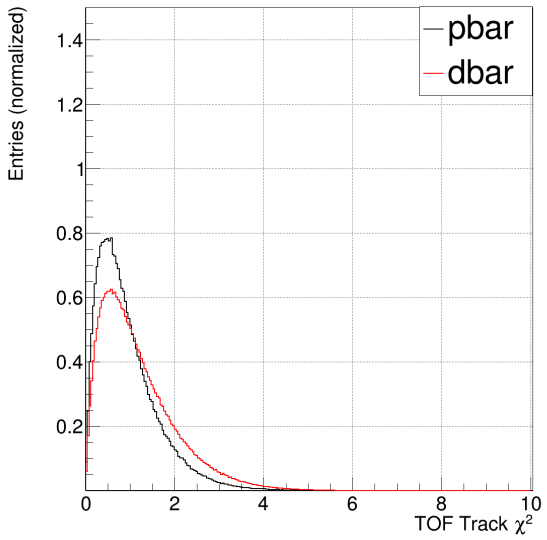

FIGURE 4.25: The B1128 Monte Carlo TOF BetaH spatial fit χ^2 distribution for antiprotons and antideuterons.

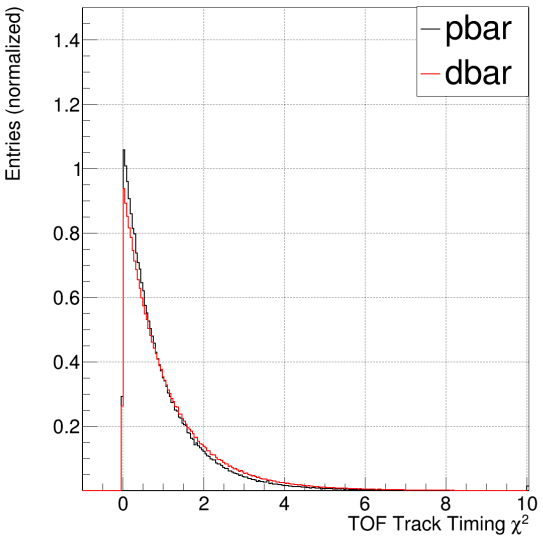

FIGURE 4.26: The B1128 Monte Carlo TOF BetaH timing fit χ^2 distribution for antiprotons and antideuterons.

TABLE 4.1: Cut investigation ranges to improve the antideuteron discovery sensitivity.

Cut		Primary Cut	Low	High
TOF Clusters NOT Associated with AMSParticle	$\leq$	1	0	1
Inner Tracker XY Hits	$\geq$	5	4	6
RICH Hits	$\leq$	7	2	10
Tracker Track Normalized χ^2 X	$<$	4.0	2.7	10.0
Tracker Track Normalized χ^2 Y (bending plane)	$<$	2.0	1.5	10.0
TOF BetaH Spatial Normalized χ^2	$<$	2.0	1.5	10.0
TOF BetaH Timing Normalized χ^2	$<$	8.0	6.0	10.0
TRD Electron Proton Log Likelihood	$\geq$	0.4	0.3	0.6

All the quality cuts are applied. The $\mathrm{d}E/\mathrm{d}x$ band cut is applied to antiproton MC while the $\mathrm{d}E/\mathrm{d}x$ edge cut is used for antideuteron MC. The antideuteron trigger efficiency is estimated for each cut variation. Also estimated for each cut variation is the antideuteron acceptance.

It is useful to first investigate the estimated sensitivities without rescaling the MC statistics which pass all cuts to the data statistics which pass all cuts. Doing this will result in the highest sensitivity to antideuterons given the high statistics of the Monte Carlo. What should become apparent will be that the amount of antiproton events with a reconstructed antideuteron like mass will be minimized. Another way to state this is that the antiproton-antideuteron separation will be maximized for a fixed antideuteron mass window.

For this demonstration 10,000 variations were performed and the resulting estimated sensitivity distribution is presented in Fig. 4.27. For reference the unvaried cut value sensitivity from this

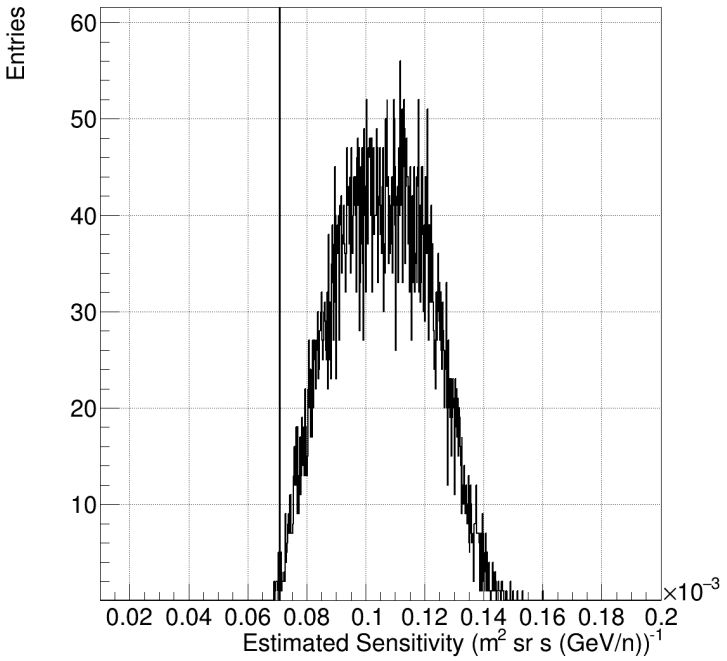

FIGURE 4.27: Without scaling the MC to data 10,000 variations were carried out and the resulting sensitivity estimates (with non-physical units) are shown. The vertical line shows the unvaried cut set using the sensitivity estimation procedure for reference.

procedure is marked with a vertical line. What is observed is that the basic cuts function as designed. The cuts were initially developed to minimize the number of proton Monte Carlo events falling in a fixed deuteron mass region using the available MC statistics at the time. This carried over to antiparticle Monte Carlo well. It is thus shown that the basic cuts provide maximal antiproton-antideuteron separation for a fixed antideuteron mass window.

The antiproton acceptance was calculated first for the basic cuts. Also for the basic cuts the data to Monte Carlo scale factor was obtained. It is assumed that the ratio of the antiproton acceptance, A, over the antiproton acceptance for a varied cutset, A', is equivalent to the data to Monte Carlo scale factor of the basic cuts, S, over the varied cutset, S'. Without having to run over the data for every cutset variation the data to Monte Carlo scale factor may be estimated by Eq. 4.5. By removing the requirement of analyzing the ISS data for every cut set the computation time per variation is reduced greatly.

$$S' = S\frac{A'}{A} \tag{4.5}$$

For each variation of the cuts, the antideuteron sensitivity is estimated using integer counts and requiring a greater than 3σ significance from Eq. 4.3. The basic cut set was used as a first test.

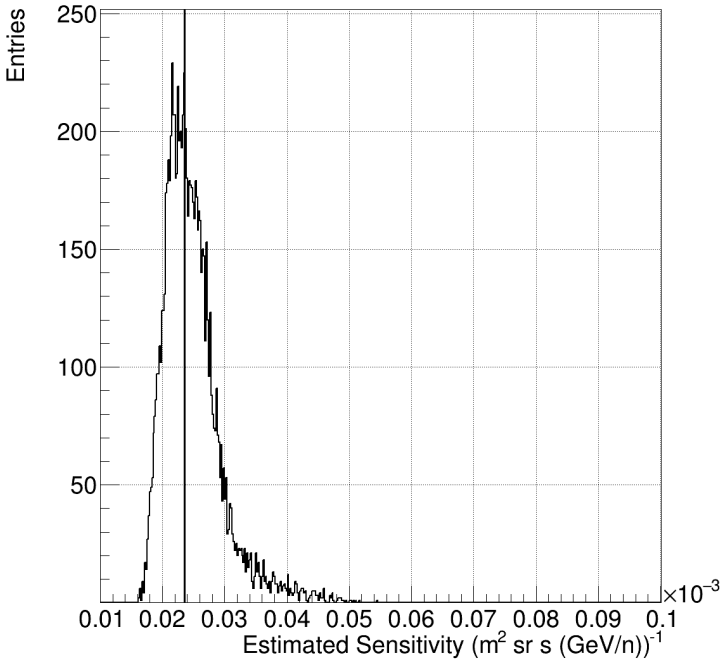

FIGURE 4.28: Including a MC to data scale factor, 10,000 variations were carried out and the resulting sensitivity estimates are shown. The vertical line shows the unvaried cutset, with the exception of the new $\mathrm{d}E/\mathrm{d}x$ low edge cut.

The procedure produced an estimated sensitivity for the basic cuts of 2.69×10^{-5} $[(\mathrm{GeV}/n)\ \mathrm{m}^2\ \mathrm{sr\ s}]^{-1}$, which is exactly what was reported above (Sec. 4.2.3). Removing the $\mathrm{d}E/\mathrm{d}x$ upper limit improved the antideuteron sensitivity to 2.36×10^{-5} $[(\mathrm{GeV}/n)\ \mathrm{m}^2\ \mathrm{sr\ s}]^{-1}$. The distribution of estimated sensitivities is shown in Fig. 4.28. It is observed that the basic cut set produces a sensitivity which is very near the most probable value of the distribution.

A few observations can be made based on the result of this optimization procedure. Fig. 4.29 depicts the estimated sensitivity with respect to the antideuteron acceptance. There are four distinct populations corresponding to the integer signal required to meet the 3σ significance condition. The population to the far left is the signal "1" population, the next to the right is the signal "2" population, and so on. It is observed that the best sensitivity is a member of the signal "2" population, which maximized the antideuteron acceptance. Fig. 4.30 shows how the estimated sensitivity behaves with respect to the antiproton background. Again, distinct populations become apparent which originate from the integer signal requirement. The cut set which produced the best sensitivity has maximized the antiproton background for the signal "2" population. Fig. 4.31 shows how the estimated antiproton background behaves with respect to the antideuteron acceptance. It is clear that the background is directly proportional to the acceptance.

TABLE 4.2: Quality cuts which provide the best sensitivity to antideuterons.

Cut					Cut Group
Tracker Track Zenith Angle at L2			$\leq$	45°	Fiducial Cuts
Tracker Track Zenith Angle at RICH Radiator			$\leq$	45°	Fiducial Cuts
Tracker Track Radius at Z = 0			$<$	47.0 cm	Fiducial Cuts
Extrapolated Tracker Track RICH crossing radius			$<$	80.0 cm	Fiducial Cuts
TOF Clusters Associated with AMSParticle	$=$	4			Hits Cuts
TOF Clusters NOT Associated with AMSParticle			$\leq$	1	Hits Cuts
ACC Hits			$\leq$	1	Hits Cuts
Inner Tracker XY Hits	$\geq$	5			Hits Cuts
RICH Hits	$\geq$	0	$\leq$	9	Hits Cuts
Tracker Track TOF Hit Matching					Track Matching Cuts
TRD Vtrack Tracker Track residual azimuth angle at UTOF			$<$	6.27°	Track Matching Cuts
TRD Vtrack Tracker Track residual zenith angle at UTOF			$<$	2.19°	Track Matching Cuts
Total UTOF Energy Deposition	$>$	3.0 MeV			Charge Cuts
Total LTOF Energy Deposition	$>$	3.0 MeV			Charge Cuts
Tracker Charge	$>$	0.700	$<$	1.300	Charge Cuts
Overall TOF Charge	$>$	0.700	$<$	1.300	Charge Cuts
UTOF Charge	$>$	0.700	$<$	1.300	Charge Cuts
LTOF Charge	$>$	0.600	$<$	1.300	Charge Cuts
Tracker Track Normalized χ^2 X			$<$	7.78	χ^2 Cuts
Tracker Track Normalized χ^2 Y (bending plane)			$<$	2.48	χ^2 Cuts
TOF BetaH Spatial Normalized χ^2			$<$	7.11	χ^2 Cuts
TOF BetaH Timing Normalized χ^2			$<$	8.15	χ^2 Cuts
Clean TRD Cut					TRD Likelihood Cuts
TRD Active Layers (Used in likelihood calculation)	$\geq$	10			TRD Likelihood Cuts
TRD Electron Proton Log Likelihood	$\geq$	0.52			TRD Likelihood Cuts
TOF Truncated Mean $\mathrm{d}E/\mathrm{d}x$ Cut (remove pions and kaons)					$\mathrm{d}E/\mathrm{d}x$ Cut
Antideuteron Edge $\mathrm{d}E/\mathrm{d}x$ Cut					$\mathrm{d}E/\mathrm{d}x$ Cut
No TRD Vertices					TRD Vertex Cut

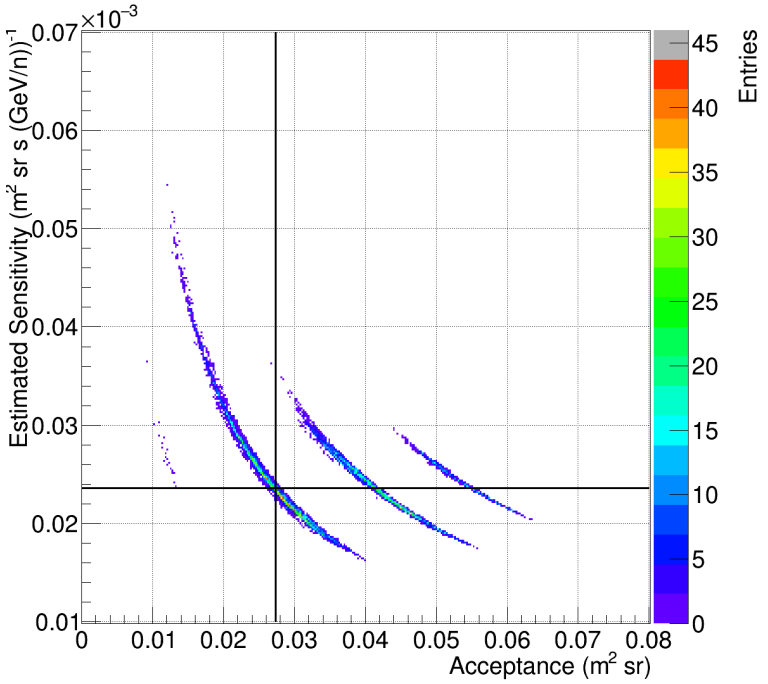

FIGURE 4.29: 10,000 variations were carried out and the resulting sensitivity estimates and acceptance are shown. The crosshair shows the result from the unvaried cutset. Distinct populations are observed which correspond to different integer signals.

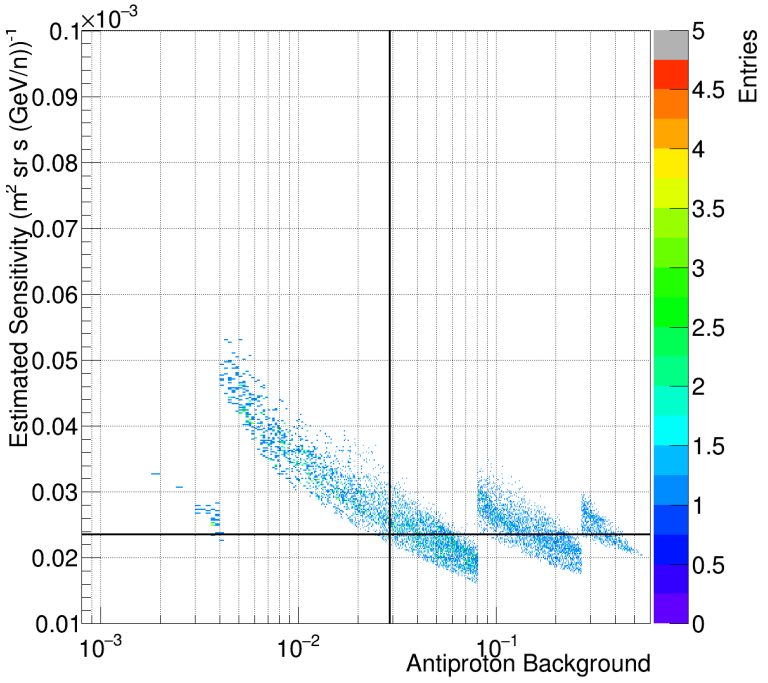

FIGURE 4.30: 10,000 variations were carried out and the resulting sensitivity estimates and antiproton background are shown. The crosshair shows the result from the unvaried cutset. Distinct populations are observed which correspond to different integer signals.

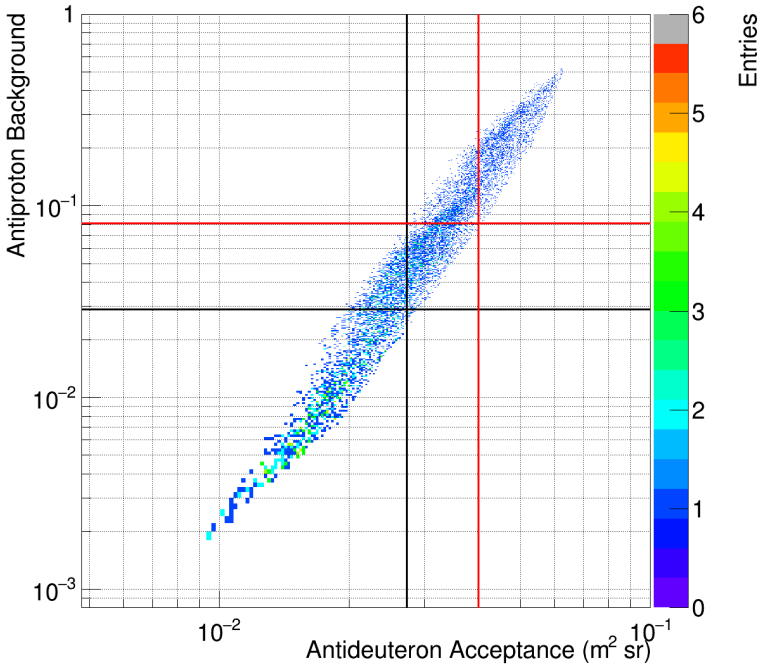

FIGURE 4.31: 10,000 variations were carried out and the resulting antideuteron acceptances and antiproton background are shown. The black crosshair shows the result from the unvaried cutset while the red crosshair show the optimized cuts.

The cut values which produced the best estimated sensitivity, Tab. 4.2, were analyzed further. It is found that the optimized cut set produces a clean data sample. The antiproton mass distribution is well described by Monte Carlo (Fig. 4.32). After properly scaling the reconstructed Monte Carlo statistics to the reconstructed data statistics the antiproton background is estimated to be 0.081 for a reconstructed mass greater than 1.59 GeV/c^2. If two antideuterons are observed this gives a significance of exactly 3. The antideuteron acceptance has been increased to 0.041 m^2 sr. The resulting sensitivity to antideuterons is found to be 1.58×10^{-5} [(GeV/n) m^2 sr s]$^{-1}$.

A single event survives all of the identification cuts. The reconstructed mass is 2.80 GeV/c^2. There are a large number of hits in tracker layer 2 which are not near the particle track. It is also observed that the reconstructed TOF velocity, $\beta = 0.79$, is very close to the upper limit of this analysis. This particular event is thus questionable. Furthermore, the next generation AMS-02 reconstruction algorithm yields a positive rigidity because it rejects the layer 2 hit. It is safe to exclude this event, thus no candidates survive.

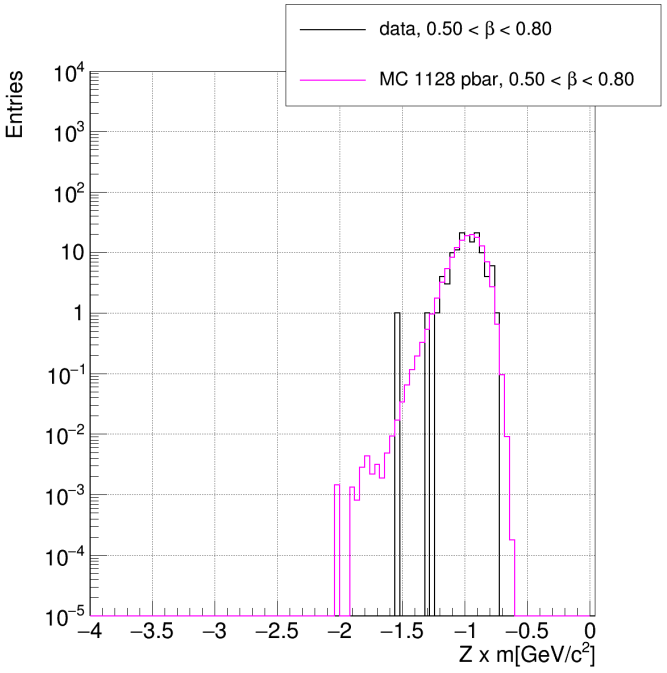

FIGURE 4.32: Galactic events which pass the antiproton band $\mathrm{d}E/\mathrm{d}x$ cut for TOF β 0.50 to 0.80. B1128 antiproton MC is reweighted by the antiproton flux and rescaled such that the area of the peak is equivalent to the data statistics. The MC to data fit χ^2/ndf is 0.431. It is seen that the Monte Carlo fits the data well.

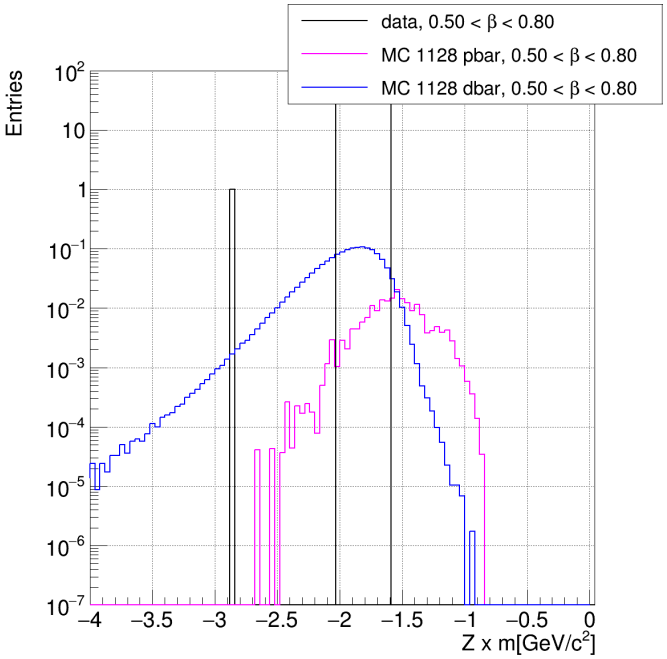

FIGURE 4.33: Galactic events which pass the antideuteron $\mathrm{d}E/\mathrm{d}x$ low edge cut for TOF β 0.50 to 0.80. The B1128 antiproton MC has been reweighted by the antiproton flux. The distribution has then been rescaled by the same factor as for the antiproton band cut. B1128 antideuteron MC passing the antideuteron $\mathrm{d}E/\mathrm{d}x$ low edge cut are shown with area equal to 1.5 for visual purposes.

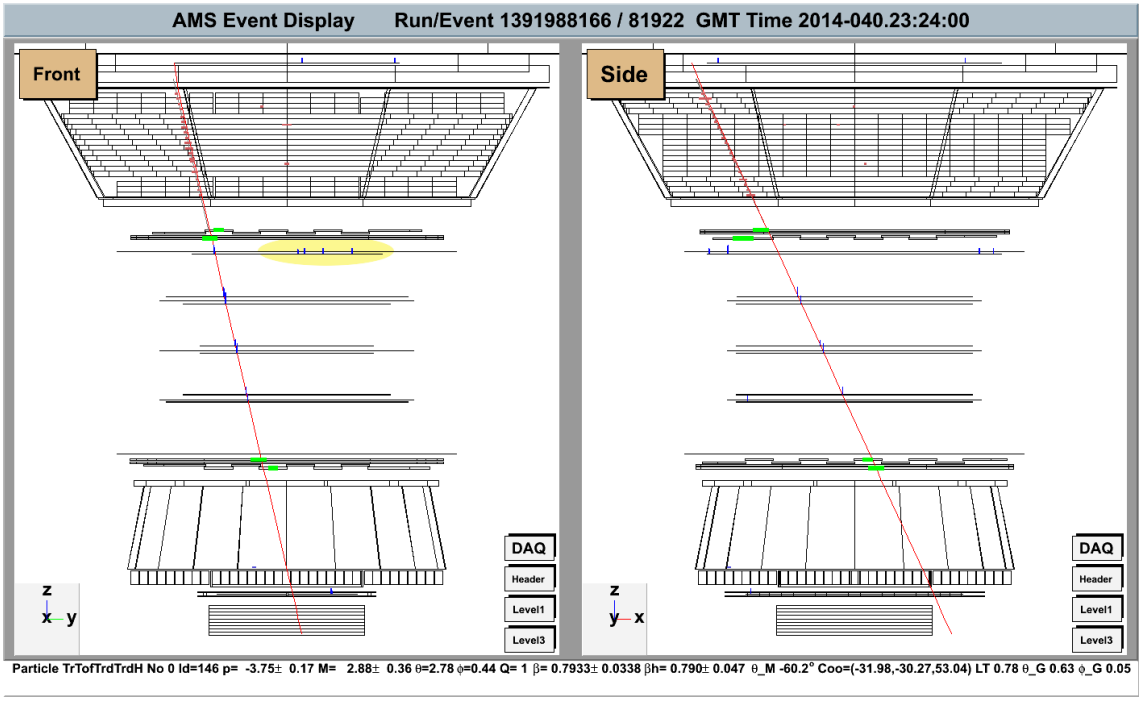

FIGURE 4.34: Event display for the surviving above cutoff event. The mass is reconstructed to be 2.80 GeV/c^2. Tracker layer 2 has a large quantity of hits located away from the particle track. These extra tracker hits make one question if this event is properly reconstructed.

4.2.7 Antideuteron Exclusion Limit

Though similar there are fundamental differences between the sensitivity to antideuterons and the antideuteron exclusion limit. The sensitivity to antideuterons is a prediction based on simulation. The antideuteron exclusion limit is established based on simulation as well as analyzed data given a null observation. No antideuteron event candidates survive, therefore an exclusion limit can be established. The Feldman-Cousins [61] statistical approach is used to set the antideuteron exclusion limit at the 95% confidence level. The lowest exclusion limit will maximize the detector acceptance while still not observing candidate events. The largest acceptance which was investigated in this analysis was estimated to be 0.068 m^2 sr, with a corresponding antiproton background of 0.57. The cuts applied are listed in Tab. 4.3. The Feldman-Cousins 95% C.L. signal is thus 2.59. The trigger efficiency is estimated to be 0.83 $\pm$ 0.01. The energy width and the measuring time are unchanged. The AMS-02 antideuteron exclusion limit at 95% C.L. is thus 1.23 $\times$ 10^{-5} [(GeV/n) m^2 sr s]$^{-1}$.

The best current antideuteron flux limit comes from the BESS collaboration [62]. Their analysis used the Feldman-Cousins 95% C.L. and did not consider backgrounds from simulation. With this methodology they obtained an upper limit of 1.9 $\times$ 10^{-4} [(GeV/n) m^2 sr s]$^{-1}$ for the kinetic energy range 0.17-1.15 GeV/n. Using the BESS-Polar2 data they further lowered this limit to 6.6 $\times$ 10^{-5} [(GeV/n) m^2 sr s]$^{-1}$ [63]. Fig. 4.35 compares the results.

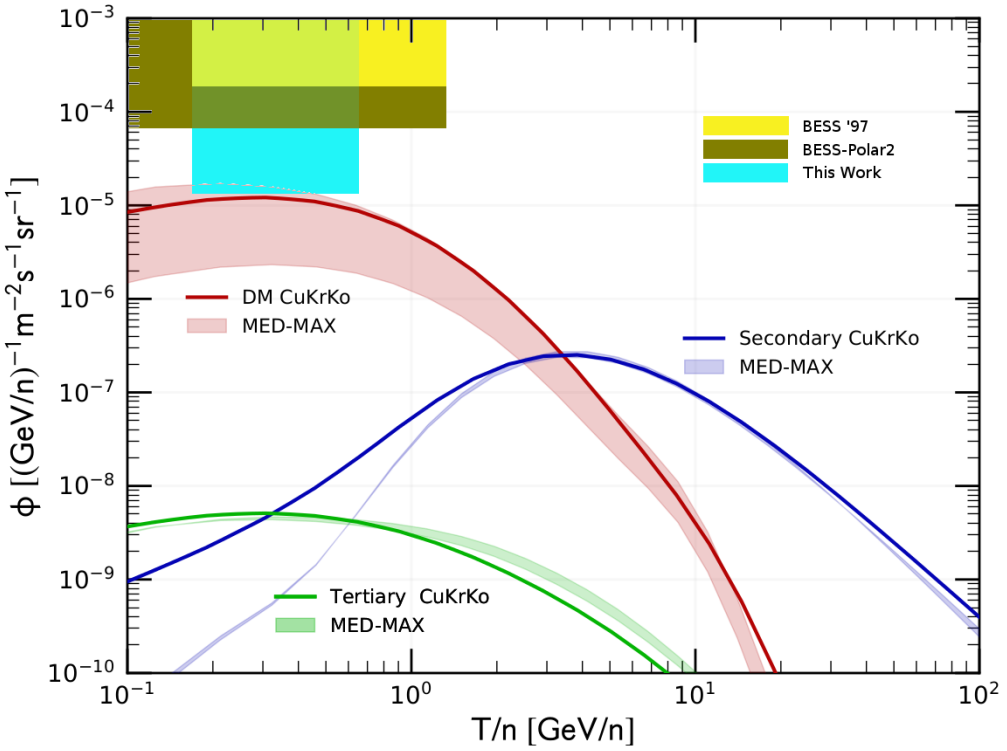

FIGURE 4.35: The antideuteron exclusion limit of this analysis has been calculated for a 95% confidence level using the Feldman-Cousins statistical approach. This result is compared to the current best antideuteron limit obtained by the BESS collaboration using the same approach.

4.2.8 Antideuteron Sensitivity Estimation through 2024 and Beyond

The ISS is slated to continue operation through at least 2024. It is therefore reasonable to make a prediction of the AMS-02 antideuteron sensitivity extrapolated to this time. An end date of January 1, 2025 is assumed for convenience. The analysis previously presented was for data obtained between May 20, 2011 until May 12, 2017. This amounted to a total flight time of 182476046 seconds. The total time between May 20, 2011 and January 1, 2025 is 428024897 seconds. The ratio between the two flight times is 2.35 and will be used as our time scaling factor. The preceding analysis had a total measuring time above geomagnetic cutoff of 7925455 seconds. The predicted measuring time through 2024 can be approximated by using the time scaling factor, and is thus 18589947 seconds.

The antiproton background will be directly proportional to the flight time. The presented analysis was shown to have 0.081 background antiprotons. The predicted background will then be the multiplication of the currently observed antiproton background with the time scaling

TABLE 4.3: Quality cuts for the antideuteron exclusion limit.

Cut					Cut Group
Tracker Track Zenith Angle at L2			$\leq$	45°	Fiducial Cuts
Tracker Track Zenith Angle at RICH Radiator			$\leq$	45°	Fiducial Cuts
Tracker Track Radius at Z = 0			$<$	47.0 cm	Fiducial Cuts
Extrapolated Tracker Track RICH crossing radius			$<$	80.0 cm	Fiducial Cuts
TOF Clusters Associated with AMSParticle	$=$	4			Hits Cuts
TOF Clusters NOT Associated with AMSParticle			$\leq$	1	Hits Cuts
ACC Hits			$\leq$	1	Hits Cuts
Inner Tracker XY Hits	$\geq$	5			Hits Cuts
RICH Hits	$\geq$	0	$\leq$	10	Hits Cuts
Tracker Track TOF Hit Matching					Track Matching Cuts
TRD Vtrack Tracker Track residual azimuth angle at UTOF			$<$	6.27°	Track Matching Cuts
TRD Vtrack Tracker Track residual zenith angle at UTOF			$<$	2.19°	Track Matching Cuts
Total UTOF Energy Deposition	$>$	3.0 MeV			Charge Cuts
Total LTOF Energy Deposition	$>$	3.0 MeV			Charge Cuts
Tracker Charge	$>$	0.700	$<$	1.300	Charge Cuts
Overall TOF Charge	$>$	0.700	$<$	1.300	Charge Cuts
UTOF Charge	$>$	0.700	$<$	1.300	Charge Cuts
LTOF Charge	$>$	0.600	$<$	1.300	Charge Cuts
Tracker Track Normalized χ^2 X			$<$	10	χ^2 Cuts
Tracker Track Normalized χ^2 Y (bending plane)			$<$	10	χ^2 Cuts
TOF BetaH Spatial Normalized χ^2			$<$	10	χ^2 Cuts
TOF BetaH Timing Normalized χ^2			$<$	10	χ^2 Cuts
Clean TRD Cut					TRD Likelihood Cuts
TRD Active Layers (Used in likelihood calculation)	$\geq$	10			TRD Likelihood Cuts
TRD Electron Proton Log Likelihood	$\geq$	0.3			TRD Likelihood Cuts
TOF Truncated Mean dE/dx Cut (remove pions and kaons)					dE/dx Cut
Antideuteron Edge dE/dx Cut					dE/dx Cut
No TRD Vertices					TRD Vertex Cut

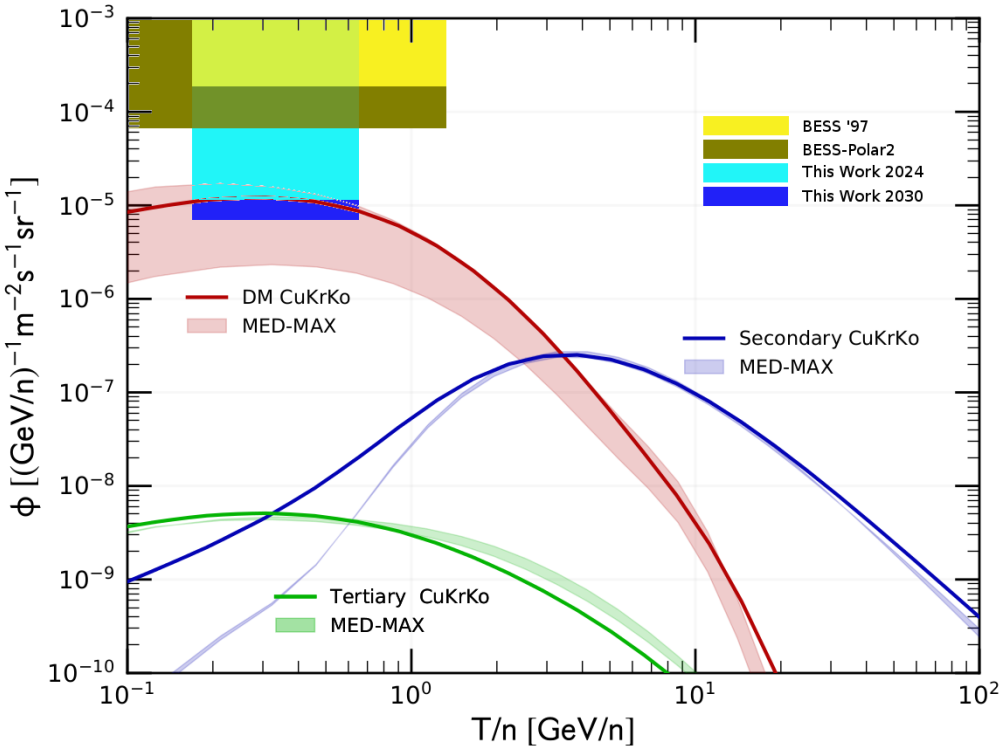

FIGURE 4.36: The predicted antideuteron sensitivity of this analysis through 2024 and 2030 has been calculated for a 3σ significance using integer signal counts. This result is compared to the current best antideuteron exclusion limits obtained by the BESS collaboration.

factor, yielded a predicted background of 0.19 antiprotons. Using this background, we may calculate the necessary signal of antideuterons to constitute a greater than 3σ significance using Eq. 4.3. It is found that in order to have a greater than 3σ signal 2.64 antideuterons should be observed. We should round up to 3 to have an integer antideuteron count. The trigger efficiency, the acceptance, and the energy width are unchanging with time.

Substituting these predicted values into Eq. 4.4 leads to a predicted discovery sensitivity of 1.01 $\times$ 10^{-5} [(GeV/n) m^2 sr s]$^{-1}$ for a significance of signal greater than 3.

An estimate through 2030 is also interesting if one considers a possible ISS lifetime extension. The total time from May 20, 2011 until January 1, 2031 is 617327297 seconds. The time ratio is thus 3.38. The antiproton background prediction is then 0.27. It is found that in order to have a greater than 3σ signal 3 antideuterons should be observed. Substituting these predicted values into Eq. 4.4 leads to a predicted discovery sensitivity of 7.00 $\times$ 10^{-6} [(GeV/n) m^2 sr s]$^{-1}$ for a significance of signal greater than 3.

Chapter 5

Conclusion

5.1 Galactic Antiproton Flux Result

One focus of this work was the precision measurement of the Galactic antiproton flux in Low Earth Orbit using the AMS-02 experiment. This was done as a precursor to the Galactic antideuteron search. AMS-02 previously published a Galactic antiproton flux [12] which covered the momentum range 1 GeV/c to 450 GeV/c using the silicon tracker for momentum reconstruction. This work sought to investigate the low momentum region in greater detail and to push to lower values. The Time of Flight system was used for the determination of particle velocity, and thus momentum, for this analysis. Many quality cuts were identified to suppress the pion and kaon background. An algorithm was developed to identify and exclude interaction vertices in the TRD which were identified as a background source of antiparticles. Secondaries produced outside of AMS-02 were suppressed by cutting on the energy deposition in the TOF. In this way the AMS-02 antiproton flux was extended down to 0.85 GeV/c.

The result is consistent with previous results from other experiments. The methods used were thus validated for the investigation of Galactic antideuterons.

5.2 AMS-02 Antideuteron Exclusion Limit

By measuring the Galactic antiproton flux, the antiproton background for antideuterons was investigated in great detail. A method was developed to distinguish between antiprotons and antideuterons using energy depositions in the TOF and silicon tracker. In addition to the separation power from $\mathrm{d}E/\mathrm{d}X$, the reconstructed mass of events was used as a final cut to distinguish between antiprotons and antideuterons. No Galactic antideuteron candidates were

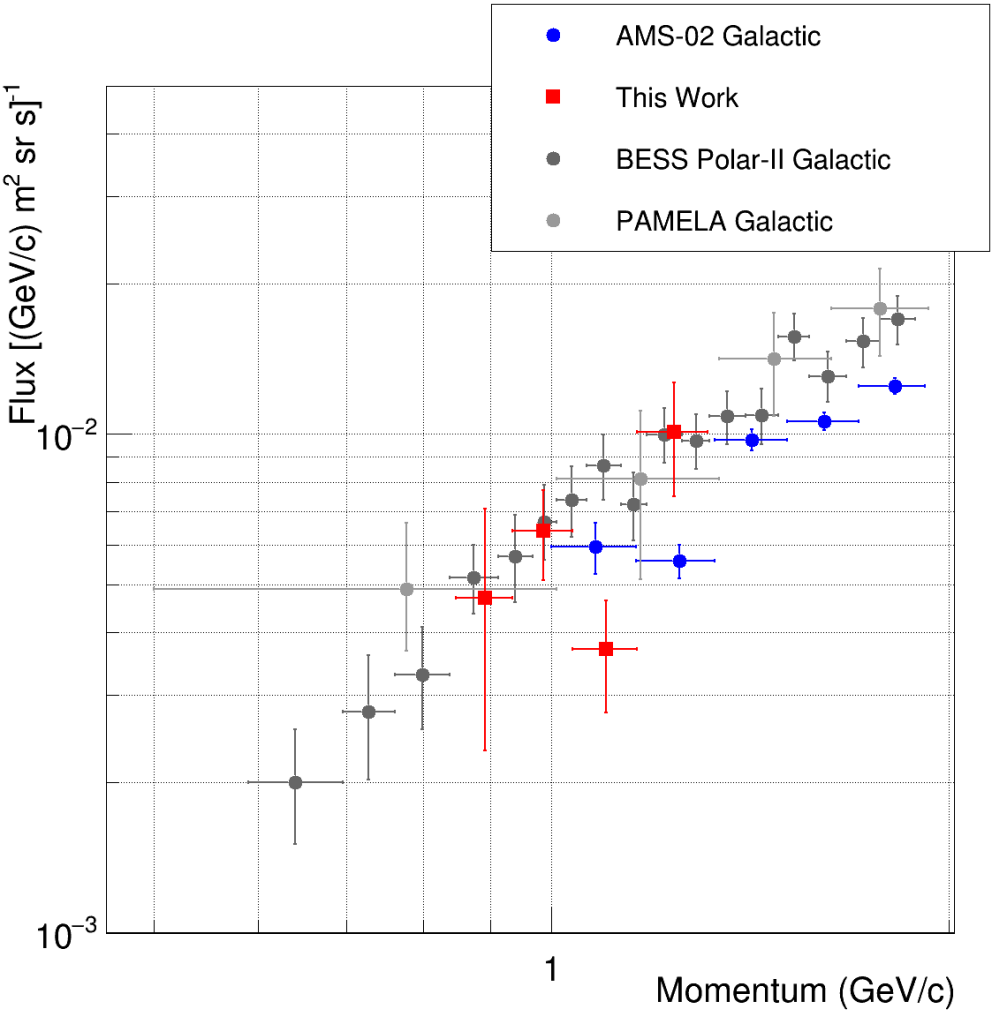

FIGURE 5.1: The Galactic antiproton flux measured as function of momentum. Also presented is the measured antiproton flux from the tracker based analysis as well as resulted from the BESS-Polar II balloon.

observed by AMS-02 between 2011 and 2017. By using extensive antideuteron simulation, the AMS-02 antideuteron exclusion limit has been calculated to be 1.23×10^{-5} $[(\mathrm{GeV}/n)\ \mathrm{m}^2\ \mathrm{sr\ s}]^{-1}$. It is currently the lowest antideuteron flux limit measured to date, for the first time probing the antideuteron discovery space.

The limit is such that the large coalescence momentum assumption in [17] has been ruled out for the specific choice of model. The typical coalescence momentum assumption cannot be ruled out by the current analysis.

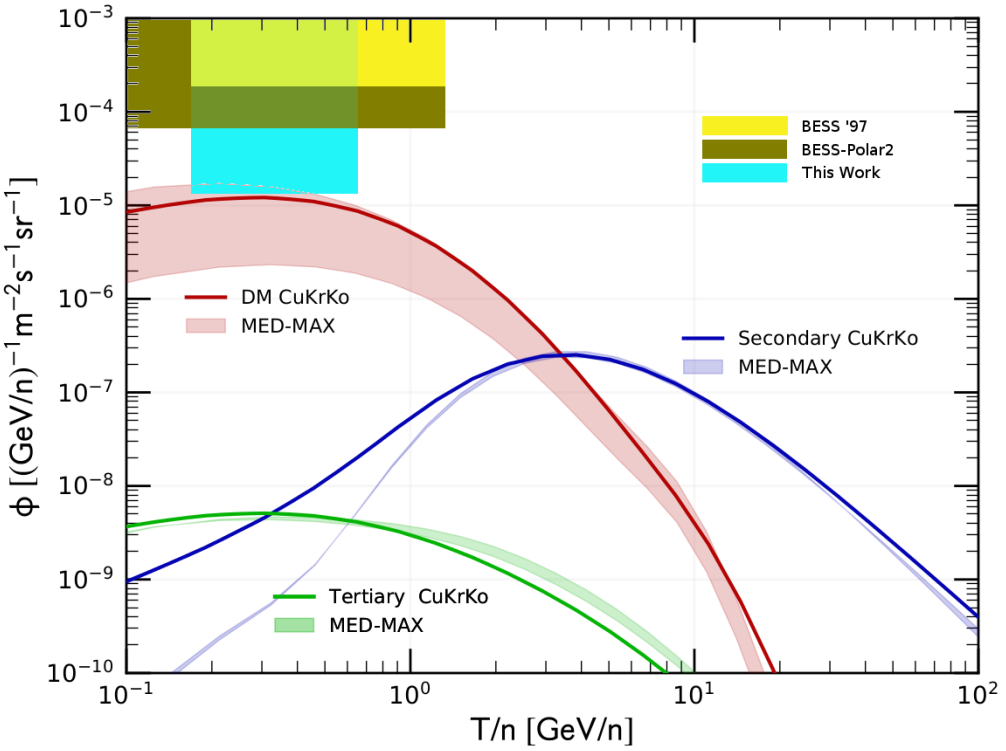

FIGURE 5.2: The antideuteron exclusion limit of this analysis has been calculated for a 95% confidence level using the Feldman-Cousins statistical approach. This result is compared to the current best antideuteron limit obtained by the BESS collaboration using the same approach.

5.3 AMS-02 Antideuteron Sensitivity Prediction Through 2024 and Beyond

Improvements were made to the quality cuts developed during the Galactic antiproton flux analysis. The cuts were optimized to maximize the AMS-02 antideuteron discovery sensitivity should the detector continue nominal operation. Considering that the AMS-02 detector will be operational through at least 2024 and perhaps through 2030 it is possible to estimate the sensitivity that is attainable with the increased run time. It has thus been estimated that AMS-02 can reach a discovery sensitivity of 1.01×10^{-5} $[(\mathrm{GeV}/n)\ \mathrm{m}^2\ \mathrm{sr}\ \mathrm{s}]^{-1}$ for a significance of signal greater than 3 if data taking continues through 2024 and 7.00×10^{-6} $[(\mathrm{GeV}/n)\ \mathrm{m}^2\ \mathrm{sr}\ \mathrm{s}]^{-1}$ if data taking continues through 2030. According to Fig. 5.3 it is worth while to continue operation of AMS-02 for as long as possible. The increased runtime will allow AMS-02 to probe deeper into the preferred parameter space of this particular Dark Matter model.

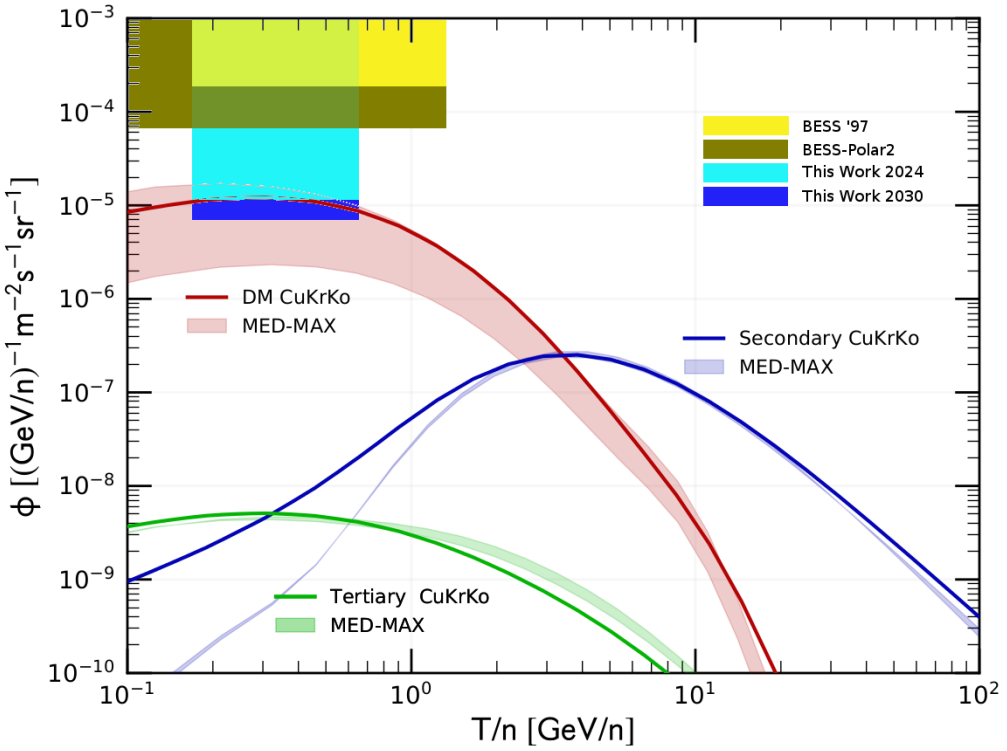

FIGURE 5.3: The predicted antideuteron sensitivity of this analysis through 2024 and 2030 has been calculated for a 3σ significance using integer signal counts. This result is compared to the current best antideuteron exclusion limit obtained by the BESS collaboration.

5.4 Final Remarks

No cosmic-ray antideuterons were observed by AMS-02 with this analysis. The antideuteron exclusion limit has been improved by an order of magnitude. Analysis of the AMS-02 data ongoing and further improvement of the antideuteron exclusion limit is possible.

This analysis focused on the low-energy antideuterons which would most likely originate from Dark Matter candidates. The AMS-02 detector can identify cosmic-rays to many orders of magnitude higher energy than this. Analyses focusing on higher energies by using the RICH are ongoing. These will probe the region where secondary antideuteron production peaks. AMS-02 still has great potential to make the first observation of antinuclei in cosmic rays.

What is Dark Matter? Humanity still does not know.

Appendix

Data Used

This analysis analyzed data taken on the International Space Station from May 20, 2011 until May 12, 2017. The version of data reconstruction (pass) is 6. The version of analysis is B950.

Simulation was used for much this analysis. Tab. 1 provides relavent information for the MCs used.

Table 1: Monte Carlo used and associated information.

Species	Version	Starting Rigidity (GV)	Ending Rigidity (GV)	Simulated Events	Generation Plane
Antiproton	B1068	0.25	2	5×10^9	Top Plane
Antiproton	B1128	0.20	1000	10^{10}	Top Plane
Antideuteron	B1128	0.20	1000	10^{10}	Top Plane
Proton	B1128	0.20	10	10^{10}	Full Cube
Proton	B1128	5	200	10^{10}	Full Cube
Proton	B1128	100	2000	10^{10}	Full Cube

Bibliography

[1] Hess, V. F. Über Beobachtungen der durchdringenden Strahlung bei sieben Freiballonfahrten. *Phys. Z.* **13**, 1084–1091 (1912).

[2] Margiotta, A. Status of the KM3NeT project. *Journal of Instrumentation* **9**, C04020 (2014).

[3] Aguilar, M. *et al.* Precision Measurement of the Proton Flux in Primary Cosmic Rays from Rigidity 1 GV to 1.8 TV with the Alpha Magnetic Spectrometer on the International Space Station. *Phys. Rev. Lett.* **114**, 171103 (2015). URL https://link.aps.org/doi/10.1103/PhysRevLett.114.171103.

[4] Aguilar, M. *et al.* Precision Measurement of the Helium Flux in Primary Cosmic Rays of Rigidities 1.9 GV to 3 TV with the Alpha Magnetic Spectrometer on the International Space Station. *Phys. Rev. Lett.* **115**, 211101 (2015). URL https://link.aps.org/doi/10.1103/PhysRevLett.115.211101.

[5] Adriani. PAMELA Measurements of Cosmic-Ray Proton and Helium Spectra. *Science* **332**, 69–72 (2011). URL http://science.sciencemag.org/content/332/6025/69.

[6] Yoon, Y. S. *et al.* Cosmic-ray Proton and Helium Spectra from the First CREAM Flight. *The Astrophysical Journal* **728**, 122 (2011). URL http://stacks.iop.org/0004-637X/728/i=2/a=122.

[7] Aartsen, M. G. *et al.* Multimessenger observations of a flaring blazar coincident with high-energy neutrino IceCube-170922A. *Science* **361**, eaat1378 (2018).

[8] Ackermann, M. *et al.* Detection of the Characteristic Pion-Decay Signature in Supernova Remnants. *Science* **339**, 807 (2013).

[9] Dirac, P. A. M. The quantum theory of the electron. I **117**, 610–624 (1928). URL http://www.jstor.org/stable/94981.

[10] Anderson, C. D. The Positive Electron. *Phys. Rev.* **43**, 491–494 (1933). URL https://link.aps.org/doi/10.1103/PhysRev.43.491.

[11] Dorfan, D. E., Eades, J., Lederman, L. M., Lee, W. & Ting, C. C. Observation of Antideuterons. *Phys. Rev. Lett.* **14**, 1003–1006 (1965). URL https://link.aps.org/doi/10.1103/PhysRevLett.14.1003.

[12] Aguilar, M. *et al.* Antiproton Flux, Antiproton-to-Proton Flux Ratio, and Properties of Elementary Particle Fluxes in Primary Cosmic Rays Measured with the Alpha Magnetic Spectrometer on the International Space Station. *Phys. Rev. Lett.* **117**, 091103 (2016). URL https://link.aps.org/doi/10.1103/PhysRevLett.117.091103.

[13] Butler, S. T. & Pearson, C. A. Deuterons from High-Energy Proton Bombardment of Matter. *Phys. Rev.* **129**, 836–842 (1963). URL https://link.aps.org/doi/10.1103/PhysRev.129.836.

[14] Csernai, L. & Kapusta, J. I. Entropy and cluster production in nuclear collisions. *Physics Reports* **131**, 223 – 318 (1986). URL http://www.sciencedirect.com/science/article/pii/0370157386900311.

[15] Baltz, A. *et al.* Strange cluster formation in relativistic heavy ion collisions. *Physics Letters B* **325**, 7 – 12 (1994). URL http://www.sciencedirect.com/science/article/pii/0370269394900639.

[16] Gomez-Coral, D.-M. *et al.* Deuteron and antideuteron production simulation in cosmic-ray interactions. *Phys. Rev. D* **98**, 023012 (2018). URL https://link.aps.org/doi/10.1103/PhysRevD.98.023012.

[17] Korsmeier, M., Donato, F. & Fornengo, N. Prospects to verify a possible dark matter hint in cosmic antiprotons with antideuterons and antihelium. *Phys. Rev. D* **97**, 103011 (2018). URL https://link.aps.org/doi/10.1103/PhysRevD.97.103011.

[18] et al, G. A. Observation of a new particle in the search for the Standard Model Higgs boson with the ATLAS detector at the LHC. *Physics Letters B* **716**, 1 – 29 (2012). URL http://www.sciencedirect.com/science/article/pii/S037026931200857X.

[19] et al, S. C. Observation of a new boson at a mass of 125 GeV with the CMS experiment at the LHC. *Physics Letters B* **716**, 30 – 61 (2012). URL http://www.sciencedirect.com/science/article/pii/S0370269312008581.

[20] Zwicky, F. Die Rotverschieb ung von extragalaktischen Nebeln. *Helv. Phys. Acta* **6**, 110–127 (1933).

[21] Babcock, H. *On The Rotation Curve of the Andromeda Nebula* (1938).

[22] Freeman, K. On the Disks of Spiral and S0 Galaxies. *Astrophys. J.* **160**, 811 (1970).

[23] Freese, K. Status of dark matter in the universe. *International Journal of Modern Physics D* **26**, 1730012 (2017). URL https://doi.org/10.1142/S0218271817300129.

[24] Raffelt, G. Dark Matter: Motivation, Candidates, and Searches. *ESHEP Proceedings 1997* (1997).

[25] White, J. N. C. F. S. The Structure of Cold Dark Matter Halos. *Astrophys. J.* **463**, 563 (1996).

[26] Turner, E. K. M. *The Early Universe* (Addison-Wesley, 1990).

[27] Tata, H. B. X. *Weak Scale Supersymmetry* (Cambridge, 2006).

[28] Giovacchini, F. *Cosmic Ray Anti-Deuteron Flux Sensitivity of the AMS-02 Detector* (2007).

[29] Aguilar. First Result from the Alpha Magnetic Spectrometer on the International Space Station: Precision Measurement of the Positron Fraction in Primary Cosmic Rays of 0.5˘350 GeV. *Phys. Rev. Lett.* **110**, 141102 (2013). URL https://link.aps.org/doi/10.1103/PhysRevLett.110.141102.

[30] Adriani, O. *et al.* PAMELA Results on the Cosmic-Ray Antiproton Flux from 60 MeV to 180 GeV in Kinetic Energy. *Phys. Rev. Lett.* **105**, 121101 (2010). URL https://link.aps.org/doi/10.1103/PhysRevLett.105.121101.

[31] Fornengo, N., Maccione, L. & Vittino, A. Dark matter searches with cosmic antideuterons: status and perspectives. **9**, 31 (2013).

[32] Cui, Y., Mason, J. D. & Randall, L. General analysis of antideuteron searches for dark matter. *Journal of High Energy Physics* **2010**, 17 (2010). URL https://doi.org/10.1007/JHEP11(2010)017.

[33] Buckley, J. *et al.* Cosmic Frontier Indirect Dark Matter Detection Working Group Summary. *ArXiv e-prints* (2013).

[34] Alcaraz, J. Protons in near earth orbit. *Phys. Lett. B* **461**, 387–396 (1999).

[35] Alcaraz, J. Search for Antihelium in Cosmic Rays. *Phys. Lett. B* **472**, 215–226 (2000).

[36] Alcaraz, J. Cosmic Protons. *Phys. Lett. B* **490**, 27–36 (2000).

[37] Kirn, T. The AMS-02 transition radiation detector. *Nucl. Inst. Meth. A* **581**, 156–159 (2007).

[38] Bindi, V. *et al.* The time of flight detector of the AMS-02 experiment on the international space station. *Nuclear Instruments and Methods in Physics Research Section A: Accelerators, Spectrometers, Detectors and Associated Equipment* **718**, 478 – 480 (2013).

URL http://www.sciencedirect.com/science/article/pii/S0168900212013988, proceedings of the 12th Pisa Meeting on Advanced Detectors La Biodola, Isola dElba, Italy, May 20 26, 2012.

[39] Lbelsmeyer, K. *et al.* Upgrade of the Alpha Magnetic Spectrometer (AMS-02) for long term operation on the International Space Station (ISS). *Nuclear Instruments and Methods in Physics Research Section A: Accelerators, Spectrometers, Detectors and Associated Equipment* **654**, 639 – 648 (2011). URL http://www.sciencedirect.com/science/article/pii/S0168900211011752.

[40] Haino, S. Performance of the AMS-02 silicon tracker in the {ISS} mission. *Nuclear Instruments and Methods in Physics Research Section A: Accelerators, Spectrometers, Detectors and Associated Equipment* **699**, 221 – 224 (2013). URL http://www.sciencedirect.com/science/article/pii/S0168900212005682, proceedings of the 8th International Hiroshima Symposium on the Development and Application of Semiconductor Tracking Detectors Academia Sinica, Taipei, Taiwan, December 5 8, 2011.

[41] von Doetinchem, P. *et al.* The AMS-02 Anticoincidence Counter. *Nuclear Physics B - Proceedings Supplements* **197**, 15 – 18 (2009). URL http://www.sciencedirect.com/science/article/pii/S0920563209007464, 11th Topical Seminar on Innovative Particle and Radiation Detectors (IPRD08).

[42] Pereira, R. The AMS-02 {RICH} detector: Performance during ground-based data taking at {CERN}. *Nuclear Instruments and Methods in Physics Research Section A: Accelerators, Spectrometers, Detectors and Associated Equipment* **639**, 37 – 41 (2011). URL http://www.sciencedirect.com/science/article/pii/S0168900210020292, proceedings of the Seventh International Workshop on Ring Imaging Cherenkov Detectors.

[43] Vecchi, M. *et al.* The electromagnetic calorimeter of the AMS-02 experiment. In *SF2A-2012: Proceedings of the Annual meeting of the French Society of Astronomy and Astrophysics* (eds. Boissier, S. *et al.*), 621–625 (2012).

[44] Agostinelli, S. *et al.* Geant4a simulation toolkit. *Nuclear Instruments and Methods in Physics Research Section A: Accelerators, Spectrometers, Detectors and Associated Equipment* **506**, 250 – 303 (2003). URL http://www.sciencedirect.com/science/article/pii/S0168900203013688.

[45] Allison, J. *et al.* Geant4 developments and applications. *IEEE Transactions on Nuclear Science* **53**, 270–278 (2006).

[46] Allison, J. *et al.* Recent developments in Geant4. *Nuclear Instruments and Methods in Physics Research Section A: Accelerators, Spectrometers, Detectors and Associated Equipment* **835**, 186 – 225 (2016). URL http://www.sciencedirect.com/science/article/pii/S0168900216306957.

[47] Pereira, R. *Private communication* (????).

[48] von Doetinchem, P. & Yamashiro, B. P o S (I C R C 2 0 1 7) 1 5 1 Geomagnetic Cutoff Calculations for the Interpretation of Low-rigidity Cosmic-ray Antiparticle Measurements (2017).

[49] Smart, D. & Shea, M. A review of geomagnetic cutoff rigidities for earth-orbiting spacecraft. *Advances In Space Research* (2004). URL http://engineering.dartmouth.edu/~d76205x/research/Shielding/docs/Smart_06.pdf.

[50] The polar aurora. By Carl Störmer. Oxford University Press, 1955. Pp. xvii, 403; 216 Figs., 27 Tables. 55s. *Quarterly Journal of the Royal Meteorological Society* **82**, 115–115 (1956). URL https://rmets.onlinelibrary.wiley.com/doi/abs/10.1002/qj.49708235123.

[51] Zuccon, P. *et al.* Atmospheric production of energetic protons, electrons and positrons observed in near Earth orbit. *Astroparticle Physics* **20**, 221 – 234 (2003). URL http://www.sciencedirect.com/science/article/pii/S0927650503001609.

[52] Derome, L. *et al.* Origin of the high energy proton component below the geomagnetic cutoff in near earth orbit. *Physics Letters B* **489**, 1 – 8 (2000). URL http://www.sciencedirect.com/science/article/pii/S037026930000914X.

[53] Alcaraz. Helium in near Earth orbit. *Physics Letters B* **494**, 193 – 202 (2000). URL http://www.sciencedirect.com/science/article/pii/S037026930001193X.

[54] Haino, S. *Private communication* (????).

[55] Sullivan, J. GEOMETRICAL FACTOR AND DIRECTIONAL RESPONSE OF SINGLE AND MULTI-ELEMENT PARTICLE TELESCOPES. *Nucl. Instrum. Methods 95: No. 1, 5-11(1971).* (????).

[56] D'Agostini, G. A multidimensional unfolding method based on Bayes' theorem. *Nuclear Instruments and Methods in Physics Research Section A: Accelerators, Spectrometers, Detectors and Associated Equipment* **362**, 487 – 498 (1995). URL http://www.sciencedirect.com/science/article/pii/016890029500274X.

[57] Abe, K. *et al.* Measurement of the Cosmic-Ray Antiproton Spectrum at Solar Minimum with a Long-Duration Balloon Flight over Antarctica. *Phys. Rev. Lett.* **108**, 051102 (2012). URL https://link.aps.org/doi/10.1103/PhysRevLett.108.051102.

[58] Adriani, O. *et al.* The Discovery of Geomagnetically Trapped Cosmic-ray Antiprotons. *The Astrophysical Journal Letters* **737**, L29 (2011). URL http://stacks.iop.org/2041-8205/737/i=2/a=L29.

[59] Abe, K. *et al.* Measurements of Cosmic-Ray Proton and Helium Spectra from the BESS-Polar Long-duration Balloon Flights over Antarctica. **822**, 65 (2016).

[60] Cowan, G. *Statistical Data Analysis* (Clarendon (Oxford), Oxford, 1998).

[61] Feldman, G. J. & Cousins, R. D. Unified approach to the classical statistical analysis of small signals. *Phys. Rev. D* **57**, 3873–3889 (1998). URL https://link.aps.org/doi/10.1103/PhysRevD.57.3873.

[62] Fuke, H. *et al.* Search for Cosmic-Ray Antideuterons. *Phys. Rev. Lett.* **95**, 081101 (2005). URL https://link.aps.org/doi/10.1103/PhysRevLett.95.081101.

[63] Sakai, K. COSPAR 2018 New results of very-low energy Antiproton spectrum and Antideuteron search in BESS-Polar II (2018).